学位論文

Study of Fe-rich chlorite and 7Å-14Å interstratified minerals using high-resolution electron microscopy

（高分解能電子顕微鏡法による鉄に富む緑泥石と7Å-14Å混合層鉱物の研究）

平成 27 年 12 月博士（理学）申請

東京大学大学院理学系研究科

地球惑星科学専攻

井上　紗綾子

Abstract

Chlorite is one of the most common phyllosilicates in sedimentary, low-to medium-grade metamorphic and hydrothermally altered rocks. Chlorite has a variety of polytypic structure and interstratified structure and a wide range of chemical compositions. They are believed to be functions of temperature and possibly many other intensive variables such as total pressure, partial pressures of oxygen and sulfur, and activities of metal cations in solution pertained to the formation. Elucidation of the relationships between the chlorite structure and their formation conditions leads to better understanding of geologic environments where chlorites occur. However, the correlations between the crystal structure of chlorite and its formation conditions have not been fully understood. In particular, the structure of Fe-rich chlorite remains ambiguous because of some difficulties for the structure analyses using X-ray diffraction (XRD).

The present study focused on firstly characterizing the structures of so-called Fe-rich chlorites of hydrothermal origin using high-resolution transmission electron microscopy (HRTEM) and high-angle annular dark field (HAADF) imaging in scanning transmission electron microscopy (STEM), along with XRD and chemical analysis. Secondly, for the sake of comparison, similar approaches were applied to pore-lining Fe-rich chlorites involving berthierines that occur in interstitial pores of sandstones.

Regarding Fe-rich chlorites of hydrothermal origin, the samples studied here had a wide range of Fe/(Fe+Mg) ratios of 0.38-0.98 and the tetrahedral Al substitutions for Si from 0.94 to 1.44 atoms per formula unit (apfu). The formation temperatures estimated by chlorite geothermometry ranged from 190 °C to 320 °C. Low magnification HRTEM images showed that most of the samples exhibited interstratified structures of 7Å, 14Å

and sporadically smectite layers. The proportion of 7Å layers increased progressively with Fe content and it reached >80% in Fe-rich samples with Fe/(Fe+Mg) > 0.9. Layer stacking structures in the high Fe-rich samples were so complex as to be associated with disorder of 7Å and 14Å layers, differences in the polarity of the tetrahedral sheets, variations of the slant of the octahedral sheets and positional disorder between octahedral and tetrahedral sheets involving the hydrogen bonding. From the chemical point of view, the 7Å layer approximated to Fe-rich berthierine. Berthierine usually occurs in sedimentary rocks and is believed to be a low temperature precursor of Fe-rich chlorite. However, the petrographic observations and the previous studies indicated that the present Fe-rich chlorite with 7Å component layer was directly precipitated from solution under relatively higher temperatures conditions.

To better understand the relationship between chemical composition and structural irregularity, the octahedral cation distributions in 7Å-14Å interstratified minerals with Fe/(Fe+Mg)>0.9 were further investigated in combination with HAADF-STEM observations and image simulations. HAADF-STEM observations along the X direction and the related directions suggested that octahedral Al concentrated in the M4 sites of the interlayer sheet in 14Å component layer. This is the first confirmation of X-ray hypothesis by STEM. Two types of 7Å layers with different octahedral cation distributions, named disordered- and ordered-types in this study respectively, were observed. The octahedral cations were randomly distributed in the disordered-type 7Å layer, while in the ordered-type 7Å layer octahedral Al preferentially concentrated in one of the octahedral sites. Vertical arrangements of 14Å layers and disordered- and ordered-type 7Å layers were random in the interstratified structure. The type of octahedral cation distribution varied laterally at the contact of opposite polar tetrahedral

sheets.

To clarify the differences between commonly observed sedimentary berthierine, 7Å-14Å interstratified mineral and chlorite, and hydrothermal samples, the structures of Fe-rich pore-lining chlorites in siliciclastic reservoir sandstones were investigated by HRTEM. The samples had Fe/(Fe+Mg) ratios of 0.75-0.80, and the formation temperatures ranged from 105 ºC to 220 ºC. Previous studies suggested that berthierine or odinite (7Å phase) was formed as a precursor at shallower depths, and subsequently transformed to chlorite through 7Å-14Å interstratified minerals with increasing burial depth. The interstratification of 7Å and 14Å layers was identified in the powder XRD patterns and the HRTEM images. The proportion of 7Å component layers in the interstratified mineral increased with decreasing temperature. The polytypic structure of the samples was, in general expressed as a mixture of I*b* and I*a* polytypic groups. The difference in the polarity of the tetrahedral sheets was very locally observed, whereas no lateral contact of opposite polar tetrahedral sheets was observed.

The structural characteristics of Fe-rich chlorite and their interstratified minerals observed in the present study provided a new formation mechanism based on the layer attachment growth model. For this growth model, three growth modules, named disordered-type, ordered-type and B-sheet, were assumed. Their existence was reasonably assumed from the present HRTEM and HAADF-STEM observations. The present Fe-rich chlorite and interstratified minerals were precipitated by the lateral and vertical accretion of the growth modules. The proposed model is still controversial but provides a clue to better understanding of the formation and transformation mechanism in nature.

CONTENTS

Chapter I GENERAL INTRODUCTION

Chlorite is one of the most common phyllosilicates in sedimentary, low-to-medium-grade metamorphic and hydrothermally altered rocks. The general chemical formula is expressed as $(R^{2+}_a R^{3+}_b \square_c)_6(Si_{4-x}R^{3+}_x)_4O_{10}(OH)_8$, where R^{2+} ions are the divalent cations of mainly Mg and Fe^{2+}, R^{3+} ions are the trivalent cations such as Al and Fe^{3+} and □ is the vacancy in octahedral sites, and the relationship of b - x = 2c exists (*e.g.* Brindley, 1982; Bailey, 1988a). Chlorite is known to have a variety of chemical compositions and polytypic structures. Variations in the chemical composition and structure are believed to be functions of temperature and possibly many other intensive variables such as total pressure, partial pressures of oxygen and sulfur and activities of metal cations in solution (*e.g.* Bailey, 1988a). When relating the variables to the formation conditions, it may be possible to reconstruct the paleo-environment under which chlorite was formed. Because chlorite occurs in various geologic environments, understanding the details of chlorite formation is important from the geological and mineralogical points of view, in addition to the viewpoint of natural resources such as oil and gas (*e.g.* Worden and Morad, 2003).

The relationship between chlorite composition and its formation temperature was studied closely and it is well known as “chlorite geothermometer” (*e.g.* Cathelineau and Nieva, 1985 ; Walshe, 1986; De Caritat *et al.*, 1993; Vidal *et al.*, 2001; Inoue *et al.*, 2009; Bourdelle *et al*., 2013; Lanari *et al*., 2014). On the other hand, the factors which control the structural variation of chlorite are not fully understood (*e.g.* Walker, 1993). One of the reasons is the paucity of crystallographic information of Fe-rich chlorite. It is mostly because the fine grain-size of Fe-chlorite makes the single crystal X-ray

diffraction (XRD) analysis difficult. In addition, Fe-rich chlorite often makes interstratified mineral with berthierine, Fe and Al-rich serpentine group mineral. The structural and chemical similarities between them often make it difficult to characterize 7Å-14Å interstratified mineral using conventional powder XRD or microprobe analysis. Thereby, the details of the transformation mechanism are not understood well.

High-resolution transmission electron microscopy (HRTEM) is a complementary tool to investigate the transformation mechanisms of fine-grained minerals at atomic scale. The HRTEM study of Fe-rich chlorite is beneficial to elucidate how the factors such as temperature and chemical composition affect the stacking structure of Fe-rich chlorite. However, many of previous HRTEM studies lacked such a viewpoint. More recently, high-angle annular dark field scanning transmission electron microscopy (HAADF-STEM) with finely focused electron probe has become of great interest in mineralogy. The contrast of HAADF-STEM image is roughly proportional to the square of atomic number (Z) (Pennycook and Jesson, 1992). This Z-contrast nature enables the identification of the octahedral cation distribution at atomic scale (Kogure and Drits, 2010; Kogure and Okunishi, 2010; Okumura *et al.*, 2014). It may be particularly useful to characterize the component layers in the interstratified minerals and to construct the transformation model.

The purpose of this study is to elucidate the factors controlling the structure of Fe-rich chlorite and as a result to understand the formation and transformation mechanisms. The minerals from different geologic environments, *i.e.*, hydrothermal and diagenetic origins, are characterized on the basis of HRTEM and STEM observations, together with powder XRD and chemical analysis. Special emphasis is paid to the characterization of 7Å-14Å interstratified structure which often appeared in Fe-rich

chlorite. In Chapter II, crystallochemical characteristics of chlorite which were revealed in the literatures are reviewed to distill the requirement of the high resolution TEM and STEM studies. From Chapters III to IV, the structures of Fe-rich chlorites from epithermal to xenothermal vein-type ore deposits are characterized by HRTEM and HAADF-STEM. The structural features are compared with those of more common intermediate Mg, Fe-chlorites from epithermal vein-type ore deposits. In Chapter V, pore-lining Fe-rich chlorites of diagenetic origins are characterized by HRTEM to compare their structural features with hydrothermal samples. In the end, the formation mechanism of 7Å-14Å interstratified minerals is discussed in Chapter VI.

Chapter II REVIEW OF CRYSTALLOCHEMICAL CHARACTERISTICS OF CHLORITE

II. 1. CHAPTER INTRODUCTION

Chlorite has been investigated by many previous studies. In general, the crystallochemical characteristics of chlorite are well described, but some of them still remain ambiguous. In particular, little is known about the structural features of Fe-rich chlorite. The simplest classification of chlorite is into Fe-rich types, known as chamosite, and Mg-rich types, known as clinochlore (Bayliss, 1975). The crystal structure of clinochlore has been investigated mainly using XRD analysis of single crystal (*e.g.* Pauling, 1930; McMurchy, 1934; Brindley and Ali, 1950; Steinfink, 1958a, b; Bailey and Brown, 1962). On the other hand, it is difficult to obtain single crystals of chamosite of sufficient size and quality to perform single crystal XRD analysis. Furthermore, there is little information available for the structure of Fe-rich chlorite from powder XRD pattern.

In the past few decades, the atomic scale analyses using HRTEM have become more and more common in the field of mineralogy. In chlorite minerals, HRTEM enables direct identification of stacking sequence and even polytypic structure if the structure is viewed along the proper directions (Kogure and Banfield, 1998). More recently, the high resolution imaging technique named HAADF-STEM is used to identify the octahedral cation distribution in phyllosilicate minerals (*e.g.* Kogure and Drits, 2010; Kogure and Okunishi, 2010). Therefore, HRTEM and STEM are expected to characterize the crystallochemical characteristics of Fe-rich chlorite which remain ambiguous in the previous studies.

In this chapter, first, the structural features of chlorite mainly obtained by XRD are summarized, following the excellent review of Bailey (1988a), to elucidate the unanswered questions with respect to the effects of formation conditions on the structure of chlorite. The second half of this chapter explores the previous TEM studies of chlorite and related minerals in order to show the requirement of the atomic scale investigation using high resolution TEM imaging techniques.

II. 2. CRYSTAL STRUCTURES OF PHYLLOSILICATES

Phyllosilicates ideally contain continuous two-dimensional tetrahedral sheets of composition T_2O_5, where T represents tetrahedral cations such as Si and Al. Each tetrahedron is linked with neighboring tetrahedron by sharing three corners (the basal oxygens) to form a hexagonal mesh pattern (Figure II-1a). Generally, all of the unshared corners (the apical oxygens) point to the same direction to form part of an adjacent octahedral sheet in which octahedra are linked laterally by sharing octahedral edges (Figure II-1b). The plane of junction between the tetrahedral and octahedral sheets consists of the apical oxygens and OH groups that lie at the center of each tetrahedral 6-fold ring at the same Z-level as the apical oxygens. Two types of layers, a ‘1:1 layer’ and a ‘2:1 layer’, exist depending on the ratio of components sheets (Figure II-2). The assemblage formed by linking one tetrahedral sheet with one octahedral sheet is called a 1:1 layer (TO) (Figure II-2a). The unshared anion plane of the octahedral sheet in the 1:1 layer consists of OH groups. On the other hand, the assemblage of two tetrahedral sheets and one octahedral sheet is called a 2:1 layer (TOT) which is formed by inverting a tetrahedral sheet so that its apical oxygens point down and are shared with the octahedral sheet below (Figure II-2b). Two anion planes of octahedral sheet in the 2:1

layer have the same O and OH composition. The 1:1 layer must be electrostatically neutral, whereas the 2:1 layer is not always electrostatically neutral. The excess layer charge is neutralized by interlayer materials including individual cations (mica), hydrated cations (smectite), and hydroxide octahedral sheet (chlorite) (Figure II-3). A unit structure is the total assembly and includes the layer and interlayer material. The terms "plane", "sheet" and "layer" cannot be used interchangeably and refer to the specific parts of the structure. The phyllosilicates are classified on the basis of layer type (1:1 and 2:1). Each phyllosilicate mineral group is characterized by the thickness of a unit structure, *i.e.* distance from one plane in the layer to that in the adjacent layer, which is called a basal spacing (Figure II-3).

Phyllosilicate minerals are further divided into two subgroups by the number of vacant sites in three octahedral sites of the smallest structural unit. If three octahedral sites are occupied, the sheet is considered as 'trioctahedral'. If only two octahedral are occupied and the third octahedral is vacant, the sheet is considered as 'dioctahedral'.

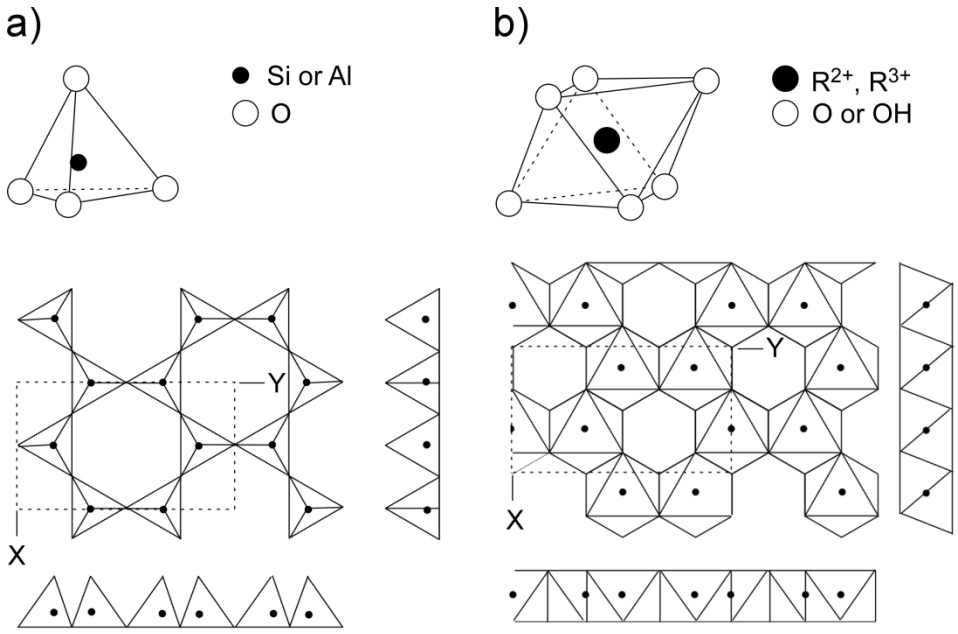

Figure II-1. Schematic diagrams of a) tetrahedral sheet and b) octahedral sheet.

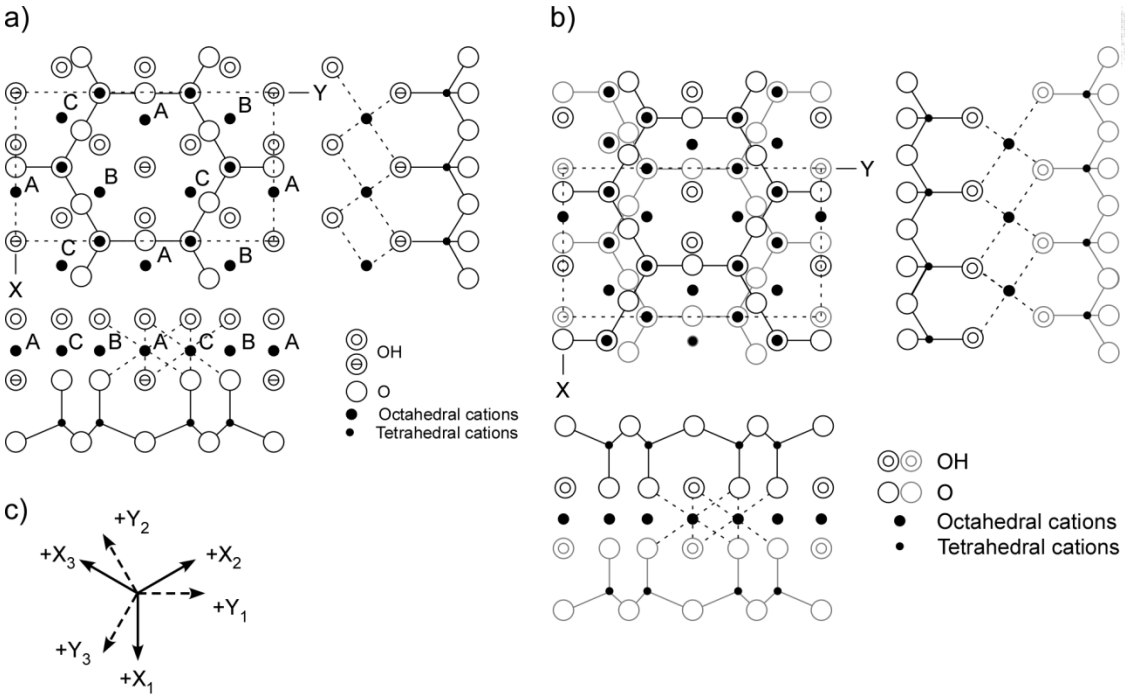

Figure II-2. Schematic diagrams of a) 1:1 layer and b) 2:1 layer and c) the definition of X*i* directions and Y*i* directions (*i* = 1-3) in the schematic diagrams. Three octahedral sites labeled A, B, C are defined in a).

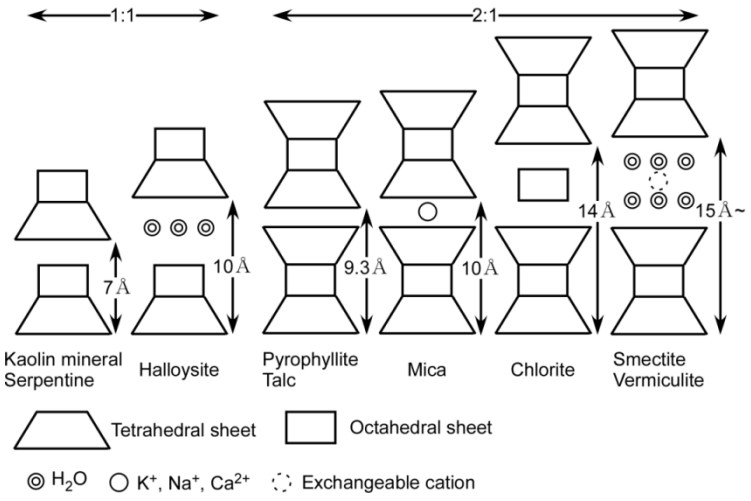

Figure II-3. Schematic diagrams showing the representative types of phyllosilicate minerals modified after Shirozu (1988).

As a consequence of different stacking arrangements of unit structures, phyllosilicates have a variety of stacking structures. Polytypism is defined by Bailey (1980) as "the existence of an element or compound in two or more layer-like crystal structures that differ in layer-stacking sequence. Polytypism differs from polymorphism in permitting small differences in chemical composition between structures, not to exceed 0.25 atoms per formula unit of any constituent element. Layer structures that differ from one another by more than this amount are to be called polytypoids rather than polytypes". Most of the phyllosilicates have polytypic forms. In general, "a set of related polytypes should be designated by a single name followed by a structural symbol suffix that defines the layer stacking differences" (Bailey, 1980).

Another distinct characteristic other than polytypism in the stacking structure of phyllosilicates is 'interstratified' or 'mixed-layer' structure, in which different types of layers are interstratified randomly or regularly. The terms 'interstratification', 'mixed-layering' and 'interlayering' are used interchangeably to describe the stacking of two or more assemblages of layers. They define how different types of layers form a stacking sequence. Component layers are stacked in random, partially regular or regular sequences. Randomly interstratified minerals are designated by the names of layer types. In the present study, following the rule of Reynolds (1992), the name of the component with the smallest value for d(001) after treatments places first. In cases where interstratified minerals contain expandable layer (*e.g.* smectite and vermiculite) as one of the component layers, the name of non-expandable layer (*e.g.* illite and chlorite) places first. A typical example is illite-smectite. Only regularly interstratified minerals that contain equal proportions of the two components can receive individual mineral names (Guggenheim *et al*., 2006).

The changes in polytypic structures and interstratification are believed to be functions of formation conditions such as temperature (*e.g.* Sudo, 1974; Shirozu, 1988 and references therein). For instance of muscovite, the transformation sequence of $1M_d \rightarrow 1M \rightarrow 2M_1$ is recognized with increasing temperature (Smith and Yoder, 1956; Velde, 1985).

II. 3. CHLORITE

II. 3. 1. Structure of chlorite

Chlorite has a 14Å unit structure consisting of alternation of the 2:1 layer of $\{M1(M2)_2(T)_4O_{10}(OH)_2\}$ and the interlayer sheet or the hydroxide sheet (B-sheet) of $\{(M3)_2M4(OH)_6\}$, where M1, M2, M3 and M4 are the octahedral sites occupied by cations such as Fe^{2+}, Mg, Al and Fe^{3+}, and T is the tetrahedral site occupied by Si and Al. The crystal structure of clinochlore is well described based on the results of XRD (*e.g.* Rule and Bailey, 1987; Bailey, 1988a; Zheng and Bailey, 1989), nuclear magnetic resonance (NMR: *e.g.* Welch *et al.*, 1995) and Mössbauer spectroscopy (MS: Smyth *et al.*, 1997). As a result, it is accepted that the octahedral trivalent Al and Fe^{3+} preferentially occupy M4 site in the B-sheet of clinochlore. The negative net charge of the 2:1 layer is compensated by the positive charge of the B-sheet. In addition to the electrostatic interaction, the hydroxyl surfaces of the interlayer sheet form long hydrogen bonding with the basal oxygen atoms of the 2:1 layers above and below the interlayer sheet (Figure II-4).

Bailey and Brown (1962) theoretically derived 12 polytypes of one-layer chlorite based on the variation in the orientation and position of the B-sheet relative to the adjacent 2:1 layers. The 12 polytypes were further divided into four structural types (I*a*,

I*b*, II*a*, II*b*). Each of the four structural types of chlorite can be involved in two different semi-random stacking sequences. Based on the equivalent relationships after 180º rotation about Y-axis, the eight resultant structures were reduced to six different structures. The stacking structure of semi-random stacking chlorite is described by six polytypic groups: I*aa*, I*ab*, I*bb*, II*aa*, II*ab* and II*bb* (Shirozu and Bailey, 1965). If the slant directions of the octahedral sheets in the 2:1 layer and the B-sheet are in the same direction, the structure is defined as type I, and if they are anti-parallel, then the structure is defined as type II (Figure II-5). Two types of mutual positions between the 2:1 layer and the B-sheet, *a* and *b*, are possible with the restriction to form the hydrogen bonding. In the *a* position, one of the three interlayer cations projects onto the center of hexagonal ring of the adjacent 2:1 layer and the other two cations project onto the tetrahedral cations. In the *b* position, the interlayer sheet is shifted by a/3 from the *a* position and no interlayer cations project onto the tetrahedral cations. Hence, it is suggested that the *b* position is energetically more favorable than *a* position (Bailey, 1988a).

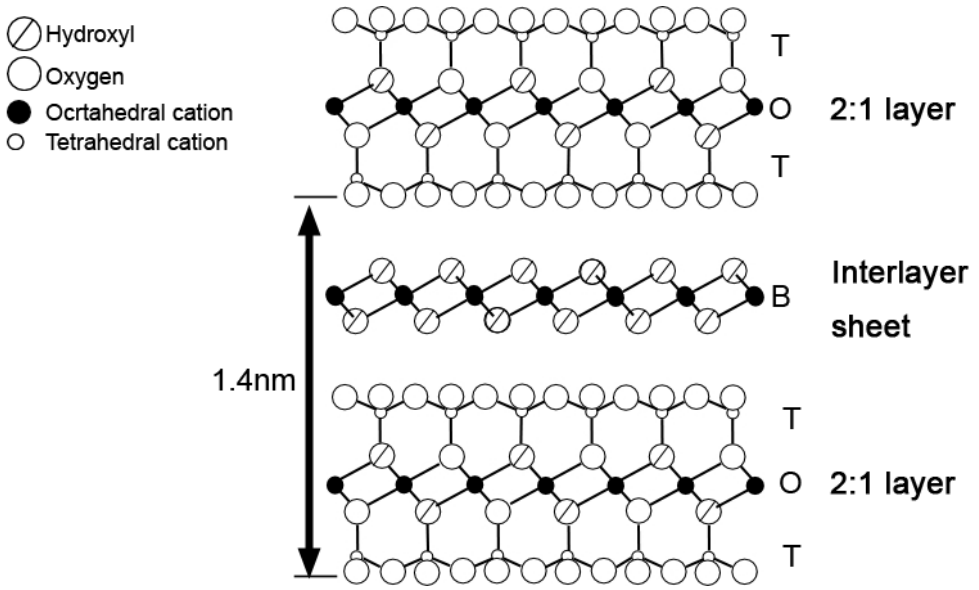

Figure II-4. [010] projection of structure of chlorite-I*bb*.

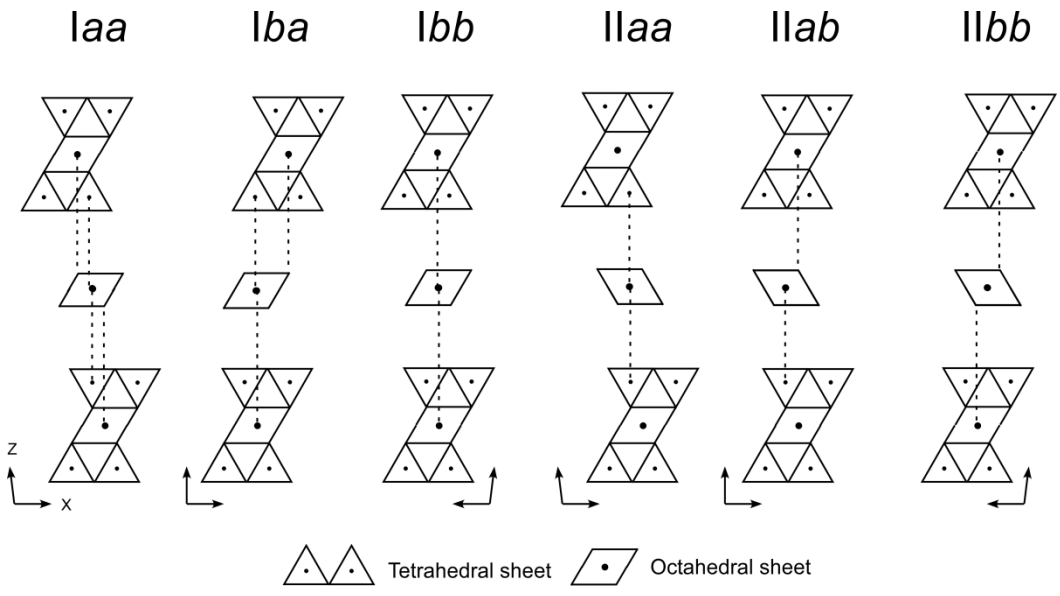

Figure II-5. Six polytypic groups of chlorite modified after Shirozu and Bailey (1965).

In nature, the occurrence of chlorite-II*bb* is most frequently reported, and the number of the occurrences of other polytypic groups decreases in the order of I*bb*, I*ba* and I*aa* (Bailey, 1988a). In addition, the stable chlorites in the chlorite zone of regional metamorphism and in medium-to- high temperature ore deposits are almost exclusively II*bb* (Bailey and Brown, 1962). Hence, it is widely accepted that II*bb* is the most stable structure of chlorite and the other polytypic groups have higher structural energy and form metastably (*e.g.* Bailey, 1988a and reference therein). Among six possible polytypic groups, neither II*aa* nor II*ab* is reported in nature. Hayes (1970) proposed that the polytype transformation sequence of $Ib_d \rightarrow Iba(\beta = 97^o) \rightarrow Ib\ (\beta = 90^o) \rightarrow IIb$ ($\beta = 97^o$) occurs in chlorites in sedimentary rocks that were exposed to progressively higher temperatures. This idea became a framework of the "chlorite polytype geothermometer". Later, Walker (1993) reviewed the reported occurrences of type I chlorite and pointed out that the transformation did not always occur at 200 ºC. For instance, type I chlorite may be stable at temperature as high as 300 ºC (Weaver *et al.*, 1984), whereas type II chlorite may form at temperature as low as 135 ºC (Walker and Thompson, 1990). Mg-rich chlorite is almost exclusively II*bb* which is the most stable polytype (Bailey and Brown, 1962; Curtis *et al.*, 1985). As mentioned above, because of its fine grain-size which makes the single crystal XRD analysis difficult, the crystal structure of Fe-rich chlorite is not sufficiently investigated (Bailey, 1988a). It is known, however, that Fe-rich chlorite tends to have I*bb* type structure (Bailey and Brown, 1962; Curtis, et al., 1985; Bailey, 1988a).

Chlorite layers can form randomly and regularly interstratified minerals with different phyllosilicate layers (Reynolds, 1988). The occurrences of interstratified chlorite minerals are often important to understand the genesis of chlorite such as the

mechanisms of chloritization process (*e.g.* Beaufort *et al.*, in press). Note that if chlorite is being considered as a component layer, the assemblage of the 2:1 layer and the interlayer sheet are considered as a single unit.

Mg-rich chlorite often makes interstratification with saponite, trioctahedral Mg-rich smectite (Reynolds, 1988). The transformation sequence of saponite-to-chlorite is related to the chloritization process found in a wide variety of geological environments such as hydrothermal alterations in continental and marine environments (*e.g.* Inoue *et al.*, 1984; Inoue and Utada, 1991; Beaufort and Meunier, 1994; Buatier *et al.*, 1995; Murakami *et al.*, 1999), diagenesis and very low grade metamorphism (*e.g.* Hillier, 1993; Jiang and Peacor, 1994; Dalla Torre *et al.*, 1996; Schmidt and Livi, 1999). As the temperature increases, saponite converts to chlorite by way of corrensite, a 1:1 regular interstratification of saponite-chlorite (Beaufort *et al.*, 1997; Drits *et al.*, 2011; Kogure *et al.*, 2013). The conversion progresses stepwise from saponite to corrensite and from corrensite to chlorite (Inoue, *et al.*, 1984; Inoue and Utada, 1991; Shau and Peacor, 1992; Beaufort, *et al.*, 1997; Murakami, *et al.*, 1999).

In contrast, Fe-rich chlorite is often intercalated by 7Å layer which is regarded as berthierine layer. The occurrences of berthierine-Fe-rich chlorite interstratified minerals have been reported from oolitic iron stones, iron formations and volcanogenic massive sulfide deposits (*e.g.* Velde, 1985; Meunier, 2005). The occurrences of Mg-rich 7Å-14Å interstratified mineral, probably lizardite-clinochlore, are reported in high temperature systems including metamorphic or hydrothermal systems (Banfield *et al.*, 1994; Banfield and Bailey, 1996). Furthermore, a 1:1 regular interstratified mineral of 7Å-14Å, named dozyite, was exclusively Mg-rich (Bailey *et al.*, 1995). However, the occurrence of Mg-rich type is limited and, in general, 7Å-14Å interstratified mineral is Fe-rich.

Berthierine is a Fe and Al-rich serpentine group mineral with chemical composition ideally of $(R^{2+}_a R^{3+}_b \square_c)_3(Si_{4-x}R^{3+}_x)_2O_5(OH)_4$ which is a half of that of chlorite. It occurs in sedimentary rocks (*e.g.* Bhattacharyya, 1983; Taylor, 1990 Hornibrook and Longstaffe, 1996), volcanogenic massive sulfide deposit (Jiang *et al.*, 1992; Slack *et al.*, 1992) and coal measure of Japan (Iijima and Matsumoto, 1982). Polytypes of serpentine group mineral are divided into four polytypic groups, group A, B, C and D (Bailey, 1988b Bailey, 1969). Most berthierine shows a mixture of group A (1*M*) and group C (1*T*) in the powder XRD pattern (Bailey, 1988c). As in the case of Fe-rich chlorite the details of crystal structure are not fully understand. Berthierine is generally regarded as a low temperature polymorph of Fe-rich chlorite (*e.g.* Velde, 1985; Meunier, 2005 and references therein). The transformation occurs at 70-200 °C by first interlayering of the two minerals (*e.g.* Velde, 1985; Hillier, 1994; Hornibrook and Longstaffe, 1996; Billault *et al.*, 2003; Meunier, 2005).

Most synthetic experiments of chlorite also indicated that chlorite was formed by way of 7Å phase regardless of Fe content of starting material (*e.g.* Nelson and Roy, 1958; Turnock, 1960; James *et al.*, 1976; Cho and Fawcett, 1986). The 7Å phase persisted for a long time (*e.g.* over 72 days at 600ºC in Cho and Fawcett (1986)) and finally converted to chlorite. More recently, hydrothermal experiments at relatively low temperature conditions demonstrated that berthierine was stable at low temperatures and Fe-rich chlorite was stable at higher temperatures at > 200 °C (*e.g.* Aagaard *et al.*, 2000; Mosser-Ruck *et al.*, 2010). The calorimetric measurements of Fe-rich chlorite and berthierine indicated that berthierine might transform into chlorite at higher temperatures, but the transformation temperature was dependent on the chemical composition of the two minerals (Blanc *et al.*, 2014).

The similarity in crystal structure and chemical composition between berthierine and Fe-rich chlorite often makes it difficult to characterize this type of interstratified mineral using conventional powder XRD or microprobe analysis. The interstratification of serpentine group mineral (7Å) and chlorite (14Å) results in weakening and broadening of odd-order 00*l* reflections relative to even-order ones (Reynolds, 1988; Reynolds *et al.*, 1992) (Figure II-6). If the amounts of 7Å layer are >20 % in the interstratified mineral, it is impossible to be detected by XRD (Reynolds *et al.*, 1992). Moreover, the weakening of odd order 00*l* reflections becomes conspicuous when the sample is Fe-rich (Figure II-7). As a result, the possibility of overlooking a small amount of intercalated 7Å layer in chlorite or intercalated 14Å layer in berthierine is a major problem to comprehend the relationships among berthierine, Fe-rich chlorite and berthierine-chlorite interstratified mineral more clearly.

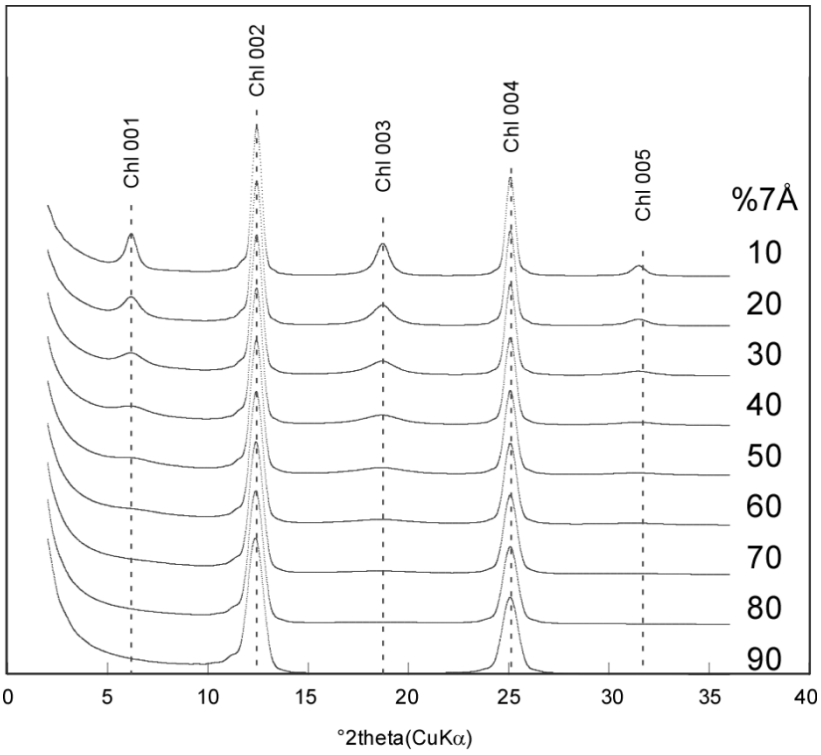

Figure II-6. XRD patterns of berthierine-chamosite interstratified minerals with different proportions of 7Å layers (%7Å) calculated using NEWMOD (Reynolds, 1985).

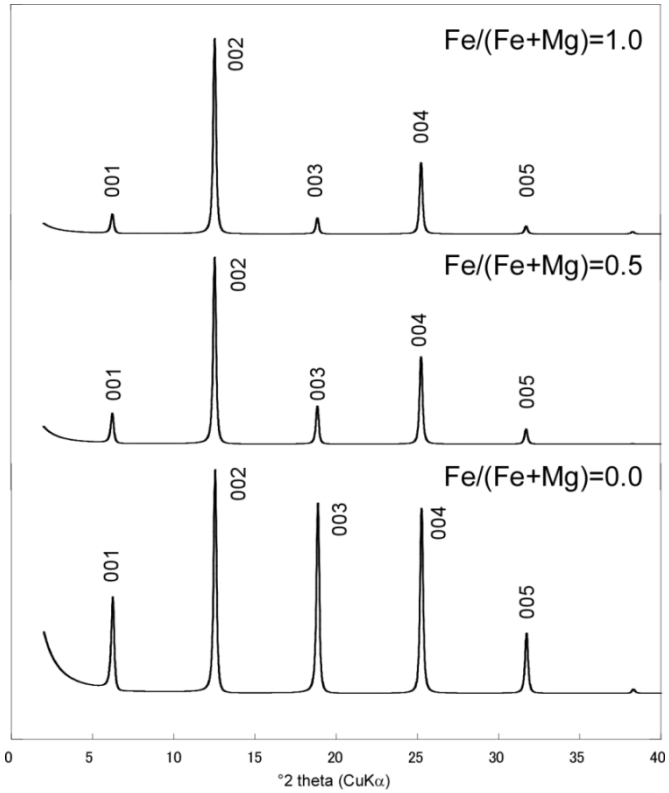

Figure II-7. XRD patterns of chlorite with different Fe/(Fe+Mg) ratio calculated using Sybilla © (Chevron™, Aplin *et al.*, 2006).

II. 3. 2. Nanoscopic approaches for the characterization of chlorite structure

As stated above, the structure of Fe-rich chlorite remains ambiguous. The structure of Fe-rich chlorite may be more complex than that of Mg-rich chlorite (Curtis, *et al.*, 1985). To overcome the difficulties in XRD examinations and to obtain crystallographic information from Fe-rich chlorite, HRTEM seems to be beneficial.

In the previous studies, HRTEM was mostly used to identify the basal spacings of each component layers in phyllosilicate minerals. For instance, it was used to identify the product phases of synthetic experiments (*e.g.* Rivard *et al.*, 2012) and the stacking sequence of the interstratification (*e.g.* Ahn and Peacor, 1985; Jiang, *et al.*, 1992; Slack, *et al.*, 1992; Banfield, *et al.*, 1994; Bailey, *et al.*, 1995; Banfield and Bailey, 1996; Xu and Veblen, 1996). The basal spacings are able to be measured in HRTEM images recorded. For Fe-rich 7Å-14Å interstratified minerals, HRTEM has been considered to be a most powerful and reliable technique to detect the interstratification. In addition to the vertical arrangement of 7Å and 14Å component layers, the lateral contact of opposite polar tetrahedral sheet was often observed in the HRTEM images (Jiang, *et al.*, 1992; Banfield, *et al.*, 1994; Banfield and Bailey, 1996; Xu and Veblen, 1996). Geometrically, two serpentine layers converted to one chlorite layer by the reversal of tetrahedral sheet. Hence, the lateral arrangement of the component layers was often interpreted as an evidence of the transformation from 7Å mineral to 14Å mineral (Xu and Veblen, 1996; Banfield and Bailey, 1996) and vice versa (Jiang *et al*., 1992). Based on the selected area electron diffraction (SAED) patterns obtained from the interstratified mineral, two types of conversion mechanisms were proposed. Xu and Veblen (1996) indicated that berthierine transformed to chlorite by inheriting the basic

polytypic structure of the reactant phase into the product phase by the relationship of antiphase boundary between the two layers. Banfield and Bailey (1996) showed a similar transformation between serpentine and clinochlore in metamorphosed serpentine. They proposed a different mechanism by taking into considerations the stability of the polytypic structure of product chlorite. A major criticism for the proposed models of transformation is that they did not consider the electrostatic difference which arises from the differences in two types of the octahedral sheets in chlorite.

The polytypic group of each layer in chlorite can be identified by HRTEM if the samples are viewed along one of the Y*i* directions defined by Bailey (1969) (see Figure II-2) (Kogure and Banfield, 1998, Figure II-8). This has made it possible to detect a mixture of different polytypic groups in chlorite (Kogure and Banfield, 1998; Kogure and Banfield, 2000) and to characterize the component layers in the interstratified chlorite minerals (Kogure, *et al.*, 2013) which are often unclear in XRD patterns. Accordingly, HRTEM observations from one of the Y*i* directions were expected to improve the transformation models from 7Å mineral to 14Å mineral. Most of the previous studies aforementioned, however, used the HRTEM images recorded along one of the X*i* directions. It may be partly because that the HRTEM observations along one of the X*i* directions are, in general, easier than those along one of the Y*i* directions.

Differences in chemical compositions of two component layers of 7Å-14Å interstratified mineral are difficult to investigate using electron microprobe analyzer (EPMA) and energy dispersive X-ray spectroscopy (EDX) equipped to SEM. Jiang *et al*. (1992) discussed whether the polymorphic relationship between berthierine and chlorite exists or not, based on the analytical TEM. Their berthierine was fortunately very coarse-grained relative to other occurrences, and hence it was possible to compare the

chemical compositions of berthierine, berthierine-chlorite and Fe-rich chlorite. In finely interstratified 7Å-14Å minerals, the chemical compositions of the two component layers were difficult to discriminate even using analytical TEM. Accordingly, the chemical compositions of 7Å and 14Å layers were assumed to be the same in the previous studies.

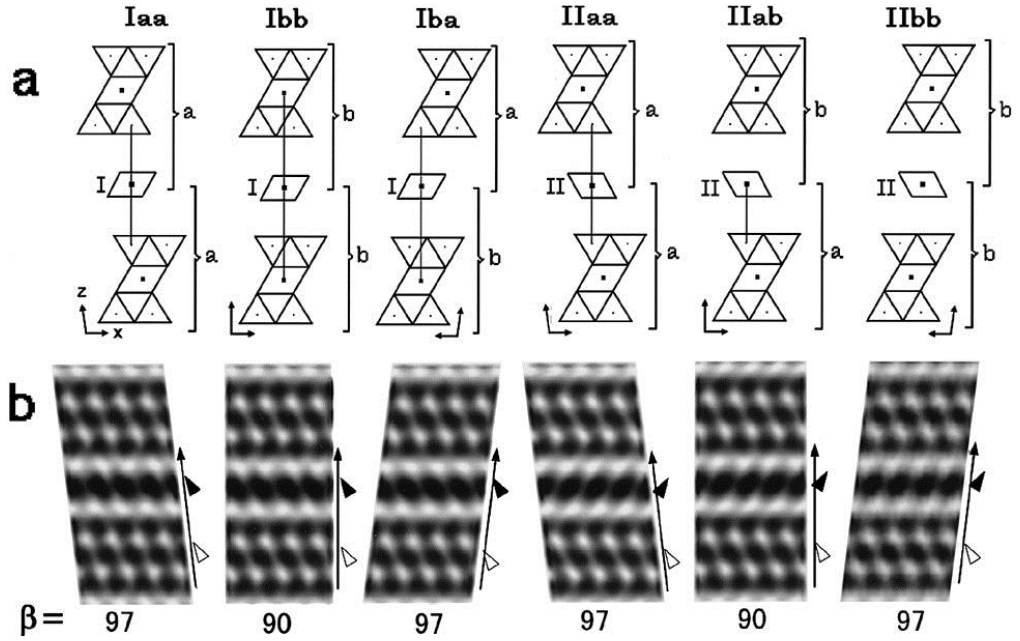

Figure II-8. (a) Schematic diagrams of each polytypic groups from [010] and (b) corresponding simulated HRTEM images. Reprinted from Kogure and Banfield (1998) with the permission from the Mineralogical Society of America.

II. 4. SUMMARY

General structure of chlorite was investigated by many researchers using XRD as reviewed in the section II.3.1. However, little is known about the stability of different chlorite structures and what controls the structure. It is especially because Fe-rich chlorite structure is not well characterized. HRTEM techniques are expected to progress the understandings of the stability of the chlorite structure. In particular, HRTEM is

considered as the most powerful technique to characterize the 7Å-14Å interstratified minerals which commonly occur in sedimentary Fe-rich chlorite. In most of the previous studies, HRTEM has been used to identify the stacking sequence of the interstratified minerals. A recent development of high resolution TEM and STEM techniques enables us to obtain much more crystallographic information that could not be obtained by conventional powder XRD. The application of such high resolution electron microscopic techniques is beneficial to elucidate the structural features of Fe-rich chlorite which remain ambiguous in XRD study.

From the next chapter, the crystallochemical characteristics of so-called Fe-rich chlorites from selected geologic environments are characterized using HRTEM and HAADF-STEM. In this study, the term chlorite signifies trioctahedral chlorite unless it is specifically mentioned otherwise.

Chapter III HIGH-RESOLUTION TRANSMISSION ELECTRON MICROSCOPY (HRTEM) STUDY OF STACKING IRREGULARITY IN FE-RICH CHLORITES FROM SELECTED HYDROTHERMAL ORE DEPOSITS

III. 1. INTRODUCTION

Chlorite and berthierine are structurally and chemically interrelated to each other. Interstratification of the two types of minerals commonly occurs in natural samples. As summarized in the previous chapter, berthierine is reported mainly from sedimentary rocks that have undergone early diagenesis (*e.g.* Velde, 1985; Meunier, 2005). In addition, the occurrences of Fe-rich chlorite and berthierine have been reported from oolitic iron stones, iron formations, and volcanogenic massive sulfide deposits (*e.g.* Velde, 1985; Slack and Coad, 1989). According to the field and laboratory studies (see reviews by Velde, 1985; Bailey, 1988a and references therein), berthierine may be a metastable phase at relatively high temperatures and probably transforms to chlorite with increasing temperature. The transformation occurs at 70-200 °C by way of interlayering of the two minerals (*e.g.* Velde, 1985; Hillier, 1994; Hornibrook and Longstaffe, 1996; Billault, *et al.*, 2003; Meunier, 2005). Otherwise, Slack, *et al.* (1992) and Jiang, *et al.* (1992) examined the structural relationship between berthierine and chlorite in a volcanogenic massive sulfide ore deposit of Archean age that have undergone metamorphism at 300-400 °C. They described that chlorite was replaced by berthierine through the topotactic transformation from chlorite to berthierine based on the lattice fringe images.

In addition to the transformation studies between berthierine and Fe-rich chlorite as

described in the previous chapter, the precipitation of extremely Fe-rich chlorite in association with quartz and sulfide deposition was studied in specific epithermal to xenothermal (in the sense of Buddington, 1935) vein-type ore deposits (*e.g.*, Nakamura, 1970; Shirozu, 1978; Inoue *et al.*, 2010). The Fe-rich chlorites are not transformation products of berthierine but appear to be direct precipitates from solution. Details of chemical and structural properties of these chlorites are, however, not well understood.

In this chapter, so-called Fe-rich chlorites from several hydrothermal ore deposits in Japan are characterized by HRTEM examination, together with powder XRD and chemical analyses. The structural characteristics of chlorites with high Fe/(Fe+Mg) ratio are compared to those of more common intermediate Mg, Fe-chlorites from epithermal vein-type ore deposits.

III. 2. SAMPLES

Seven chlorite samples were studied from epithermal to xenothermal vein-type ore deposits in Japan: each one from Toyoha, Arakawa and Ashio, two from Osarizawa, and two from drill cores in the geothermal field adjacent to the Toyoha deposit. All deposits formed in the Miocene to Pliocene (Shikazono, 2003). Chlorites studied here showed several modes of occurrences under optical microscope such as vein and pore fillings and replacements of the mafic minerals, plagioclase and matrix in rocks. Among these, chlorites showing the modes of occurrences which are characteristics of precipitates under optical and scanning electron microscopes were investigated in this study (*e.g.* Inoue *et al*., 2012) (Figures III-1 and 2).

The Toyoha deposit, Hokkaido Prefecture, consists of a network of veins with polymetallic mineralization of Pb, Zn, Ag, Mn, In, Cu, Bi, Sn etc. Hydrothermal activity

with mineralization started at ~3 Ma and they remain active. Chlorites from the mineralized vein in Toyoha deposit, Soya vein and drill cores (called TH-2 described in Inoue, *et al.*, 2010; Inoue *et al.*, 2012) from the adjacent geothermal field were investigated here. Soya chlorite is a gangue mineral from a quartz vein associated with sphalerite and pyrite (Figure III-2e). Homogenization temperatures of fluid inclusions in quartz ranged from 210 to 261 °C, on average 233 °C (A. Inoue, written communication), as given in Table III-1. Chlorites from drill core TH-2, which were collected at different depths of 680 m and 894 m of the core, fill veinlets in propylite, hydrothermally altered andesite, associated with quartz and pyrite (Figures III-2a-d). The hydrothermal alteration and homogenization temperatures of fluid inclusions in core TH-2 were described by Inoue *et al.* (2010, 2012).

Osarizawa and Arakawa, Akita Prefecture, are typical Cu-Pb-Zn epithermal vein-type ore deposits. Chlorite was collected from two mineralized quartz veins, the Ishikirizawa and Unotori veins in the Osarizawa deposit (Figures III-1a-d), and from the contact between a barren quartz vein and shale country rock in Arakawa (Figures III-1e and f). Chlorites from Osarizawa are associated with chalcopyrite, sphalerite, galena, and pyrite; those from Arakawa with pyrite and hematite. Homogenization temperatures of fluid inclusions in quartz ranged from 248 to 356 °C, on average 279 °C, for the Ishikirizawa; from 225 to 320 °C, on average 269 °C, for the Unotori; from 188 to 87 °C, on average 247 °C, for the Arakawa (Table III-1).

Ashio deposit, Tochigi Prefecture, is classified as a xenothermal polymetallic vein-type ore deposit (Imai *et al.*, 1975). Although the limited number of microthermometric studies in Ashio, it is believed that the ore formation occurred at temperatures of > 300 °C (Shikazono, 2003).

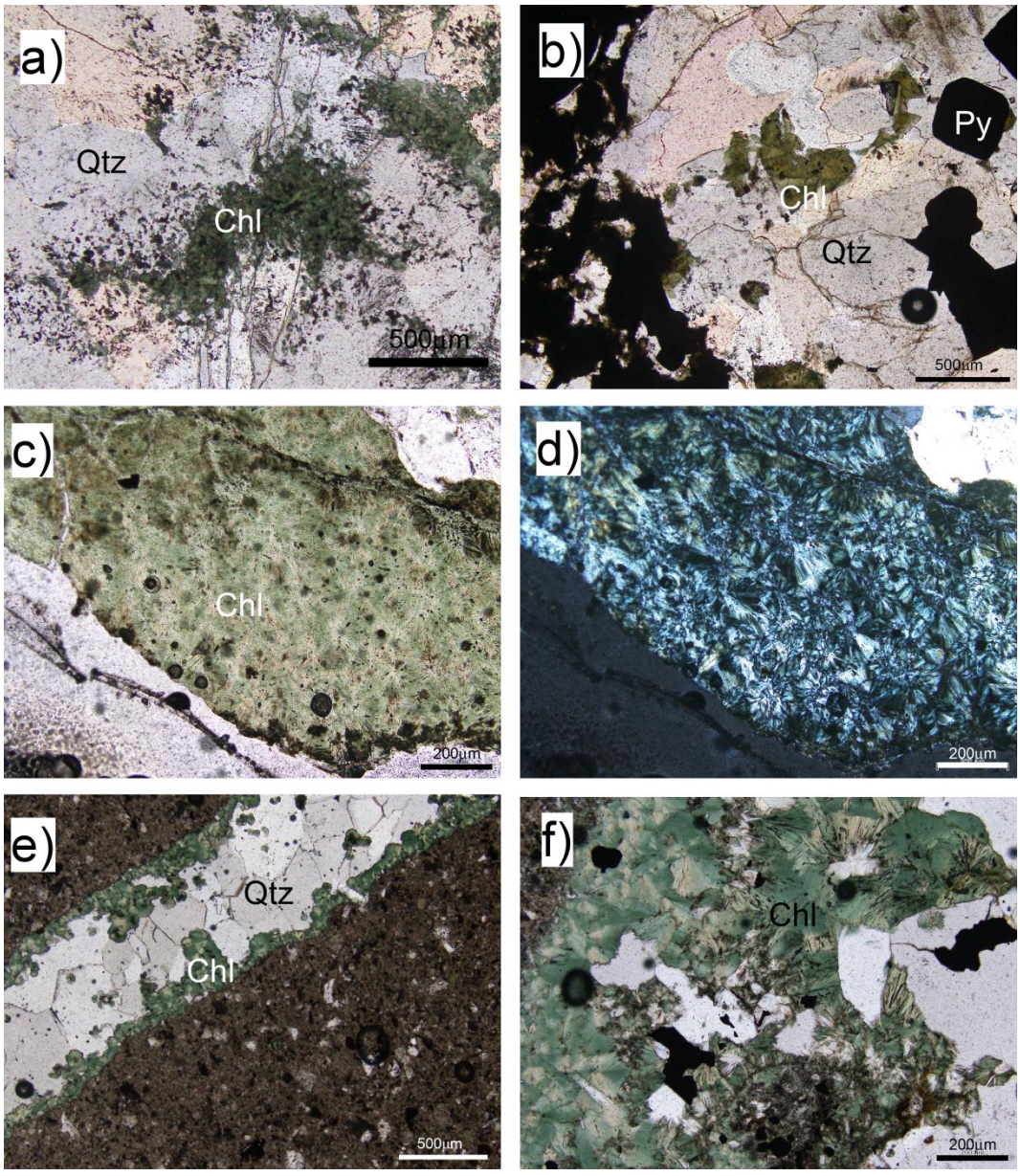

Figure III-1. Optical micrographs of chlorites. a) chlorites in quartz vein in the Ishikirizawa sample, b) chlorites in quartz vein in the Unotori sample, c) chlorites in quartz vein in the Unotori sample d) photo of b) under cross-polarized light, e) chlorites at the contact between the barren quartz vein and the country shale rock the Arakawa sample, f) Magnified image of studied chlorite in the Arakawa sample. Chl: chlorite, Qtz: quartz, Py: pyrite.

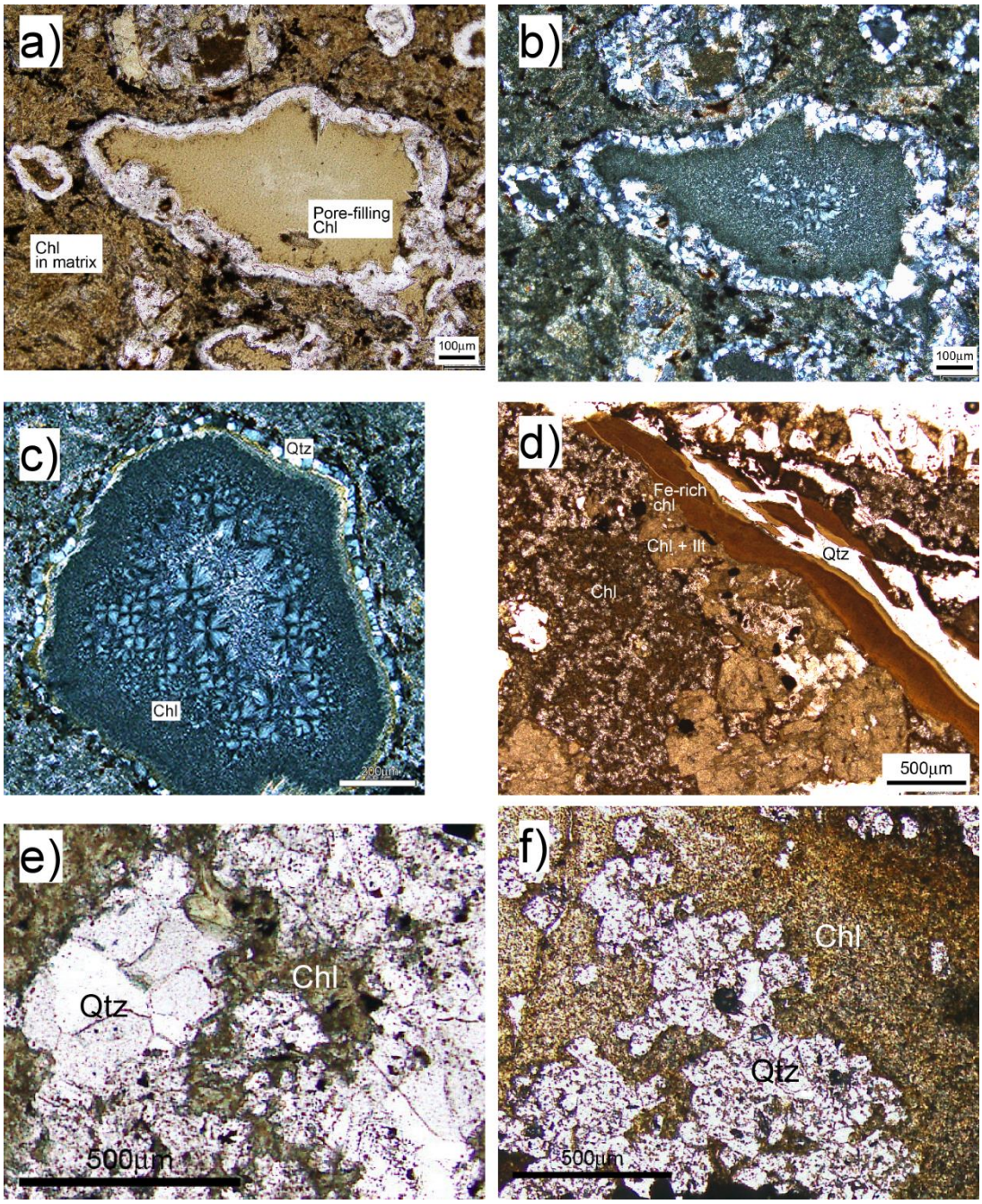

Figure III-2. a) pore-filling chlorites and chlorites in matrix of rock in TH-2-894 sample, b) photo of a) under cross-polarized light, c) pore-filing chlorites showing the spherulitic texture in TH-2-894 under cross-polarized light, d) a vein of Fe-rich chlorite in TH-2-680 sample, e) chlorites in quartz vein in the Soya sample, f) chlorites in quartz vein in Ashio sample. Chl: chlorite, Qtz: quartz.

Table III-1. Chemical composition of samples. Structural formulae were calculated on the basis of O= 14.

			Toyoha								Osarizawa			
	Ashio	STD[d]	Soya	STD	TH-2-680	STD	TH-2-894	STD	Arakawa	STD	Unotori	STD	Ishikirizawa	STD
SiO_2	21.62	0.36	22.51	1.35	24.85	1.14	26.12	1.49	31.02	1.75	28.95	0.93	28.59	0.50
Al_2O_3	22.46	0.53	20.02	0.86	16.65	2.29	18.01	0.66	23.77	1.79	17.38	0.64	16.22	0.63
FeO[a]	41.69	0.29	36.60	5.16	37.40	4.24	25.68	2.36	35.70	4.83	22.19	2.97	20.48	1.86
MnO	0.06	0.05	2.26	2.13	1.12	2.75	8.08	3.24	0.00	0.00	0.84	0.10	0.81	0.14
MgO	0.37	0.06	2.40	2.56	3.89	0.30	8.08	4.11	9.51	2.52	16.53	1.74	18.42	1.17
Total	86.21	0.93	83.79	4.24	83.90	1.89	85.98	1.02	100.00		85.88	2.97	84.53	1.26
Structure formula on the basis of O=14														
Si	2.56	0.02	2.70	0.04	2.97	0.12	2.94	0.07	2.93	0.10	3.06	0.05	3.05	0.02
Al(IV)	1.44	0.02	1.30	0.04	1.03	0.12	1.06	0.07	1.07	0.10	0.94	0.05	0.95	0.02
Tetrahedral cations	4.00		4.00		4.00		4.00		4.00		4.00		4.00	
Al(VI)	1.69	0.03	1.54	0.08	1.31	0.13	1.33	0.04	1.58	0.15	1.22	0.06	1.09	0.04
Fe^{2+}	4.12	0.05	3.69	0.57	3.76	0.56	2.43	0.30	2.84	0.47	1.96	0.25	1.83	0.18
Mn	0.01	0.01	0.22	0.20	0.11	0.03	0.78	0.33	0.00	0.00	0.07	0.01	0.07	0.01
Mg	0.07	0.01	0.42	0.43	0.68	0.46	1.33	0.63	1.33	0.32	2.60	0.25	2.93	0.15
Octahedral cations	5.89		5.87		5.86		5.87		5.75		5.85		5.92	
No. of vacancies	0.11		0.13		0.14		0.13		0.25		0.15		0.08	
Fe/(Fe+Mg)	0.98		0.90		0.85		0.65		0.68		0.43		0.38	
Formation T (°C)[b]	321	33	281	46	214	72	222	23	187	25	200	30	270	33
Th (°C)[c]	~300[e]		233	22	204	15	269	5	247	32	269	27	279	38

a: Total iron as FeO
b: Formation temperature estimated by chlorite geothermometer developed by Bourdelle et al. (2013)
c: Homogenization temperatures of fluid inclusions in quartz (unpublished data by A. Inoue)
d: Standard deviation
e: cited from Shikazono (2003)

III. 3. METHODS

The samples were gently crushed and sonicated in distilled water. The clay-sized fraction was separated by repeated decantation. Because the samples from Soya, Ishikirizawa, and Unotori contained significant amounts of impurities such as sulfide minerals, the clay fractions were further separated by Na-polytungstate densimetry (Cassagnabère, 1998). The separated clay suspension was sedimented onto glass slides and air-dried to prepare oriented mounts. Random powder mounts were prepared by the side-loading method (Moore and Reynolds, 1989).

Powder XRD patterns were acquired using a RINT-Ultima+ diffractometer (Rigaku) with a Cu X-ray tube, Ni filter, and silicon strip X-ray detector (Rigaku D/teX Ultra). Cu Kα radiation was produced at 40 kV and 30 mA. A measurement condition of 0.25° divergence slit, 10 mm mask confining the beam width, and 8 mm anti-scatter slit was used. The diffraction profile was obtained every 0.02° at a scan rate of 0.5° (2θ)/min.

Chemical analyses of the chlorites were performed on petrographic thin sections using a Kevex Sigma energy-dispersive X-ray spectrometer (EDS) attatched to a Hitachi S-4500 scanning electron microscope (SEM) with a cold field-emission gun operated at 15 kV.

TEM specimens were prepared using a focused ion beam (FIB) instrument with micro-sampling system (Hitachi FB-2100). Petrographic thin sections were cut into 5 mm squares to be accommodated in the FIB chamber, and coated with carbon to prevent charge accumulation on the surface of insulation minerals during the FIB process. In the FIB procedure, tungsten was deposited on the surface of the target area. Then trenches of about 5 μm in depth were formed around the target area with a high energy (30 keV)

Ga ion beam, and a fragment of each thin section was transferred onto a crescent-shape cupper grid using a micro-sampling system. The fragment was thinned to < 100 nm with a low energy Ga ion beam of 10 keV so as to minimize surface amorphization caused by the bombardment of Ga ion.

Specimens prepared by FIB were observed using a TEM (JEOL JEM-2010UHR,) operated at 200 kV with a nominal point resolution of ~ 0.2 nm. HRTEM images were recorded by a Gatan MSC 794 bottom-mounted CCD camera, then processed by a Wiener-filter (Marks, 1996; Kilaas, 1998), developed by K. Ishizuka (HREM Research Inc.), which was implemented in Gatan DigitalMicrograph to remove noisy contrast. Because the contrast in an HRTEM image is dependent on the sample thickness and defocus condition, HRTEM images were recorded at sufficiently thin areas of the TEM specimens and with a proper defocus condition to make suitable correspondence between the images and the crystal structures, following Kogure and Banfield (1998) and Kogure *et al.* (2001). HRTEM images were recorded along one of the Y_i directions (i= 1 to 3) (Figure II-2) to determine the polytypic groups of serpentine and chlorite layers (Kogure and Banfield, 1998; Kogure *et al.*, 2001).

III. 4. RESULTS

III. 4. 1. XRD

XRD patterns of oriented samples are shown in Figure III-3. All the samples contain some impurities such as illite, quartz, pyrite, and/or chalcopyrite. The 14 Å reflection of chlorite is present in all samples, but the intensity ratios of 001/002 reflections vary. Ethylene glycol treatment showed no expandable component; any large-space reflections diagnostic of regular interstratification were not observed in all samples.

The broadening in odd order 00*l* reflections which is diagnostic of 7Å-14Å interstratification was not clear in the studied samples (Figure III-3). Samples from Unotori, Ishikirizawa, Arakawa and TH-2-894 appeared to be chlorite dominated, whereas samples from TH-2-680, Soya, and Ashio consisted of berthierine ± chlorite ± berthierine-chlorite interstratification.

Figure III-3 shows XRD profiles of Unotori, Soya and Ashio samples in the range of 30-75 °2θ, together with calculated patterns with only *k* = 3n reflections (orthohexagonal cell setting) for I*bb* and II*bb* of Mg-chlorite and groups C and A of serpentine, using the structural parameters of Bailey and Brown (1962) and Bailey (1969). The XRD pattern of the Unotori sample is consistent with the structure of chlorite-II*bb* (Figure III-4) considering peak shifts by composition-dependent cell dimensions (see TableIII-1). Polytypic groups of Ishikirizawa, Arakawa and TH-2-894 chlorites were also assigned to II*bb* (data not shown here), although there was considerable interference from illite. The profiles of Soya, Ashio and TH-2-680 samples could not be assigned to a single type of polytypic group of serpentine or chlorite; they appeared to be a complex mixture of groups A and C of serpentine and chlorite-I*bb*.

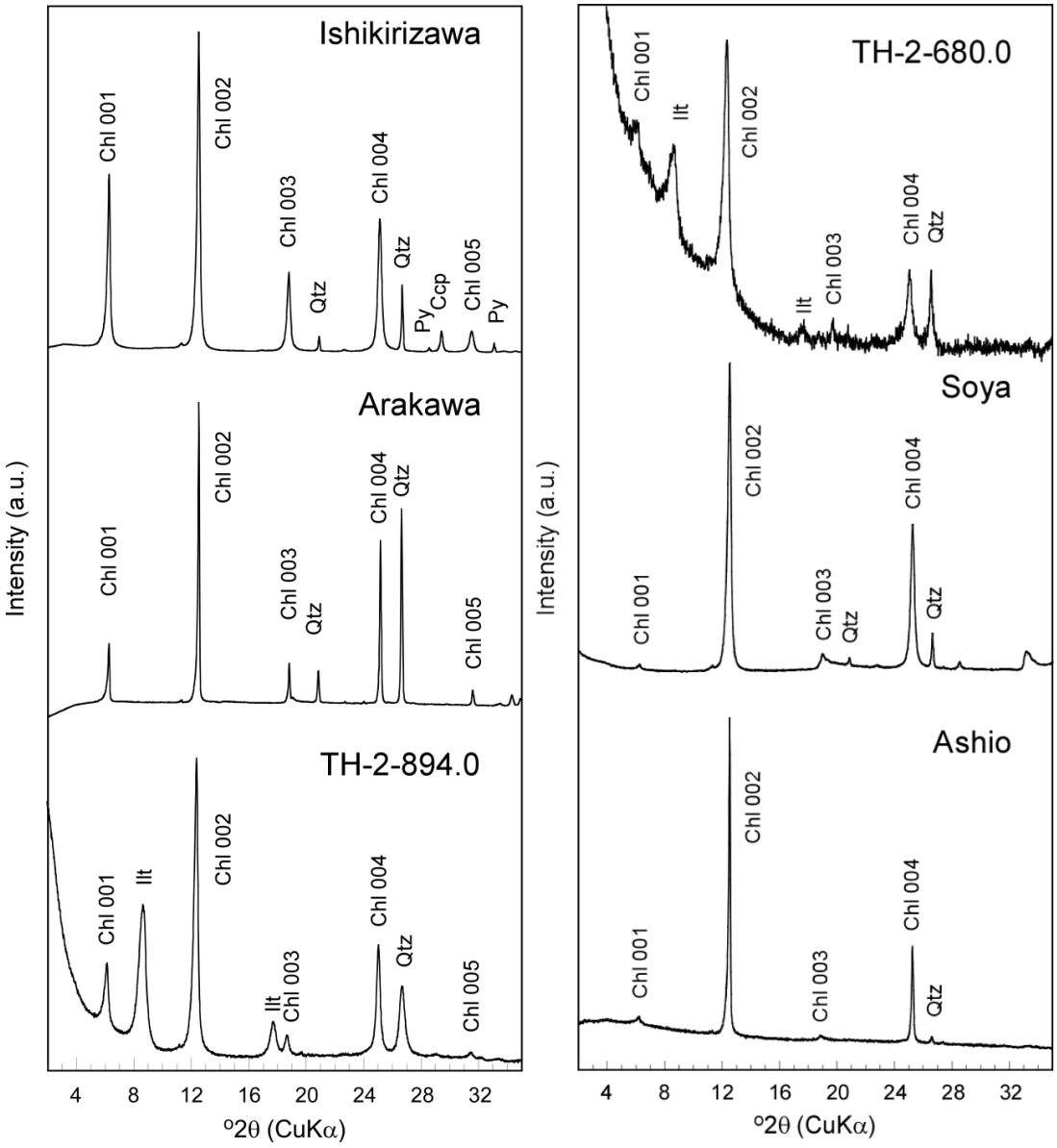

Figure III-3. One-dimensional powder XRD patterns of the chlorite samples. Chl: chlorite, Ilt: illite, Qtz: quartz, Py: pyrite, Ccp: chalcopyrite.

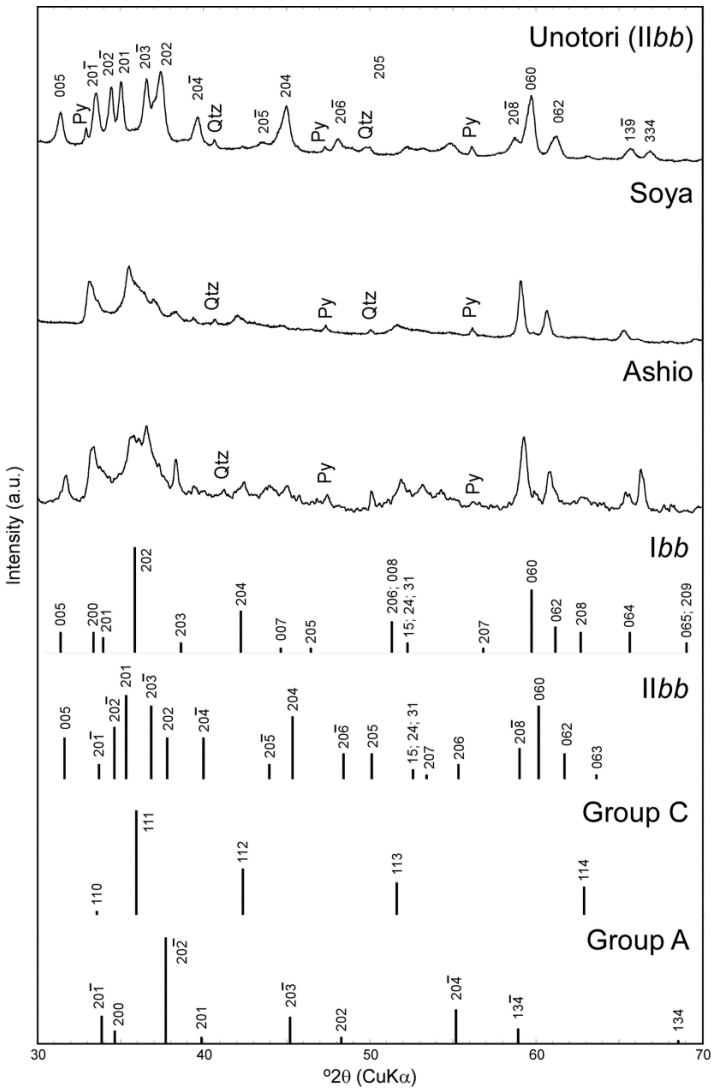

Figure III-4. Examples of powder XRD patterns from the randomly-oriented samples to identify polytypic groups and the position of peaks which are characteristics of representative polytypic groups of chlorite (I*bb* and II*bb*) and serpentine (groups C and A). Polytypic groups in parentheses are possible candidates for each sample. Qtz: quartz, Py: pyrite.

III. 4. 2. Chemical composition

Structure formulae were calculated based on 14 oxygen atoms and iron cations were regarded as divalent (Table III-1). Although the analyses occasionally showed large standard deviations in some samples, no zonation of elements was observed within a single grain of chlorite under SEM. The Fe/(Fe+Mg) ratios ranged from 0.38 to 0.98. TH-2-894 contained significant Mn compared to the other samples. Tetrahedral Al (Al(IV)) content was in the range of 0.94-1.44 atoms per formula unit (apfu). The

content paralleled to Fe/(Fe+Mg) ratios. In particular, the Ashio sample was characterized by large amounts of Fe(VI) (4.12 apfu) and Al(IV) (1.44 apfu). The composition may be compared with those of berthierine from the Kidd Creek volcanogenic massive sulfide ore deposit (Slack and Coad, 1989; Jiang, *et al.*, 1992; Slack, *et al.*, 1992) and from sedimentary rocks (*e.g.* Brindley, 1982; Iijima and Matsumoto, 1982), because a 7 Å reflection was dominant in the XRD patterns of the samples (see Figure III-3). The negative layer charge generated by Al substitutions for Si may be compensated by Al substitutions and small numbers of vacancies in the octahedral sheets (Brindley, 1982), though the ferric iron contents were not determined in the present study.

Bourdelle *et al.* (2013) proposed a geothermometer to estimate the temperature of chlorite formation using chemical composition without considering the effect of ferrous and ferric iron concentrations. Inoue et al. (2009) noted that their geothermometer is applicable to berthierine. Similarly, Bourdelle's geothermometer was applied to the present samples regardless of the interlayering of 7Å layers. The estimated temperatures of formation ranged from about 190 °C to 320 °C (Table III-1). The values were not so far from the respective homogenization temperatures of fluid inclusions in associated quartz. Bourdelle and Cathelineau (2015) proposed that the correlation between the chemical composition and the formation temperature are represented through isotherms on R^{2+} -Si plot (Wiewióra and Weiss, 1990). Such chemical characteristics of the samples are illustrated on Wiewióra-Weiss' diagram of Figure III-5 although the samples contain interlayering of 7Å layers. This result may justify the use of chlorite geothermometer to 7Å-14Å interstratified minerals. Despite the large standard deviation in both the formation temperatures and the homogenization temperatures of each sample,

it is evident that all the samples studied here formed at >190 ºC, the formation temperatures which are higher than those for sedimentary berthierine (*e.g.* Velde, 1985; Meunier, 2005).

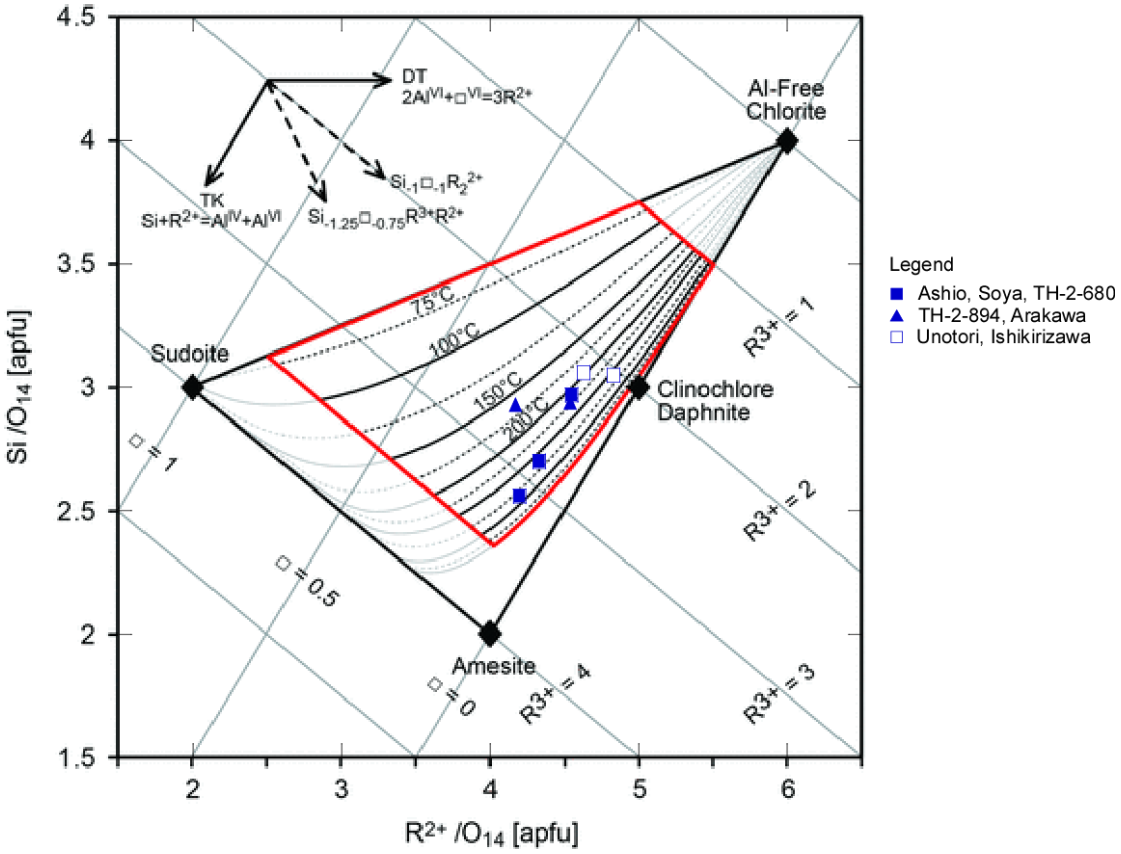

Figure III-5. R^{2+}-Si plot of Wiewiora and Weiss (1990) of samples overlaid on the representation of isotherms calculated with Bourdelle et al. (2013)'s geothermometer (Bourdelle and Cathelineau, 2015). The area shown in red suggested the area of optimal reliability for the geothermometer. Modified from Bourdelle and Cathelineau (2015) with permission from the Schweizerbart and Borntraeger science publishers (www.schweizerbart.de).

III. 4. 3. TEM

Low magnification HRTEM images of select samples are given in Figure III-6. Most samples were characterized by continuous, parallel stacks of layers without inclined contact with contiguous packets, as well as a few dislocations. In the samples with low

Fe contents (Fe/(Fe+Mg) ~ 0.4), Ishikirizawa and Unotori, 14Å layers predominated and 7Å layers were observed infrequently (Figures III-6a and b). Layers with 24 Å periodicity were observed in some chlorite packets of Unotori (Figure III-6b), which is probably a 1:1 regular interstratification of chlorite-smectite (*e.g.* Beaufort, *et al.*, 1997; Murakami, *et al.*, 1999; Kogure, *et al.*, 2013), because smectite layers shrunk to ~10 Å under vacuum conditions, and no K was detected by quantitative analysis by TEM-EDS. The frequency of 24Å layer was low, and hence it was not detected by XRD. The occurrence of 7Å layers was noticeable in samples with high Fe contents (Fe/(Fe+Mg) > 0.8), as represented by the Ashio sample (Figure III-6d). The proportion (%) of 7Å layers determined from a number of HRTEM images for each sample was nearly in proportion to the Fe content (Table III-1): from 0 % (Ishikirizawa), 0 % (Unotori), 8 % (Arakawa), 14 % (TH-2-894), 88 % (TH-2-680), 73 % (Soya), and 79 % (Ashio), and independent of the formation temperature (Figure III-5).

Figure III-7 shows selected area electron diffraction (SAED) patterns of Ishikirizawa, Arakawa and TH-2-680 along one of the Y_i directions. With increasing proportion of 7Å layers, the intensities of odd 00*l* spots for chlorite decreased. The reciprocal lattices in the patterns were oblique for Ishikirizawa and Arakawa (Figures III-7a and b). Polytypic groups of Ishikirizawa and Arakawa were assigned to chlorite-II*bb*; that of Unotori was also assigned to mainly II*bb*, but I*ba* stacking was locally observed in HRTEM images of the sample (Figure III-8). Assignment of the polytypic group of TH-2-680 (which was the same as for Ashio and Soya, though not shown here) from the SAED pattern was not possible because of intensive streaking along the c* direction (Figure III-7c). Hence, direct observations of the stacking structures by HRTEM are of great importance for these extremely Fe-rich samples.

The stacking structures in Ashio and Soya samples were disordered so that they were difficult to be described using conventional polytype notation such as I*bb* and II*bb* for chlorite layers or groups A and C for serpentine layers. This was because of the interstratification was at a fine scale and the 7Å layers occurred with many having opposite polarities (*i.e.* TO and OT) (Figure III-9). The lateral contacts of the opposite polar 7Å layers were observed on the HRTEM images (Figure III-9 and white boxes). To demonstrate the irregularity of such stacking structure completely, a new notation is proposed and the details of the stacking structure is further discussed below.

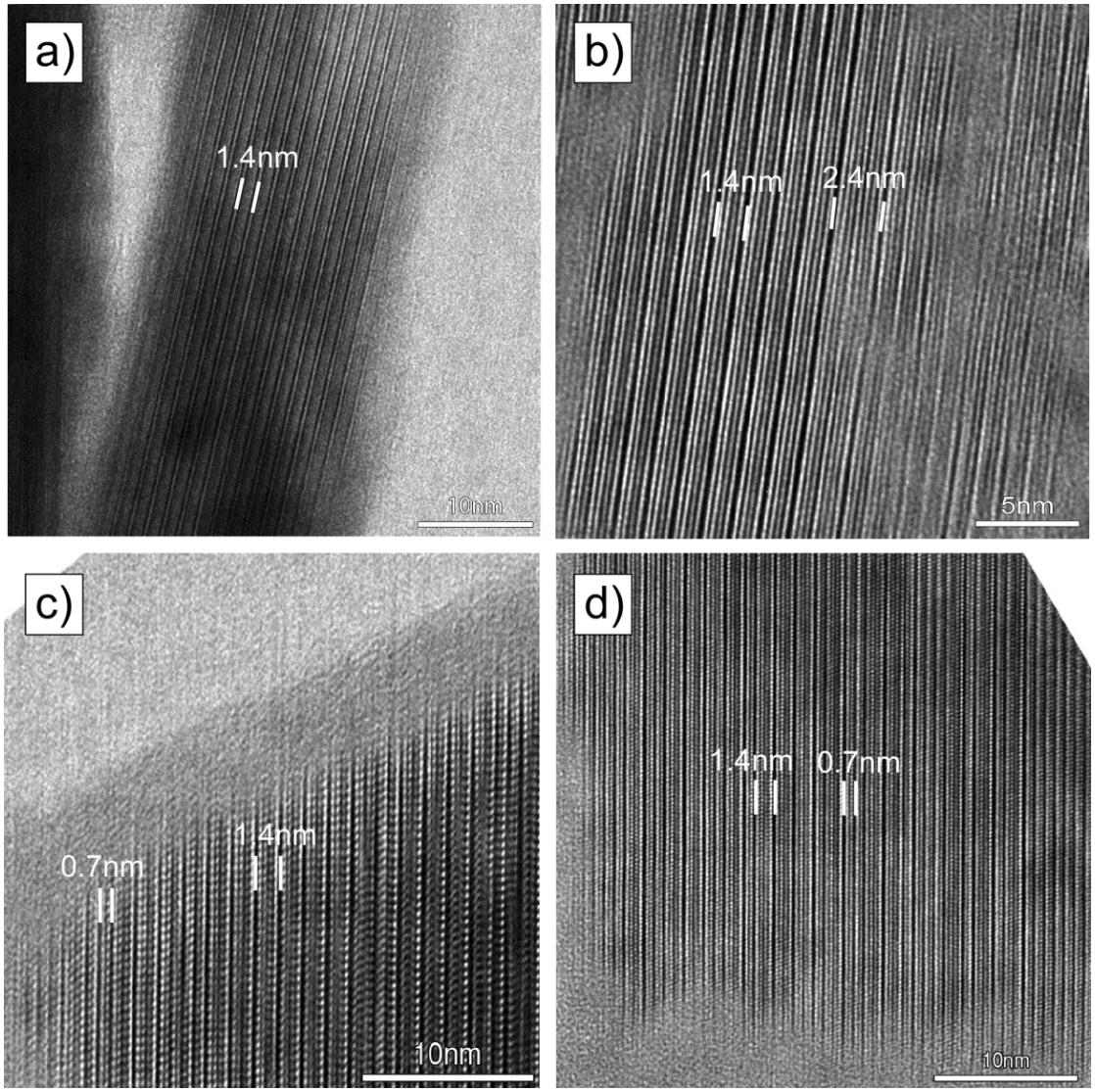

Figure III-6. HRTEM images with a relatively low-magnification, showing the layer stacking in the samples of (a) Ishikirizawa, (b) Unotori, (c) Arakawa, and (d) Ashio. Images in (a), (b) and (d) were recorded along one of the Y*i* directions and that in (c) along one of the X*i* directions.

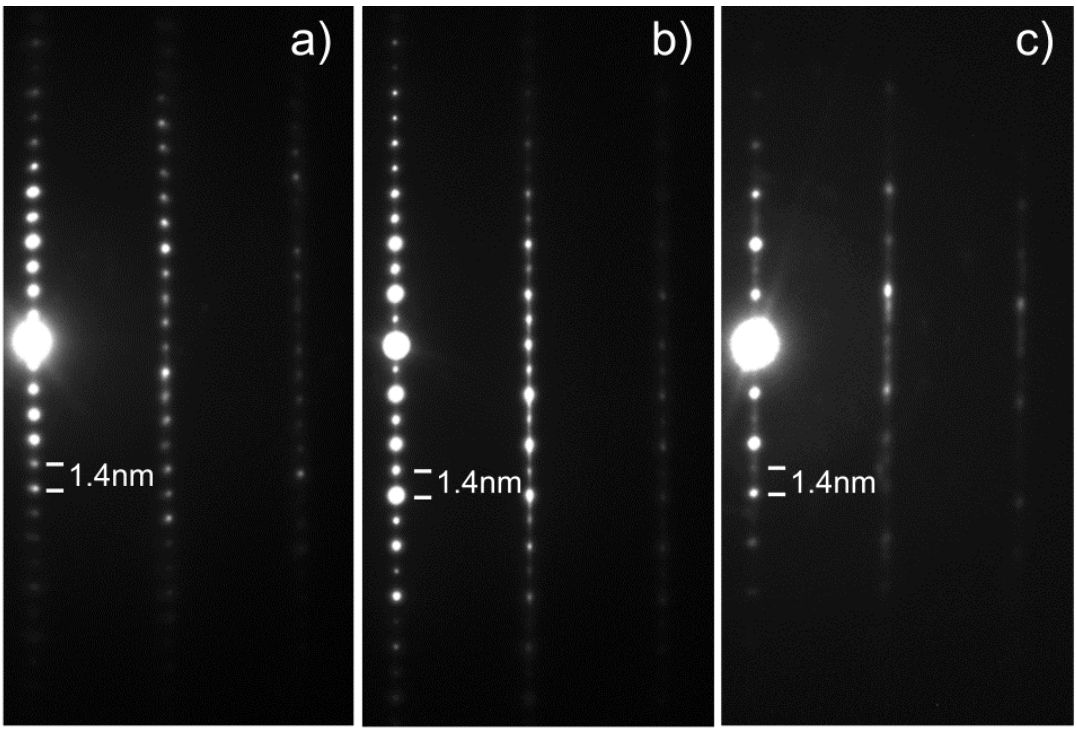

Figure III-7. SAED patterns of the several samples taken along one of the Y*i* directions. (a) Ishikirizawa. (b) Arakawa. (c) TH-2-680.

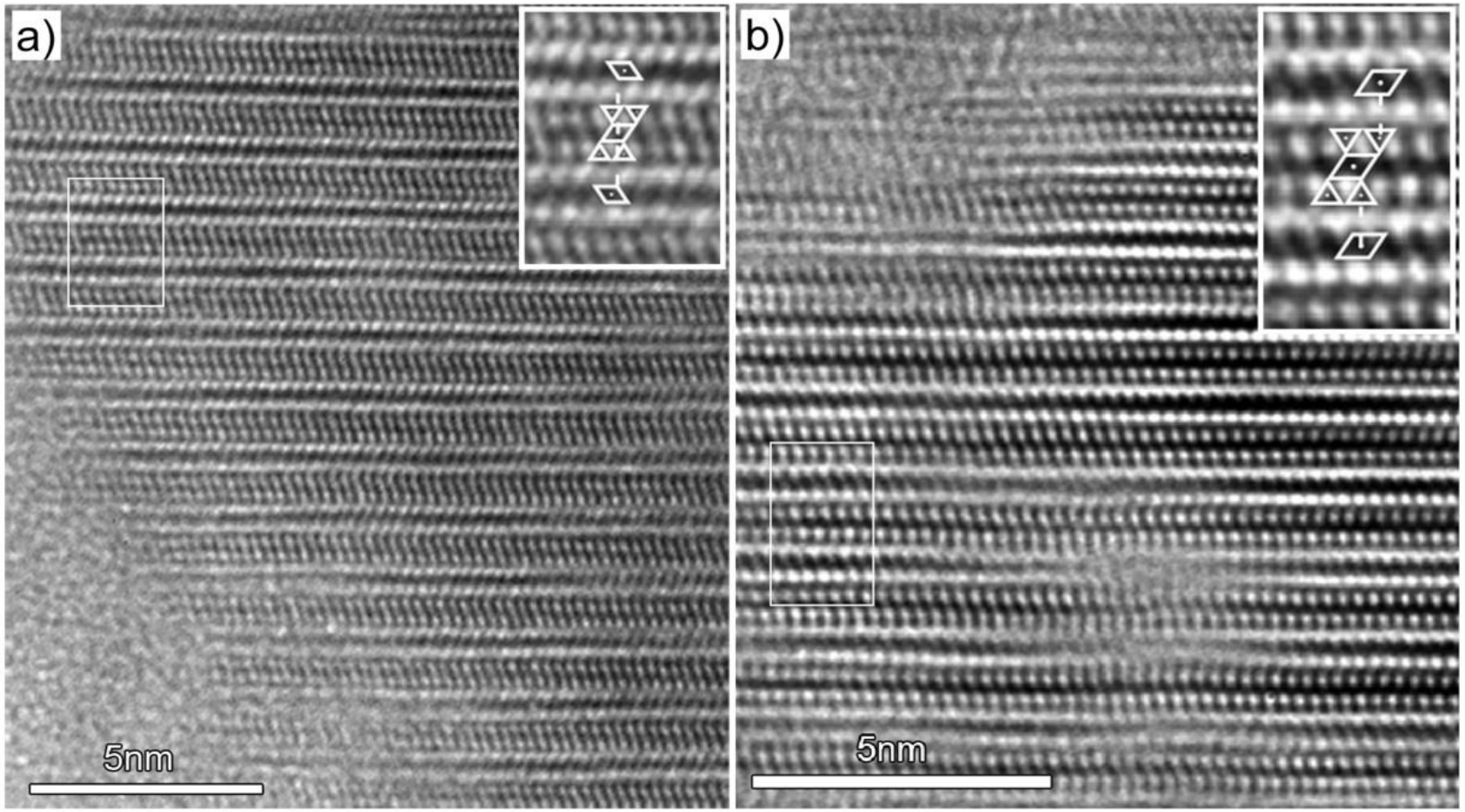

Figure III-8. HRTEM images recorded along one of the Y*i* directions of (a) chlorite-II*bb* of Ishikirizawa and (b) chlorite-I*ba* of Unotori. The inset images are the magnified images of the area indicated by white boxes with schematic diagrams showing the unit structure.

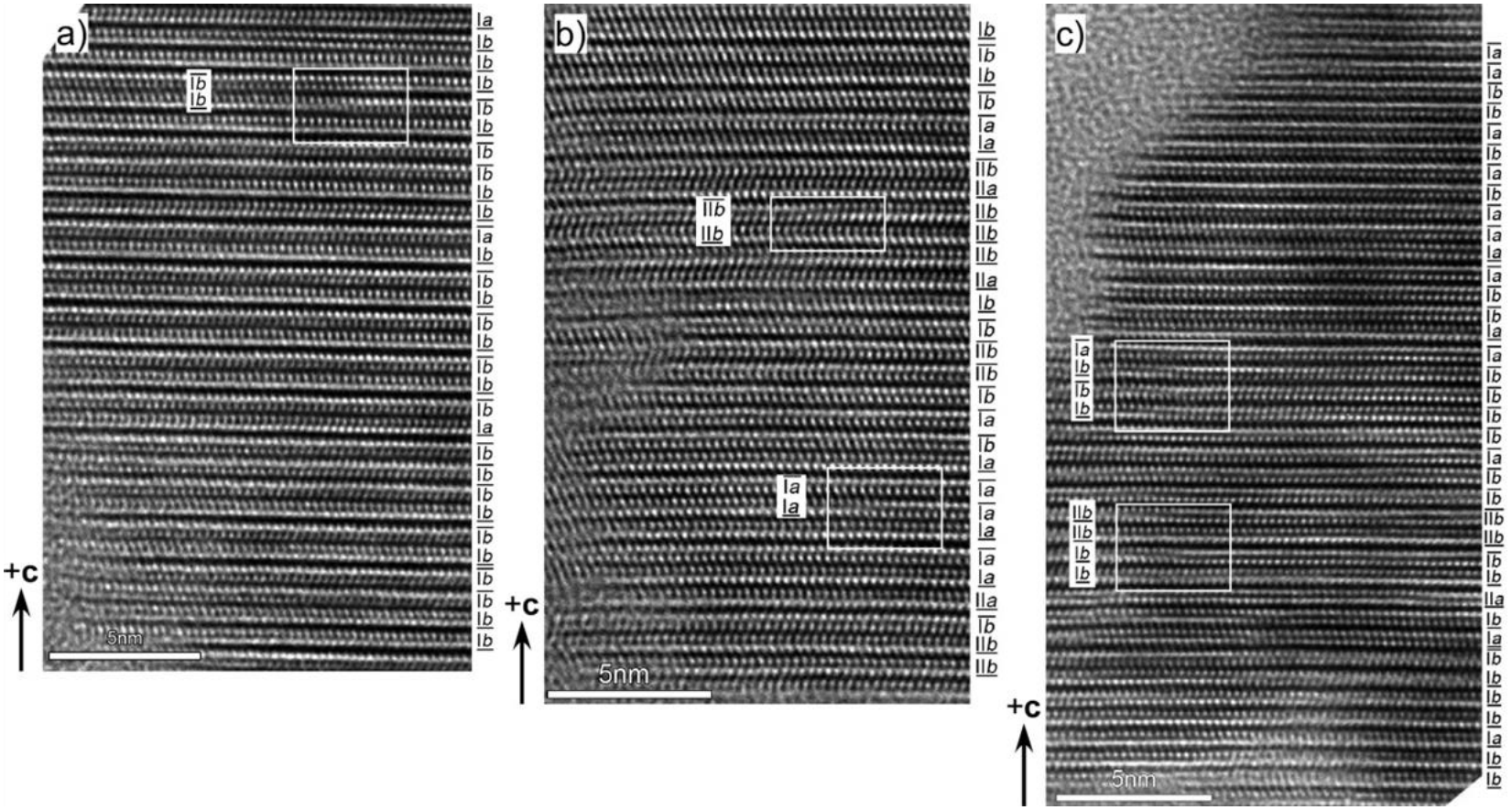

Figure III-9. HRTEM images recorded along one of the Y*i* directions of 7Å-14Å interstratified minerals of (a) Ashio, (b) Soya, and (c) TH-2-680. The symbol for the new notation method to describe the stacking structure of each layer is denoted at the right-hand side of the images (see text for detail), and white boxes on the images indicate the lateral contact of modules of opposite polarity.

III. 5. DISCUSSION

III. 5. 1. Layer stacking in interstratification

For the integrated description of the stacking for the interlayering of 7Å and 14Å layers at a fine scale, a new notation is employed. All the component layers are described as 7Å thick. Thus, the chlorite layer is divided into two modules when it was viewed along one of the Y_i directions: one module is between the cation plane of the upper B-sheet and that in the 2:1 layer, and another between the octahedral cation plane of the 2:1 layer and that of the lower B-sheet (Figure III-10). If the module contains the tetrahedral sheet by the **- c** axis oriented apical oxygens, it is termed the -c module and expressed by over-bar ($\bar{}$), and that with the **+ c** axis oriented apical oxygens is termed the +c module by under-bar ($\underline{\ }$) (Figure III-10). The octahedral slant of each module is defined following Bailey and Brown (1962). Hence, if the slant directions of the octahedral sheets at the lower and upper boundaries of the module are in the same direction, the structure of the module is defined as type I, and if they are anti-parallel, type II (Figure III-10). If the tetrahedral cations are located just above or below the octahedral cations across the hydrogen bonding, then the relationship between them is termed type *a*; and if the tetrahedral cations are laterally shifted relative to the octahedral cations, then it is type *b* stacking (Figure III-10). Using this notation, chlorite-I*bb*, and -c and +c serpentine of group C are expressed as $\overline{\mathrm{I}b}\underline{\mathrm{I}b}$, $\overline{\mathrm{I}b\mathrm{I}b}$ and $\underline{\mathrm{I}b\mathrm{I}b}$, respectively. The conventional polytypic notations for chlorite and serpentine can be described using the new notations (Figure III-10). Note that this notation is applicable to the stacking configurations that can only be observed in HRTEM, and is not applicable to the XRD data directly.

The stacking structures of interstratified minerals from Ashio, Soya and TH-2-680 are described using the present notation, as given in the right-hand side of the HRTEM images (Figure III-9). In the Ashio sample (Figure III-9a), both the -c and +c 7Å layers are found within a small packet in approximately equal proportion, but the two modules do not alternate as expected for pure chlorite. And the two modules link preferentially with the type I*b* stacking, although the stacking is locally perturbed by type I*a* (Figure III-9a). In the Soya sample, the proportion of -c and +c layers resembles that in Ashio (Figure III-8b). In contrast, the proportion in TH-2-680 is quite different and the amount of -c layers is almost twice of that of +c layers (Figure III-9c). Furthermore, different types of shift (*a* and *b*) and octahedral slant (I and II) mix irregularly in Soya and TH-2-680. The 14Å layer of $\overline{\text{II}}\overline{b}\underline{\text{I}}\underline{b}$ stacking, which cannot be categorized into any of the six polytypic groups, is observed in Soya (Figure III-9b). The irregularity is more obvious in Soya than in TH-2-680.

The degree of irregularity in layer stacking may be controlled by many factors, *e.g.* chemical composition, formation temperature, transformation mechanism, and kinetics of mineral precipitation such as crystal growth rate and mechanism. The data (Table III-1) indicate that the Fe/(Fe+Mg) ratio and the Al(IV) content decrease in the order of Ashio, Soya and TH-2-680 and the formation temperatures of these samples ranged from 190 to 300 ºC. The order of the Fe/(Fe+Mg) ratio and the Al(IV) content is inconsistent with the order of increasing irregularity; hence, the three factors, Fe/(Fe+Mg), Al(IV) and temperature, can be excluded from the principal causes of the irregularity. The mechanism and the rate of crystal growth are suspected to be the main causes of formation of the complex irregularities in the stacking of 7Å and 14Å layers because the hydrothermal chlorites are not transformation products from any precursor

minerals.

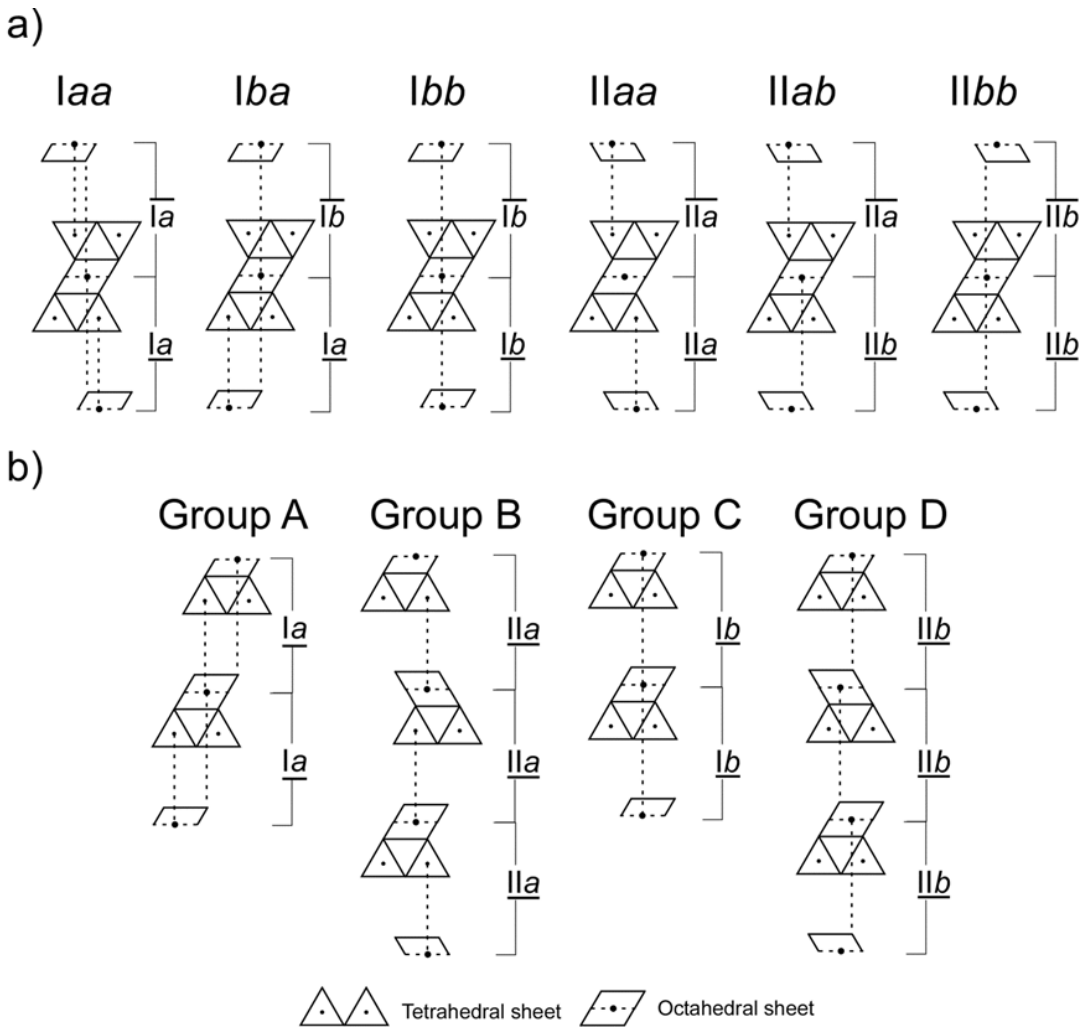

Figure III-10. Schematic diagrams showing the correspondence between polytypic notations proposed in this study and that of Shirozu and Bailey (1965) for (a) chlorite, and Bailey (1969) for (b) serpentine.

III. 5. 2. Lateral relation between 7Å and 14Å layers

Considering the transformation mechanism between 7Å and 14Å layers, Baronnet (1992) noted that if the serpentine-chlorite interstratified mineral is in an intermediate stage of topotactic transformation from serpentine to chlorite (or vice versa), the polytypic group of the reactant phase must be inherited by the product phase. Many studies have used the β angle as measured on SAED patterns to identify the transformation mechanism (*e.g.* Jiang, *et al.*, 1992; Banfield and Bailey, 1996; Xu and Veblen, 1996). In the cases where the β angle of serpentine is 90º in the transformation from serpentine to chlorite, for instance, Xu and Veblen (1996) simply assumed that serpentine-2*H* (group D) transformed to chlorite-II*ab*, thereby maintaining β=90º. Using the present notation method, the transformation is described from $\overline{\text{II}b\text{II}b\text{II}b}$ to $\overline{\text{II}a}\underline{\text{II}b}$. Note that II*ab* is not a stable polytypic group of chlorite as described in Chapter II. 3. Banfield and Bailey (1996), therefore, constructed another structure model to explain the transformation from serpentine of group D to chlorite-I*bb* ($\overline{\text{II}b\text{II}b\text{II}b}$ to $\overline{\text{I}b}\underline{\text{I}b}$ by the present notation) by changing the direction of octahedral slant at the lateral contact between 7Å and 14Å layers. In the present study, the lateral contact was infrequently observed in the interstratified structure as described above (for example, white boxes in Figure III-9). The lateral contacts are expressed as $\overline{\text{I}b}\underline{\text{I}b\text{I}b}$ and $\overline{\text{I}b\text{I}b}\underline{\text{I}b}$ in Ashio, $\overline{\text{II}b}\underline{\text{II}b}$ and $\underline{\text{II}b\text{II}b}$, and $\overline{\text{I}a\text{I}a}$ and $\underline{\text{I}a\text{I}a}$ in Soya, and $\overline{\text{I}a}\underline{\text{I}b}\overline{\text{I}b}\underline{\text{I}b}$ and $\overline{\text{I}a\text{I}b\text{I}b}$, and $\underline{\text{II}b\text{II}b\text{I}b\text{I}b}$ and $\overline{\text{II}b}\underline{\text{II}b}\overline{\text{I}b}\underline{\text{I}b}$ in TH-2-680. Close examination of HRTEM images reveals that the model of Xu and Veblen (1996) applies successfully to the stacking structure of 7Å and 14Å layers, whereas the alternative model of Banfield and Bailey (1996) is not applicable to the three samples. On the basis of Banfield and Bailey (1996), the type I*a* stacking in 7Å layers is required to convert into the type I*b* stacking in adjacent 14Å layers.

In the Soya sample, the stacking structure of 7Å layer succeeds continuously to that of 14Å layer by way of the mode of I*a* type stacking at both the left-hand and right-hand sides of the lateral contact fronts (Figure III-11b). Consequently, along with the severely disordered stacking in vertical direction as discussed above, the above observations of the lateral contact imply that the stacking relation between 7Å and 14Å layers as the components in the interstratification cannot be explained by the inheritance of polytypic groups during a solid-state transformation. On the contrary, the interstratified minerals of 7Å and 14Å layers observed in the present study are not products of an intermediate stage of topotactic transformation between the two minerals as described by Baronnet (1992), Xu and Veblen (1996) and Banfield and Bailey (1996).

It should be kept in mind that the present study assumed that the chemical compositions of each component layer are the same. It is highly possible that there are differences in chemical compositions of the component layers and atomic scale chemical heterogeneities within each component layer. Further characterizations of individual component layers from the viewpoint of the chemical heterogeneity will be beneficial to clarify the genesis of the samples.

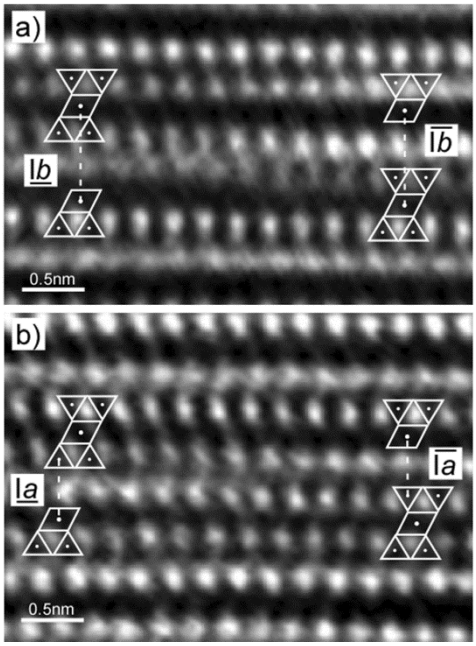

Figure III-11. Magnified image of the lateral contact in (a) Ashio and (b) Soya. The schematic diagrams correspond to the stacking structure are overlaid on HRTEM images.

III. 5. 3. Geological implication

The petrographic microscopic and TEM observations suggested that each chlorite sample studied here precipitated in veins directly from solutions, and were not affected by later modifications (*e.g.* Inoue *et al*., 2010; 2012). The formation temperatures were > 190 °C determined from homogenization temperatures of fluid inclusions in associated quartz and chlorite geothermometry (Table III-1). Because of the relatively high temperature precipitation of chlorites, the followings were recognized: the component layers in chlorites with low Fe content (*e.g.* Ishikirizawa and Unotori) were basically 14Å layers. Each structure was polytype II*bb* which is the most stable structure of chlorite (Bailey, 1988a). Interlayering with different component layers was observed locally in HRTEM images although the frequency was as low as not detected by XRD. One of the component layers appeared to be dehydrated smectite of 10Å, and the resultant interstratified structure involved the two component layers formed a

regularly interstratified structure with 24Å fringes like corrensite. This type of interstratification has been documented in the saponite-to-chlorite series in various geologic regimes (*e.g.* Hillier, 1993; Beaufort, *et al.*, 1997; Murakami, *et al.*, 1999; Kogure, *et al.*, 2013).

In contrast, the present study highlighted that the proportion of 7Å layer increases with increasing Fe content, and the number of 7Å layer can be > 80 % near the Fe-end member. The chemical composition of 7Å layer approximated Fe-rich berthierine. Berthierine is common in sedimentary rocks and is probably a precursor of chamosite during burial diagenesis. Natural occurrences show that the transformation of berthierine to chamosite occurs over a wide temperature range from 70 °C to 200 °C during burial diagenesis (*e.g.* Velde, 1985; Jahren and Aagaard, 1989; Hornibrook and Longstaffe, 1996). Aagaard *et al*. (2000) indicated that the transformation temperature is around 90 ºC. Experiments at relatively low temperature conditions (*e.g.* Mosser-Ruck, *et al.*, 2010) demonstrated that berthierine was stable at low temperatures and transforms to chamosite at temperatures higher than 200 °C. In addition, high temperature and pressure experiments on the stability of Fe-rich chlorite, including Fe-amesite composition (*e.g.* Chernosky *et al.*, 1988; Parra *et al.*, 2005; Vidal, 2005 and references therein), also suggested that the 7Å phase appeared as a metastable phase and finally transformed to 14Å chlorite following the Ostwald step rule. More recently, Blanc et al. (2014) indicated, from their calorimetric measurements of Fe-rich chlorite and berthierine, that berthierine might transform into chlorite at higher temperatures, but the transformation temperature is dependent on the chemical composition of the two minerals. Although the thermal stability of berthierine is not resolved, the Fe-rich berthierine studied here precipitated as a metastable phase from solutions based on the

intensive irregularity of layer stacking as observed under HRTEM. Nevertheless, the fact that Fe-rich berthierine formed at higher temperatures than those in sedimentary environments indicates the necessity to reconsider the thermal stability of Fe-rich berthierine.

III. 6. SUMMARY AND CONCLUSION

The present HRTEM study of chlorites which precipitated at temperatures roughly from 200 °C to 300 °C in quartz veins of hydrothermal ore deposits led to the following conclusions:

• Low magnification HRTEM images showed that most of the samples made an interstratification between 7Å, 14Å, and sparingly smectite layers. The proportion of 7Å layers increased progressively with Fe content.

• From the chemical point of view, the 7Å layer is close to Fe-berthierine. Berthierine has been considered to be characteristic of sedimentary rocks and may be a lower temperature phase compared to chlorite. However, our results suggest that Fe-berthierine precipitated at relatively higher temperatures from solutions. Actually the thermal stability of Fe-berthierine has not been comprehended yet, and thus further work will be needed.

Chapter IV: HIGH-ANGLE ANNULAR DARK FIELD SCANNING TRANSMISSION ELECTRON MICROSCOPY (HAADF-STEM) STUDY OF OCTAHEDRAL FE AND AL DISTRIBUTION IN FE-RICH 7Å-14Å INTERSTRATIFIED MINERALS

IV. 1. INTRODUCTION

IV. 1. 1. Chapter introduction

In the previous chapter, the author characterized the structures of so-called Fe-rich chlorites from several hydrothermal ore deposits using HRTEM. The stacking structures of the samples with Fe/(Fe+Mg)>0.9 were characterized by disorder of 7Å and 14Å layers, difference in the polarity of the tetrahedral sheet, variation of the slant of octahedral sheets, and positional disorder between octahedral and tetrahedral sheets in HRTEM images recorded along one of the Y_i directions. Moreover, lateral contacts of the tetrahedral sheets of opposite polarity were frequently observed. Such lateral arrangements of 7Å and 14Å layers were observed in previous HRTEM studies of 7Å mineral to 14Å mineral transformation (*e.g.* Banfield and Bailey, 1996; Xu and Veblen, 1996). The results of Chapter III implied that high Fe content in the samples may influence the formation of the complex stacking structures. To date, the structure of Fe-rich 14Å chlorite and 7Å berthierine has not been understood compared to their Mg-endmember (*e.g.* Bailey, 1988a, c). This is also the case for the component layers of the interstratified minerals, because Fe-rich chlorite is usually characterized by fine grain-size which makes XRD refinement difficult. As shown previously, HRTEM has contributed significantly to overcoming such difficulty. A recent imaging technique,

called HAADF-STEM, has an ability to obtain the information about cation distributions in the octahedral sheets of phyllosilicate minerals (*e.g.* Kogure and Drits, 2010; Kogure and Okunishi, 2010; Okumura, *et al.*, 2014). In HAADF-STEM image, the image contrast is roughly proportional to the Z^2 (Pennycook and Jesson, 1992). The octahedral cation distributions in samples with Fe/(Fe+Mg)>0.9 were investigated by a combination of the HAADF-STEM observations and the image simulations viewed from one of the X_i directions (i=1-3) (Figure II-2).

IV. 1. 2. Brief summary of HAADF-STEM

STEM is, in brief, expressed as a combination of scanning electron microscopy (SEM) and TEM. The STEM image is formed with the very finely focused electron beam scanned over the sample (Pennycook and Nellist, 2011 and reference therein). The beam spreading of the sample is small in a very thin specimen, and hence the spatial resolution is mainly controlled by the probe size. In recent years, the development of the spherical aberration (Cs) corrector dramatically improves the spatial resolution of STEM.

There are different types of signals which can be detected by STEM: (i) the transmitted electrons that leave sample at relatively small angle with respect to the optic axis (bright field: BF), (ii) those that leave sample at high angle with respect to the optic axis (annular dark field: ADF), (iii) those lose a measurable amount of energy as they pass through the sample (which are related to electron energy loss spectroscopy: EELS), and (iv) X-ray which is emitted by the electron excitation in sample (energy dispersive X-ray spectroscopy: EDS). In this study, high-angle ADF- (HAADF) and BF-STEM were used. The BF-STEM image is equivalent to the HRTEM image based on the

principle of reciprocity (Cowley, 1969). The ADF imaging uses a signal detected by an annular detector placed above the specimen in the STEM. The contrast of ADF image is proportional to the intensity of scattering which leads to the atomic number contrast (Z-contrast). The ADF imaging can be described as being incoherent. It means that the contrast reversal due to the phase contrast caused by changes in defocus and specimen thickness is almost negligible in ADF-STEM. Such characteristic makes ADF-STEM useful for the atomic scale observations. In ADF-STEM of a zone-axis crystal, however, the effects of diffraction contrast becomes higher, and hence, the realization of Z-contrast image becomes difficult. In HAADF-STEM, the annular detector is placed at higher angle where thermal diffuse scattering due to thermal vibration of the atoms is dominant, in other words, the scattered electron is no longer coherent. Consequently, the contrast in HAADF-STEM image is almost proportional to Z^2 (Pennycook and Nellist, 2011).

IV. 2. SAMPLES AND METHODS

IV. 2. 1. Samples

Studied samples are two 7Å-14Å interstratified minerals from Soya vein in the Toyoha deposit, Hokkaido and the Ashio deposit, Tochigi, Japan. They will be called the Ashio and Soya samples hereafter. Details of the samples are summarized in the previous chapter.

IV. 2. 2. HAADF-STEM

STEM specimens were prepared using a FIB apparatus with micro-sampling system following the procedure described in the previous chapter.

STEM observations were carried out on two apparatus, a JEOL JEM-2800F without a Cs-corrector and JEOL ARM-200F with a Cs-corrector for the probe-forming lens. Both apparatuses are equipped with Schottky-type field emission electron guns operated at 200 kV. The image resolution expected for the STEM image is 2 Å with JEM-2800F and 0.8 Å with ARM-200F. Beam convergence semi angle of the probe is 8.8 mrad for JEM-2800F and 24 mrad for ARM-200F. The detection semi-angles of the HAADF-detector for JEM-2800F and ARM-200F are between 55 (inner) and 248 (outer) mrad and between 68 (inner) and 280 (outer) mrad, respectively. Images taken with JEM-2800F are referred to as "Cs-uncorrected" and those with ARM-200F are referred to as "Cs-corrected" throughout this study. Recorded HAADF images were processed to remove noisy contrast by a Wiener-filter (Marks, 1996; Kilaas, 1998) developed by K. Ishizuka (HRTEM Research Inc.) which was implemented in a Gatan DigitalMicrograph (Kogure and Okunishi, 2010). All images were recorded along one of the X_i directions.

IV. 2. 3. HAADF-STEM image simulations

HAADF images were simulated to compare with observed images using the FFT multislice method (Ishizuka, 2002; xHREM, HREM Research Inc.) developed by K. Ishizuka. Calculations were based on the structure models of chlorite-I*bb* (Bailey and Brown, 1962) and serpentine of polytype 1*T* (Bailey, 1969). All structural parameters were converted to those of *P*1 symmetry. The values described above were input for optic and detector parameters of HAADF-STEM throughout the simulations.

Figure IV-1 shows simulated HAADF images of 14Å Fe-chlorite ($(Fe_5Al)(Si_3Al)O_{10}(OH)_8$) in the two cases, Cs-corrected and Cs-uncorrected images, along with the

corresponding crystal structure. All octahedral sites in chlorite structures can be recognized as the individual columns of 1.5Å periodicity if the structure is viewed along one of the X_i directions. In the simulations it was assumed that octahedral Al preferentially occupies the M4 site; tetrahedral Si and Al are randomly distributed to the T sites (*e.g.* Bailey, 1988a; Welch, *et al*., 1995). Brighter lines correspond to the octahedral sheets which mainly contain Fe and Al, and darker arrays that present between octahedral sheets correspond to the tetrahedral sheets which are composed of Si and Al. The octahedral sheets which are closer to two tetrahedral sheets correspond to those in the 2:1 layer (called O-sheet hereafter), and those which are apart from the tetrahedral sheets are B-sheet. It is noticed that M1, M2 and M3 sites, which are occupied by Fe, exhibit brighter contrast than M4 site in which Al predominates. The M1, M2 and M3 sites are not distinguished on the Cs-uncorrected HAADF-STEM images, whereas, all the octahedral sites are resolved as an array of spots on the Cs-corrected HAADF-STEM image. Image does not reverse contrast at any defocus value and sample thickness (Figure IV-2). For the image simulations of defocus value was set to -3 nm.

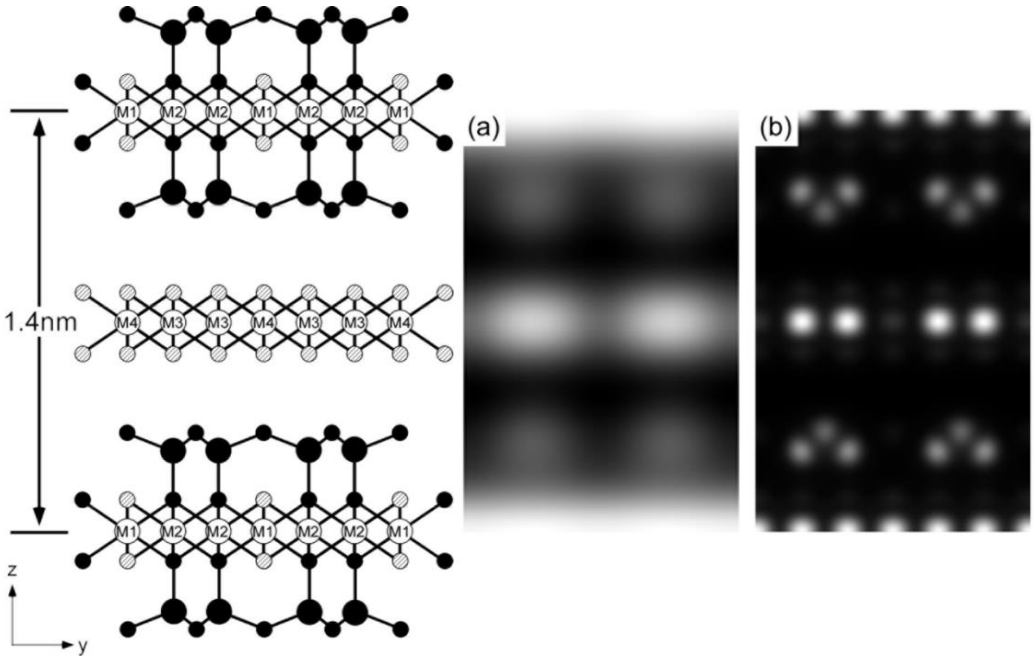

Figure IV-1. Simulated Cs-uncorrected (a) and Cs-corrected (b) HAADF-STEM images of chlorite ($(Fe_5Al)(Si_3Al)\ O_{10}(OH)_8$) and corresponding crystal structure viewed along one of the X_i directions (i=1-3).

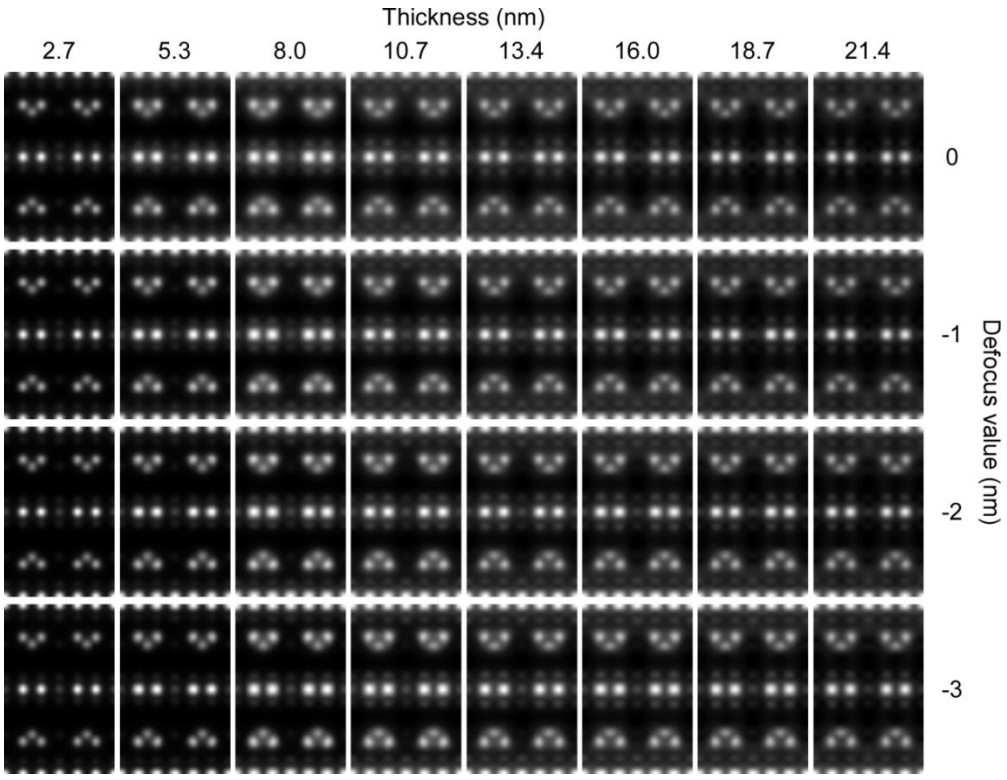

Figure IV-2. The simulated Cs-corrected HAADF-STEM images of chlorite as functions of sample thickness and defocus value.

IV. 3 RESULTS AND DISCUSSION

IV. 3. 1 Distribution of octahedral Fe and Al in14Å layer

Figure IV-3 shows a Cs-uncorrected HAADF image of the Ashio sample after filter-processing. Two types of the octahedral sheets are distinguished in terms of the contrast profile; the O-sheet exhibits a nearly continuous bright line, while discontinuous contrast is apparent in the B-sheet. Such features become even clearer in Cs-corrected images (Figure IV-4). The octahedral sites in the O-sheets exhibit an array of spots with almost equal contrast, while regular repetition of two brighter and one relatively darker spots is apparent in the B-sheet. Compared with the crystal structure of chlorite, the darker spots are assigned to the M4 sites in the B-sheet, which suggests that the M4 sites are occupied by atoms with Z lower than those occupy the other M1, M2, and M3 sites. This assignment was confirmed by the image simulations (Figure IV-5).

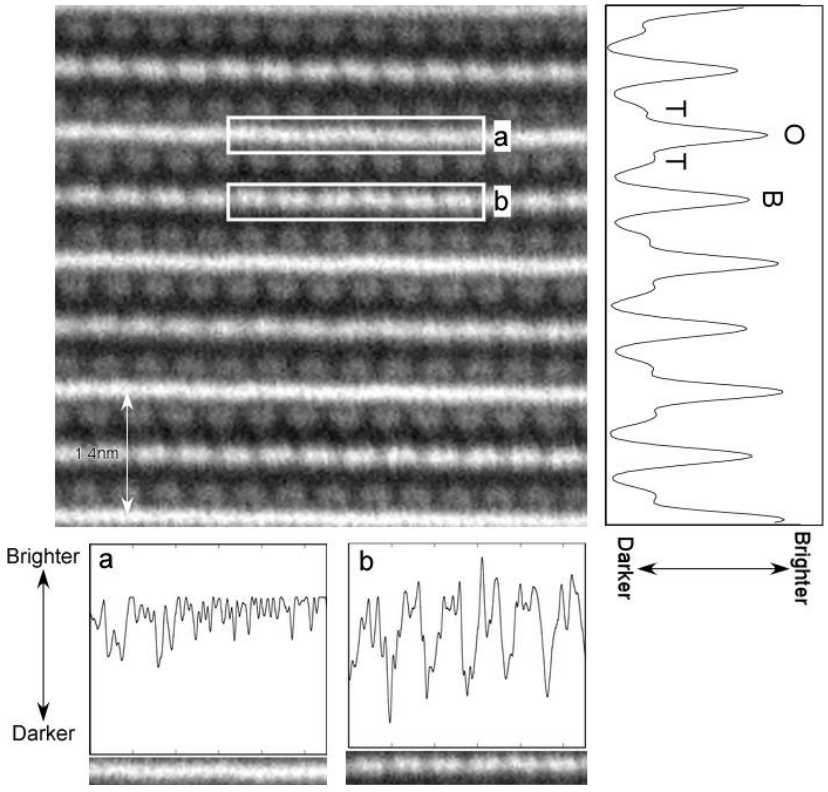

Figure IV-3. Cs-uncorrected HAADF-STEM image of 14Å layers of the Ashio sample viewed along one of the X_i directions, contrast profiles measured from areas in boxes a and b and the integral contrast profile of the image perpendicular to the stacking direction. T: tetrahedral sheet, O: the O-sheet in the 2:1 layer, B: the B-sheet.

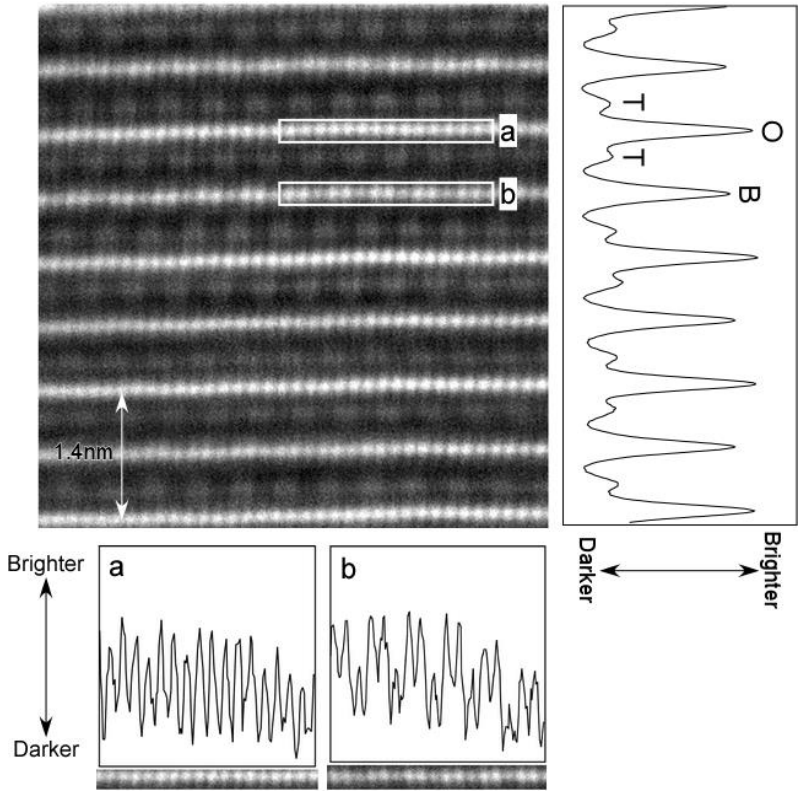

Figure IV-4. Cs-corrected HAADF-STEM image of 14Å layers of Ashio viewed along one of the X_i directions, and contrast profiles measured from areas in boxes a and b and the integral contrast profile of the image perpendicular to the stacking direction.

Concerning the compositional difference between the O- and B-sheets, the contrasts of the O-sheet and B-sheet were integrated along the sheets on experimental images (Figures IV-3 and 4). The integrated contrast of the B-sheet was always darker than that of O-sheet. The ratio of the integral contrast of the B-sheet to the O-sheet for both of images was about 0.8, suggesting that octahedral Al is preferentially accommodated in the B-sheet.

The structure formula of the Ashio sample approximated as $(Fe^{2+}_{4.08}Fe^{3+}_{0.22}Al_{1.5}\square_{0.2})(Si_{2.5}Al_{1.5})O_{10}(OH)_8$, ignoring the presence of Mg and Mn in Table III-1. The HAADF-STEM images based on the formula were simulated to recognize the position

of the M4 site for Cs-corrected HAADF-STEM (Figures IV-5). Upon simulating the images, it is required to distinguish ferrous and ferric irons in order to estimate the numbers of vacancies. Inoue *et al.* (2009) and Bourdelle *et al*. (2013) proposed chlorite geothermometers using chemical composition data. The Inoue's method requires the data of ferric iron content, whereas Bourdelle's one does not require those. Nevertheless, the two methods provide similar estimates of the formation temperatures. If this is the case, assuming that the formation temperatures estimated by Bourdelle's method are the same as those by Inoue's, estimated $Fe^{3+}/\Sigma Fe$ was 0.05. Accordingly, the following two types of octahedral cation distributions were assumed in the simulations:

(a) $(Fe^{2+}_{2.45}Fe^{3+}_{0.13}Al_{0.30}\square_{0.12})_{M1+M2}$ $(Fe^{2+}_{1.63}Fe^{3+}_{0.09}Al_{0.20}\square_{0.08})_{M3}(Al)_{M4}$,

(b) $(Fe^{2+}_{2.45}Al_{0.43}\square_{0.12})_{M1+M2}$ $(Fe^{2+}_{1.63}Al_{0.29}\square_{0.08})_{M3}(Fe^{3+}_{0.22}Al_{0.78})_{M4}$.

Differences in contrast between the two octahedral sites of M1-M4 are evident regardless of sample thickness and M4 site compositions (Figures IV-5). Namely, the contrast of M4 sites becomes higher with increasing Fe content in M4 site compared to M3 sites. The ratios of M4 to M3 calculated from Z^2 for the above two types were 0.3 and 0.5 respectively. This is similar to the intensity ratio of M4 to M3 measured on simulated image (Figure IV-5). The difference in contrast between M4 and M3 sites was slightly lower in the experimental Cs-corrected HAADF-STEM image than those in the simulated images (Figures IV-3 and 4), although the actual intensity ratio was dependent on the sample thickness. It suggests that small amounts of Fe are actually present in the M4 sites in addition to dominant Al. Previous XRD, NMR and MS studies of clinochlore indicated that trivalent cations preferentially occupy the M4 site (e.g. Bailey, 1988a). In addition, the calculation of the interlayer bonding energy of clinochlore-II*bb*

suggested that the ordering of trivalent cations into the M4 site increase the stability of the structure (Bish and Giese, 1981). Accordingly, it is deduced that iron occupied in the M4 sites is mostly ferric although ferrous and ferric irons cannot be distinguished in the HAADF-STEM images. In type (b) model of the octahedral cation distribution described above, the ferrous Fe and the excess of Al were partitioned in M1, M2 and M3 sites at equal proportion. The calculated ratio between Z^2 of the B-sheet to the O-sheet for this type was 0.73 which is close to the contrast ratio (0.8) between the two sheets in the experimental image.

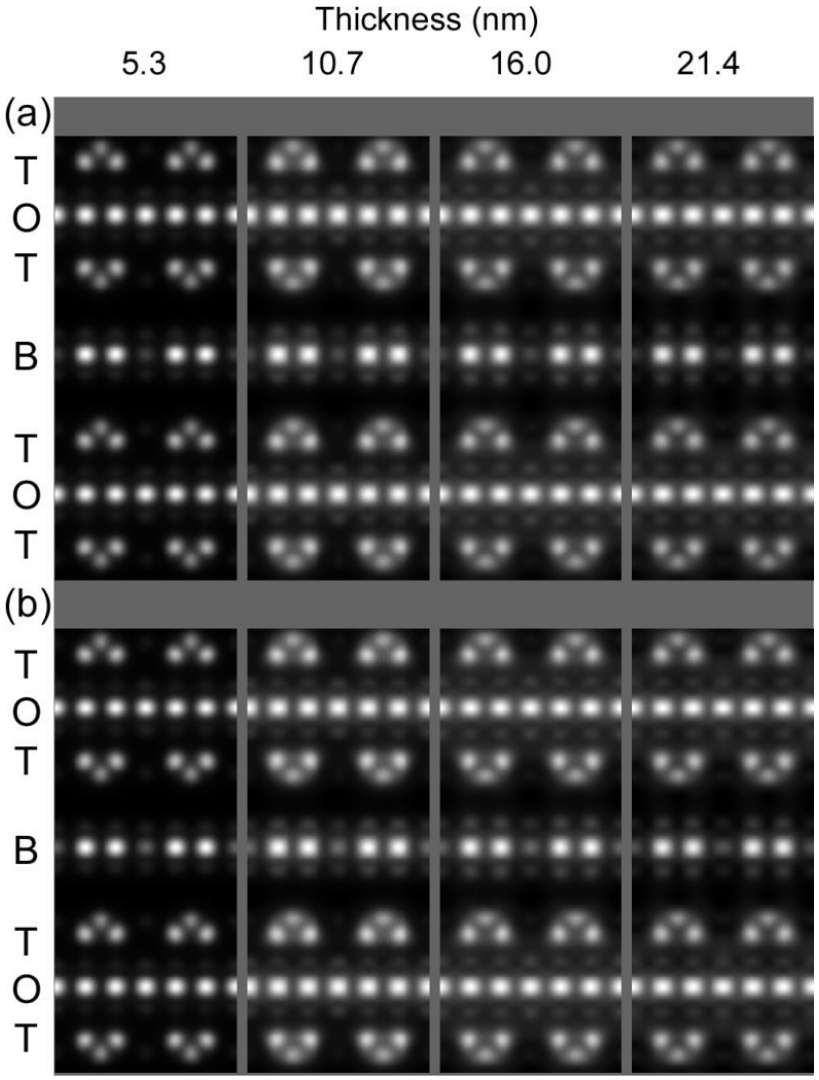

Figure IV-5. Simulated Cs-corrected HAADF-STEM images of chlorite ($(Fe^{2+}_{4.08}Fe^{3+}_{0.22}Al_{1.5}\square_{0.2})(Si_{2.5}Al_{1.5})O_{10}(OH)_8$) of octahedral cation distribution types (a) and (b) as a function of sample thickness. See text for details.

IV. 3. 2 Distribution of octahedral Fe and Al in 7Å layer

Figure IV-6 shows low magnification Cs-uncorrected HAADF images of 7Å-14Å interstratified minerals in the Ashio sample and the Soya sample (Figure IV-6). In terms of the octahedral cation distribution in the 7Å component layers of the interstratified

minerals, two types of 7Å layers are recognized in the Cs-uncorrected HAADF-STEM images (Figure IV-6). That is, one is the 7Å layer with octahedral sheet which appears to be nearly continuous bright line and the other is that with octahedral sheet which appears to be a bright line with interruption. To avoid confusion, the 7Å layer with the former type of the octahedral sheet is named disordered-type and that with the latter type of the octahedral sheet is named ordered-type. The disordered and ordered types of 7Å layers showed the O- and B-sheets like contrast profiles, respectively. In order to verify differences in the two types, the HAADF-STEM images of the disordered and the ordered types of 7Å layers, as being defined below, were simulated for both Cs-uncorrected and Cs-corrected HAADF-STEM (Figure IV-7). The chemical composition of 7Å component layer was assumed to be a half of that of 14Å component layer: $(Fe^{2+}_{1.63}\ Fe^{3+}_{0.22}Al_{1.07}\square_{0.08})\ (Si_{1.25}Al_{0.75})O_5(OH)_4$ for the disordered type and $(Fe^{2+}_{1.63}Al_{0.29}\square_{0.08})_{B,C}\ (Fe^{3+}_{0.22}Al_{0.78})_A(Si_{1.25}Al_{0.75})O_5(OH)_4$ for the ordered type together with ordered distribution of octahedral cations between the A, B and C sites defined by Bailey (1969) (Figure II-2a), similar to the type (b) of 14Å layers. It is known that there is no cation ordering in trioctahedral 1:1 phyllosilicates including berthierine (*e.g.* Bailey, 1966). Comparison of the simulated and the observed HAADF-STEM images confirmed that the cation distribution in the ordered type of 7Å layer is similar to that of B-sheet in 14Å layer. That is, Al and probably Fe^{3+} occupy preferentially the A sites of the octahedral sheet in 7Å layer. Differences in chemical composition between the two types of octahedral sheets in 7Å layers are not definitive yet on the basis of present HAADF-STEM experiments. The integrated intensity ratio between ordered and disordered types of 7Å layers was about 0.9 in HAADF-STEM image of Ashio (Figure

IV-6a). That between the B- and O-sheets was about 0.8 in the same image. It may imply that both types of 7Å layers have same chemical composition but different octahedral cation distribution.

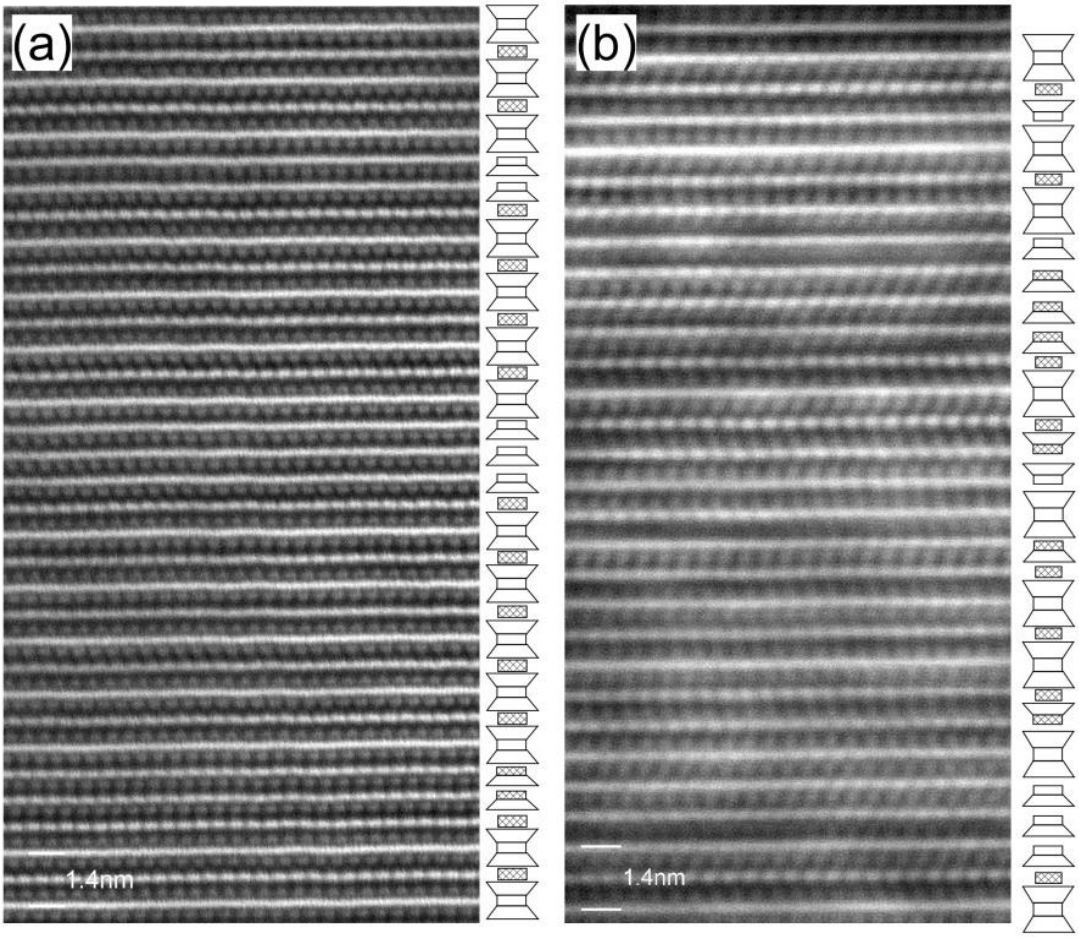

Figure IV-6. Cs-uncorrected HAADF-STEM images and schematic diagrams showing the stacking sequences of the Ashio (a) and the Soya samples (b). Trapezoids represent tetrahedral sheets. White rectangles represent O-sheet and disordered-type octahedral sheets in 7Å layer, and shaded ones represent B-sheet and ordered-type octahedral sheets in 7Å layer.

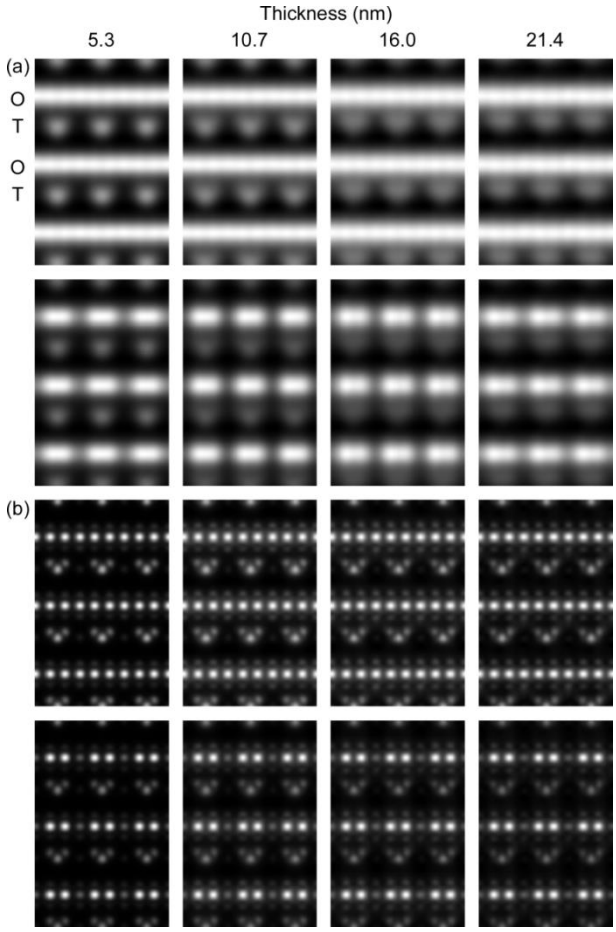

Figure IV-7. Simulated (a) Cs-uncorrected and (b) Cs-corrected HAADF-STEM images for disordered (upper) and ordered (lower) -type 7Å layers as a function of sample thickness.

IV. 3. 3. Vertical and lateral arrangements of 7Å and 14Å layers

The HRTEM observations revealed that vertical arrangement of the 7Å and 14Å layers was random, and two opposite polarities of 7Å layer existed in the arrangement. In the HAADF images (Figure IV-6), similar random distribution was observed in terms of arrangement of 7Å and 14Å layers. The 14Å layers gave a constant repetition of TOT-B in a packet locally intercalated by the two types of 7Å layers, ordered and disordered types defined above. Note that the entire arrangement of 14Å layer and two

types of 7Å layers appeared to be random and stacking of disordered and ordered types of 7Å layer with opposite polarity was visible in a packet. It is concluded that the random arrangement of 7Å and 14Å layers in Fe-rich samples is characterized by the interstratification with differences in chemistry in addition to in structure.

The 7Å-14Å interstratified minerals contained the lateral contact of opposite polar tetrahedral sheet. Figure IV-8 highlights the lateral relations between 7Å and 14Å layers in the Cs-corrected HAADF images of Ashio sample. The gaps in the octahedral sheets which are observed in the HAADF-and BF-images of Figure IV-8 may result from the noise during the image acquisition. There are two types of lateral contacts in the octahedral sheets of 7Å and 14Å layers: one is the contact between the disordered type 7Å and the B-sheet of 14Å layer (c in Figure IV-8) and the other is that between the disordered type 7Å layer and O-sheet of 14Å layer (d in Figure IV-8). It is conclusive that the stacking sequence of TOT-B is stable for Fe-rich chlorite, and both disordered and ordered types of 7Å layers exist possibly in Fe-rich berthierine, and then the 7Å layers with the ordered type octahedral sheets are always allowed to link to the O-sheet of 14Å layers in the interstratified structures. The similar structures were observed in the Soya sample.

Based on the petrographic and HRTEM observations, it was concluded that the 7Å-14Å interstratified minerals studied were not at an intermediate stage of topotactic transformation between Fe-rich berthierine and chlorite, as described previously. Although HAADF-STEM observations of the transformation type interstratified mineral have not been performed, the regular alternation of disordered and ordered type 7Å layers and the lateral contact of the ordered type 7Å layer and B-sheet is expected in this type of 7Å-14Å interstratified minerals. The lateral contact between the ordered type 7Å

layer and the B-sheet was never observed in the present study. Vertical and lateral arrangements of 7Å and 14Å layers observed by HAADF-STEM reinforce the conclusion that the samples were precipitated as a metastable phase from solution at relatively high temperatures condition.

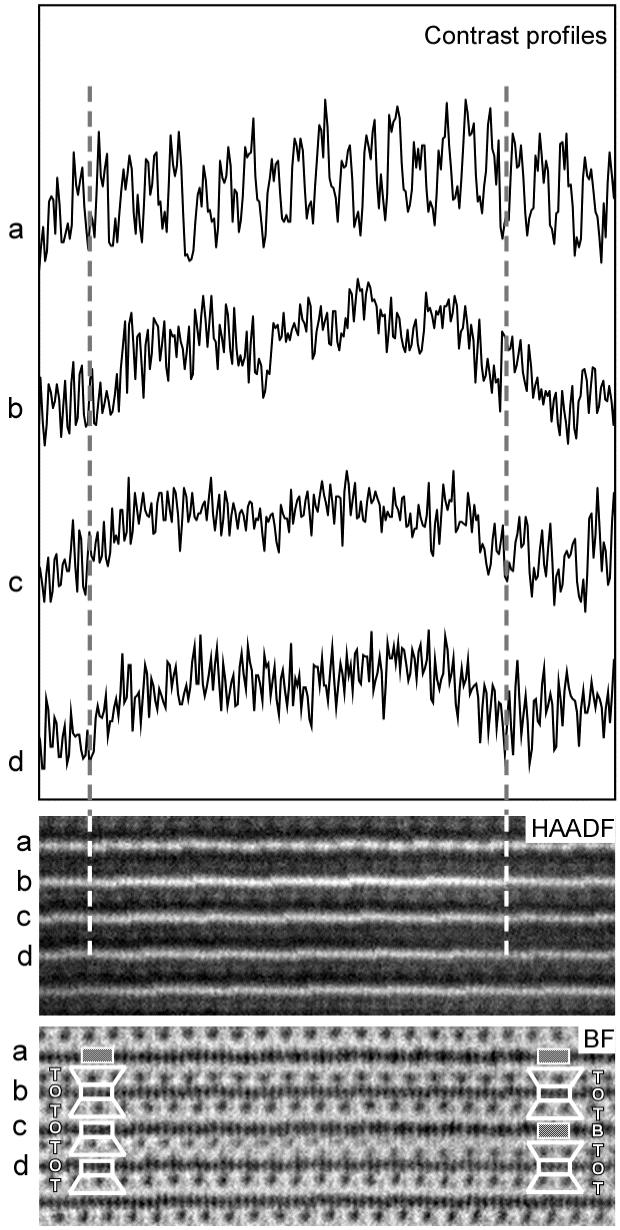

Figure IV-8. Magnified Cs-corrected HAADF-and bright field (BF) -STEM images of the lateral contacts of octahedral sheet with different cation distribution type in the Ashio sample. Contrast profiles (a-d) were measured at the octahedral sheet marked a-d in the images. a: B-sheet, b: O-sheet, c: the contact of disordered octahedral sheet of 7Å layer and B-sheet, d: the contact of disordered octahedral sheet of 7Å layer and O-sheet.

IV. 4. CONCLUSIONS

A combined HRTEM and HAADF-STEM study of 7Å-14Å interstratified minerals revealed that samples with Fe/(Fe+Mg)>0.9 were characterized by a complex mixture of component layers having different polarities, slants of the octahedral sheet and octahedral cation distributions. Particularly, 7Å layers with two types of octahedral cation distribution model, disordered and ordered types, coexisted in the samples. At the lateral contact of tetrahedral sheets with opposite polarity, types of octahedral cation distribution were frequently varied. Such structural and chemical irregularities, again, were brought about by the reason why they were precipitated as a metastable phase from solution at relatively high temperature conditions.

The regular alternation of the disordered and ordered type 7Å and the lateral contact of the ordered type 7Å layer and B-sheet may be expected for the interstratified minerals which are at an intermediate stage of the topotactic transformation from other occurrences. This hypothesis will be verified by the HAADF-STEM observations of the transformation type interstratified minerals.

Chapter V HRTEM STUDY OF PORE-LINING FE-RICH 7Å-14Å INTERSTRATIFIED MINERALS OF DIAGENETIC ORIGIN

V. 1. INTRODUCTION

V. 1. 1.Chapter introduction

The crystallochemical features of the so-called Fe-rich chlorite from hydrothermal deposits were characterized in the previous chapters (Chapters III and IV). The characteristic features were complex structural irregularities associated with layer-polarity and interlayering as well as chemical heterogeneities, which may be entirely owing to the dynamics and mechanism of the crystal growth during the rapid precipitation of the samples in solutions. Then some questions arise: whether such structural and chemical peculiarities are unique in hydrothermal chlorites or not. It is known that Fe-rich chlorites commonly occur as pore-linings in sandstones suffered from burial diagenesis, and the chlorites are considered to be mostly transformation products from precursor berthierine or odinite formed at shallower depths (*e.g.* Hillier, 1994; Billault *et al.*, 2003). It is thus important to compare the two groups of Fe-rich chlorites from different origins at atomic scale in order to understand the detail mechanism of formation.

The chemistry, morphology and structure of Fe-rich pore-lining chlorites and 7Å-14Å interstratified minerals of diagenetic origin were investigated using SEM, TEM and XRD (*e.g.* Hillier and Velde, 1992; Reynolds, *et al.*, 1992; Hillier, 1994; Billault, *et al.*, 2003). To author's knowledge, however, there are no HRTEM data available on this type of 7Å-14Å interstratified minerals which are comparable with those of the hydrothermal samples. This chapter is devoted to highlight the structural differences

between 7Å-14Å interstratified minerals of diagenetic and hydrothermal origins by HRTEM, using Fe-rich pore-lining chlorites which were already described by Hillier (1994)

V. 1. 2. Pore-lining chlorites

Chlorite commonly occurs as a mat of crystals coating framework grains in sandstones (Wilson and Pittman, 1977). Such pore-lining chlorites preserve efficiently primary intergranular porosity during subsequent deeper burial (*e.g.* Ehrenberg, 1993; Worden and Morad, 2003). This behavior of chlorite is critically important for recovering hydrocarbon because it influences the reservoir qualities such as the permeability and porosity (Ehrenberg, 1993). The occurrences of the pore-linings are generally considered to be the evidence of neoformation of minerals that precipitated from pore-water. Most of pore-lining chlorites may be transformation products of early formed minerals with progress in burial diagenesis. Both Mg-rich and Fe-rich types of pore-lining chlorites have been described to occur in siliciclastic sandstones, but Fe-rich types appears to be more common (Hillier, 1994).

V. 1. 2. 1. Mg-rich pore-lining chlorites

The occurrence of Mg-rich pore-lining chlorites is limited in deeply buried eolian sandstones that are likely to have received fluids from closely connected sabkha, playa lake or evaporite deposits during shallow burial (*e.g.* Hillier *et al.*, 1996; Biernacka, 2014). Mg-rich samples generally show a honeycomb texture, similar to the characteristics of swelling clays (E-H in Figure V-1). Mg-rich chlorite is commonly trioctahedral and often coexists with corrensite (Hillier, 1994; Hillier, *et al.*, 1996). In

some specific fields, the occurrence of sudoite, Al-rich di-trioctahedral chlorite, is reported from Rotliegend sandstones in the eastern part of the southern Permian Basin (Biernacka, 2014). Hillier (1994; 1996) pointed out that Mg-rich pore-lining chlorite is originated from Mg-smectite and eventually it is transformed via corrensite during burial diagenesis.

V. 1. 2. 2. Fe-rich pore-lining chlorites

Fe-rich pore-lining chlorites occur in near-shore marine or deltaic sediments (Ehrenberg, 1993; Worden and Morad, 2003; Beaufort *et al*., in press). Fe-rich samples show well developed euhedral crystals that are oriented perpendicular to the surfaces of framework grains and increase the grain sizes with increasing temperature (A-D in Figure V-1). Billault *et al*. (2003) noted that such morphology characterized only the crystals which occurred near the center of the pore. At the contact between quartz grains and at the base of chlorite coating, chlorites were very fine-grained and were arranged parallel to the surfaces of detritus quartz crystals.

The polytypic and interstratified structures of Fe-rich pore-lining chlorites were investigated mainly by XRD (Hillier and Velde, 1992; Reynolds, *et al.*, 1992; Hillier, 1994; Ryan and Reynolds, 1996). The previous studies indicated that samples from shallower depths usually made an interlayering of 7Å layer with 14Å layer, different from Mg-smectite, and hence Fe-rich chlorite was transformed from precursor Fe-rich 7Å minerals such as berthierine or odinite with progress in burial diagenesis. Berthierine and odinite are trioctahedral and di, trioctahedral Fe, Al-rich serpentine group minerals, respectively (Bailey, 1988d; Meunier, 2005). Hillier (1994) and Billault (2002) pointed out that the precursor 7Å mineral was more likely berthierine from the

chemical point of view, though the possibility that the precursor 7Å mineral was odinite is not excluded completely.

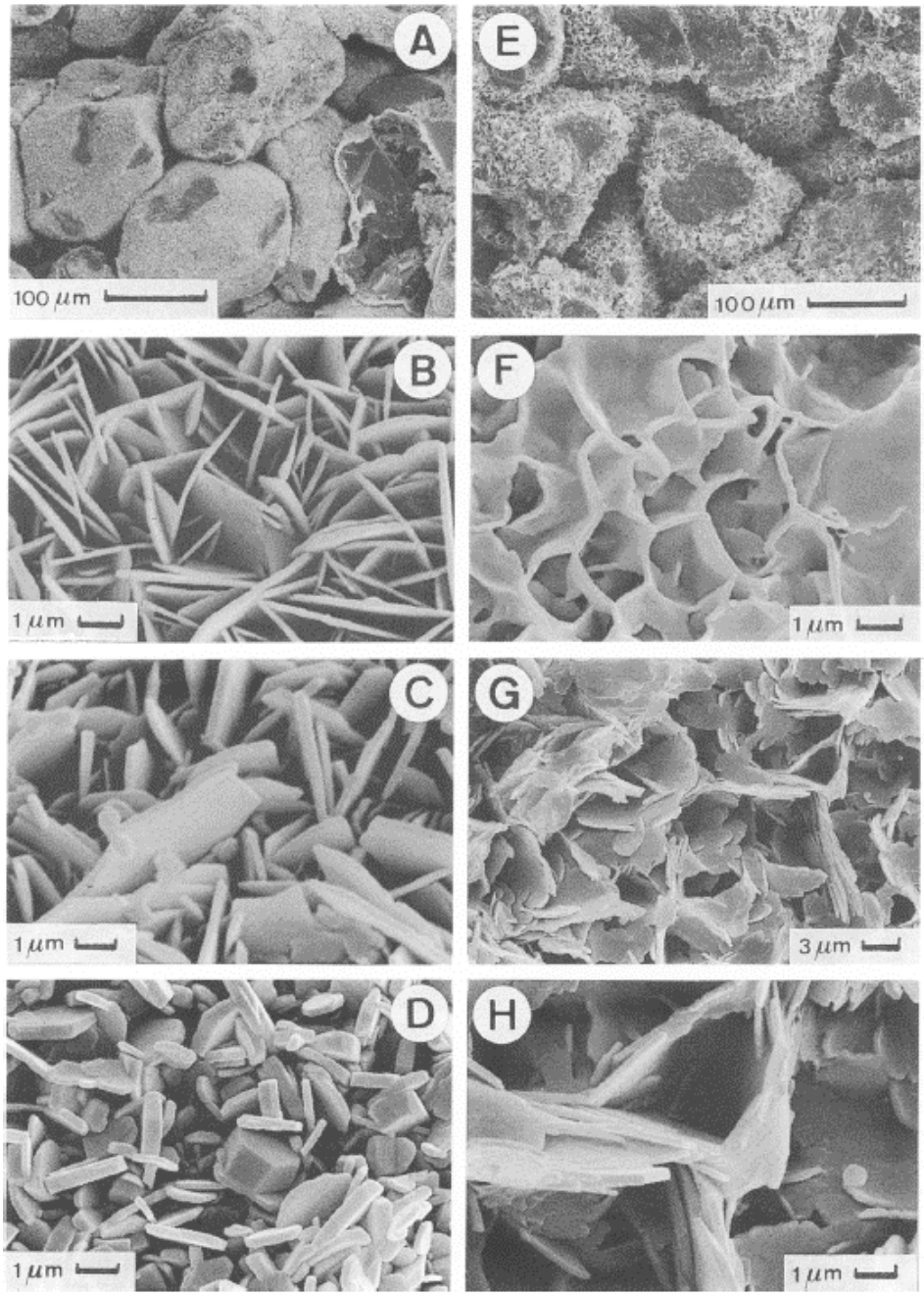

Figure V-1. SEM images of Fe-rich (A-D) and Mg-rich (E-H) pore-lining chlorites showing differences in morphology and arrangement (Hillier, 1994). A: Tilje 3, B: Dunlin 1, C: Tofte 7, D: Spiro 1, E: Rotl 66, F: Y1, corrensite, G: Rotl 6, H: Rotl 66 (close up of boxwork texture shown in G). (Hillier (1994), reprinted with the permission by the Mineralogical Society)

V. 2 SAMPLES AND METHODS

V. 2. 1. Samples

Samples studied are from the Tofte and Statfjord formations, offshore Norway, the Dogger beta Hauptsandstein, Germany and the Spiro Sandstone, Oklahoma, USA (courtesy of Prof. Stephen Hillier, the James Hutton Institute, Scotland). The details of sample descriptions can be found in Table V-1 and referred to Hillier (1994) and references therein. The chemical compositions were summarized in Table V-2, which were cited from Hillier (1994). The maximum temperatures of formation were determined by Hillier (1994) using vitrinite reflectance (Hillier and Marshall, 1992). Similar temperature data of chlorite formation were also estimated in the present study using a chlorite geothermometer of Bourdelle, *et al.* (2013) (Table V-3). Vitrinite reflectance, a measure of the thermal maturation of sedimentary organic matter, is a function of the maximum temperature reached in the system during burial diagenesis (Barker and Pawlewicz, 1986). The relation between temperature (T) and vitrinite reflectance (Ro) is expressed as $\ln(R\text{o}) = 0.0096 \cdot T - 1.4$ (Barker and Pawlewicz, 1986; Hillier and Marshall, 1992). The formation temperatures estimated by chlorite geothermometer were similar to the maximum temperatures determined using vitrinite reflectance, except for Statfjord 4 in which the maximum temperature was significantly higher than that by chlorite geothermometer (Table V-3). It is evident that the chlorite samples were formed at temperatures in a range of 100-220 ºC.

Table V-1. Details of Fe-rich pore-lining chlorites examined in this study (modified from Hillier, 1994)

Sample	Stratigraphy	Age	Location	Depositional environment	References
Haupts 1	Dogger beta Haupsandstein	M. Jurassic Bathonian	Schleswig-Holstein, Germany	Braid delta, merging with foreshore and shoreface deposits	Horn (1965), Zimmerle (1963)
Tofte 7	Tofte Formation	Toarcian	Haltenbanken, offshore Norway	Shallow marine, deltaic	Eherenberg (1991; 1993)
Stat 4	Statfjord Formation	Rhaetian-Sinemurian	Veselefrikk Field, offshore Norway	Shallow marine middle to upper shore face	Eherenberg (1991; 1993)
Spiro 3	Spiro Sandstone	Pennsylvanian	Arkoma Basin,Oklahoma and Arkanasas	Variety marine and non marine fluvial and tidal channels	Lumsden et al. (1971), Houseknecht (1987)

Table V-2. Structural formulae were calculated on the basis of O=14.

	Spiro3	Tofte7	Statfjord4	Haupts1
SiO_2	22.11	19.89	17.51	18.76
TiO_2	0.04	0.03	0.04	0.08
Al_2O_3	21.39	16.66	14.92	15.78
FeO*	31.53	24.47	21.31	20.57
MgO	4.92	4.55	3.56	2.86
MnO	0.13	0.03	0.04	0.02
CaO	0.03	0.11	0.08	0.05
Na_2O	0.06	0.04	0.18	0.18
K_2O	0.08	0.12	0.07	0.27
	80.29	65.90	57.71	58.57
	Structural formula on the basis of O=14			
Si	2.68	2.89	2.90	3.03
Al(IV)	1.33	1.12	1.10	0.98
ΣTetrahedral cations	4.00	4.00	4.00	4.00
Al(VI)	1.72	1.74	1.81	2.02
Fe	3.19	2.97	2.95	2.77
Mg	0.89	0.99	0.88	0.69
Mn	0.02	0.01	0.01	0.01
ΣOctahedral cations	5.81	5.69	5.65	5.48
No. of vacancies	0.20	0.31	0.36	0.52
Fe/(Fe+Mg)	0.78	0.75	0.77	0.80

* Total iron as FeO

Table V-3. Fe/(Fe+Mg), estimated maximum temperature and formation temperature, the proportion of 7Å layers determined by XRD and TEM.

				XRD				TEM	
Sample	Fe/(Fe+Mg)	Tvr (°C)*	Tcg (°C)	%7Å (1)*	%7Å (2)*	%7Å (2)	Polytype	%7Å	Polytype
Spiro 3	0.78	220	220	0	1	1	I*bb*, II*bb*	3	I*bb*
Tofte 7	0.75	155	151	11	7	6	I*bb*	7	I*bb* (+I*ba*)
Statfjord 4	0.77	125	141	25	15	>20	I*bb*	54	I*bb*
Haupts1	0.8	100	105	26	22	>20	I*bb*	44	I*bb* (+I*ba*)

* Data cited from Hillier (1994)
Tvr: Maximum temperature determined based on vitrinite reflectance
Tcg: Formation temperature estimated using the chlorite geothermomter by Bourdelle et al. (2013)
(1) Method of Hillier and Velde (1992)
(2) Method of Reynolds et al. (1992)

V. 2. 2. Methods

Powder samples of chlorites were impregnated in an epoxy resin and sandwiched between two glass slides so that the (001) plane of chlorite were oriented. The slab of chlorite grains were sliced perpendicular to the (001) plane with a diamond wheel cutter and polished mechanically to ~ 1 μm thick. The thin section was sandwiched between copper TEM grids, and thinned to electron transparency by Ar^+ ion milling (Gatan Model 600 Dual Ion Mill). TEM specimens were lightly coated with carbon to prevent charge accumulation and observed in TEM (JEOL JEM-2010UHR) operated at 200 kV. Powder XRD patterns were obtained following the methods described in Chapter III.

V. 3. RESULTS AND DISCUSSION

V. 3. 1. Characteristics of chemical compositions

All of the samples of interest have a narrow range of Fe/(Fe+Mg) values between 0.7 and 0.8. The tetrahedral Al contents are in the range of 0.98-1.12 apfu, which are almost equivalent to those (0.94-1.44 apfu) of hydrothermal samples studied in the previous

chapters (Table III-1). The total R^{3+} contents of samples excluding Fe^{3+} are invariable within a range of 2.86-3.00, whereas the numbers of vacancies vary significantly within a range of 0.20-0.52. These chemical characteristics are illustrated in the Wiewióra-Weiss' diagram of Figure V-2 (Wiewióra and Weiss, 1990), following Bourdelle and Cathelineau (2015). For instance, the number of vacancies and the total Al (R^{3+}) content of the Spiro3 with a formation temperature >200 °C are 0.2 and 3.05 respectively, whereas those of sample Haupts1 with the lowest formation temperature of 100 °C are 0.52 and 3.0 respectively. The compositions appear to be entirely in parallel with the $Si + \square \leftrightarrow 2R^{2+}$ exchange vector.

The chemical compositions of the studied samples are compared with those of Fe-rich chlorites, 7Å-14Å interstratified minerals and berthierines that show pore-lining occurrences (*e.g.* Curtis *et al*., 1982; Ahn and Peacor, 1985; Ryan and Reynolds, 1992; Hornibrook and Longstaffe, 1996; Billault *et al*., 2003), in addition to odinite (Bailey 1988d) and berthierine (Brindley, 1982). In the Wiewióra-Weiss' diagram (Figure V-3), all compositions were calculated on the basis of O=14 and all iron cations were regarded as divalent. The present pore-lining chlorite and 7Å-14Å interstratified samples are characterized by low total octahedral cation contents owing to the large numbers of vacancies. Surprisingly, they are plotted in a range between the chemical compositions of berthierine and odinite (see Figure V-3), rather than being plotted along the typical berthierine compositions described by Brindley (1982). Similar characteristics were recognized for other pore-lining berthierines (*e.g.* Hornibrook and Longstaffe, 1996; Curtis, 1985). Hornibrook and Longstaffe (1996) indicated that the trend in chemical composition of their pore-lining berthierine showed the presence of odinite-berthierine solid solution series. Accordingly, the compositional trend of the

present pore-lining Fe-rich chlorites suggests that they preserve a trace of odinite in the structures to some extent.

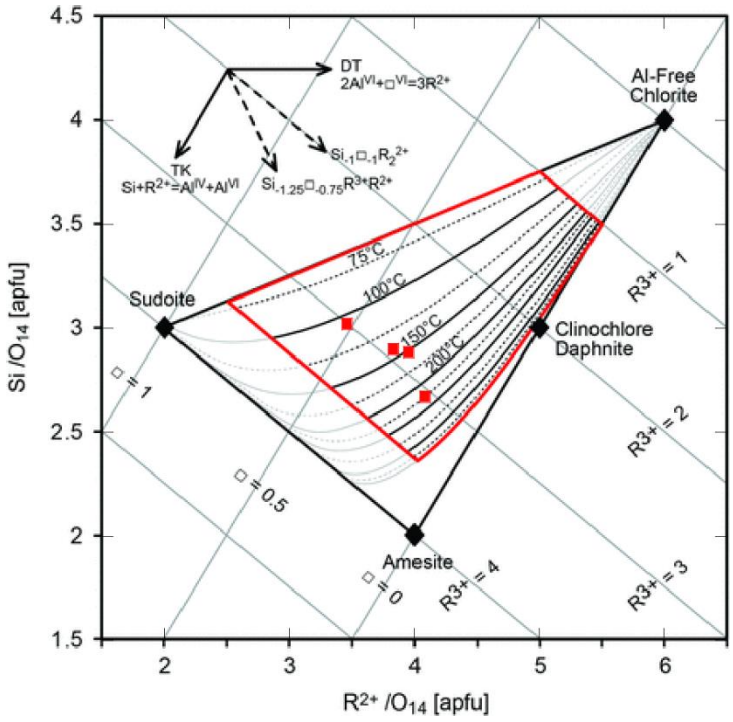

Figure V- 2. R^{2+}-Si plot of Wiewiora and Weiss (1990) of pore-lining samples overlaid on the representation of isotherms calculated with Bourdelle et al. (2013)'s geothermometer. The area shown in red suggested the area of optimal reliability for the geothermometer. Modified from Bourdelle and Cathelineau (2015) with permission from the Schweizerbart and Borntraeger science publishers (www.schweizerbart.de).

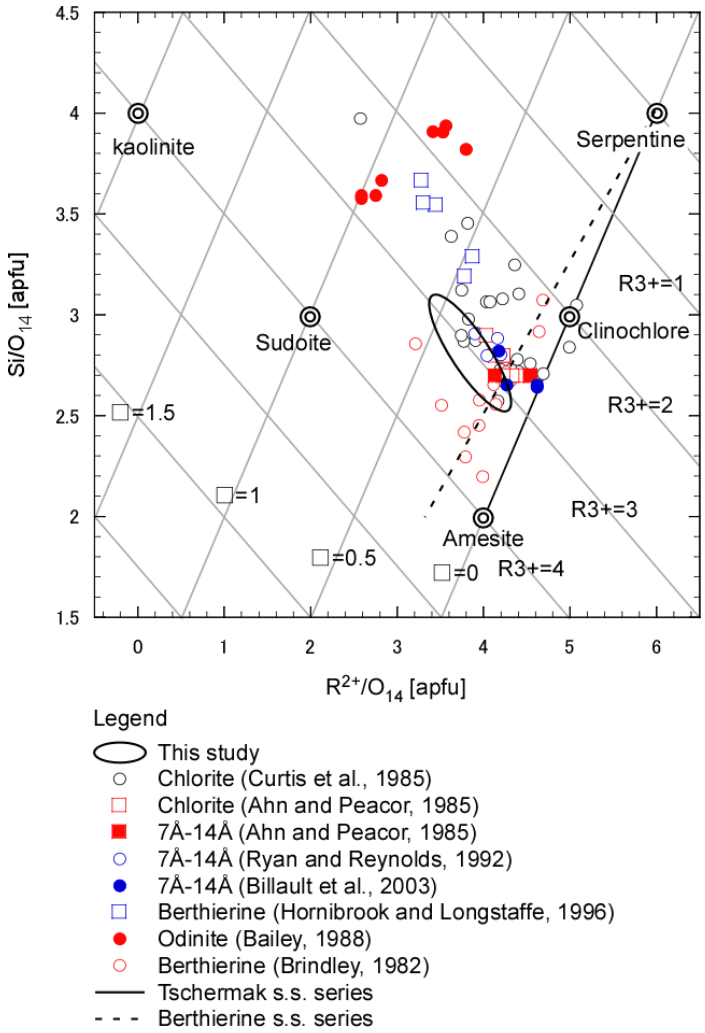

Figure V-3. Wiewióra-Weiss' diagram of pore-linings of this study and of previous studies. The chemical compositions of berthierine (Brindley, 1982) and odinite (Bailey, 1988d) are also plotted in the diagram. All of the compositions are calculated on the basis of O= 14 and iron cations are regarded as divalent.

V. 3. 2. XRD

The samples contained impurities such as quartz, illite and possibly illite-smectite interstratified mineral (Figure V-4). The 14Å reflection of chlorite was present in all XRD patterns. The presence of corrensite was not recognized in the studied samples. Any large d-spacing reflection which is diagnostic of regular interstratification between 7Å and 14Å layers like dozyite was not observed in all samples. The broadening of odd-order 00*l* reflections of chlorite diagnostic of random 7Å-14Å interstratification was apparent in all samples compared to hydrothermal chlorites described in the previous chapters.

Reynolds *et al*. (1992) proposed a quantification method to estimate the proportion of 7Å layers in random 7Å-14Å interstratified minerals using the difference between the full width at half maximum (FWHM) values of 004 and 005 reflections. Residual line broadening (βr) is obtained from FWHM of diffraction profile for the 004 (β_{004}) and 005 (β_{005}) reflections by the following equation: $\beta_r = \left(\beta_{005}^{1.25} - \beta_{004}^{1.25}\right)^{\frac{1}{1.25}}$. The proportion of 7Å layers (%7Å) in the random interstratification is calculated from the empirical expression: %7Å = -0.51 + 24.27βr. This expression is valid in the range from about 1 to 20 % of the %7Å (Reynolds *et al*., 1992). Hillier and Velde (1992) also proposed a modified method to quantify the proportion of 7Å layers in the interstratified mineral. The proportion values determined by the two methods are given in Table V-3.

The %7Å values in the 7Å-14Å interstratified mineral were 1 % for Spiro3 and 6 % for Tofte7. The proportions for the Statfjord4 and Hautps1 samples were >20%. It is obvious that the proportion of 7Å layers decreases with increasing the formation temperature, and it also decreases with the amount of vacancies although it is independent of the Fe/(Fe+Mg) ratio.

XRD profiles of samples in the range of 30-75 in °2θ showed that the polytypes of samples are assigned into I*bb*, except for Spiro 3 in which the polytype is a mixture of I*bb* and II*bb* (Figure V-5), based on the notation of Shirozu and Bailey (1965). The results of XRD are consistent with the results of Hillier (1994).

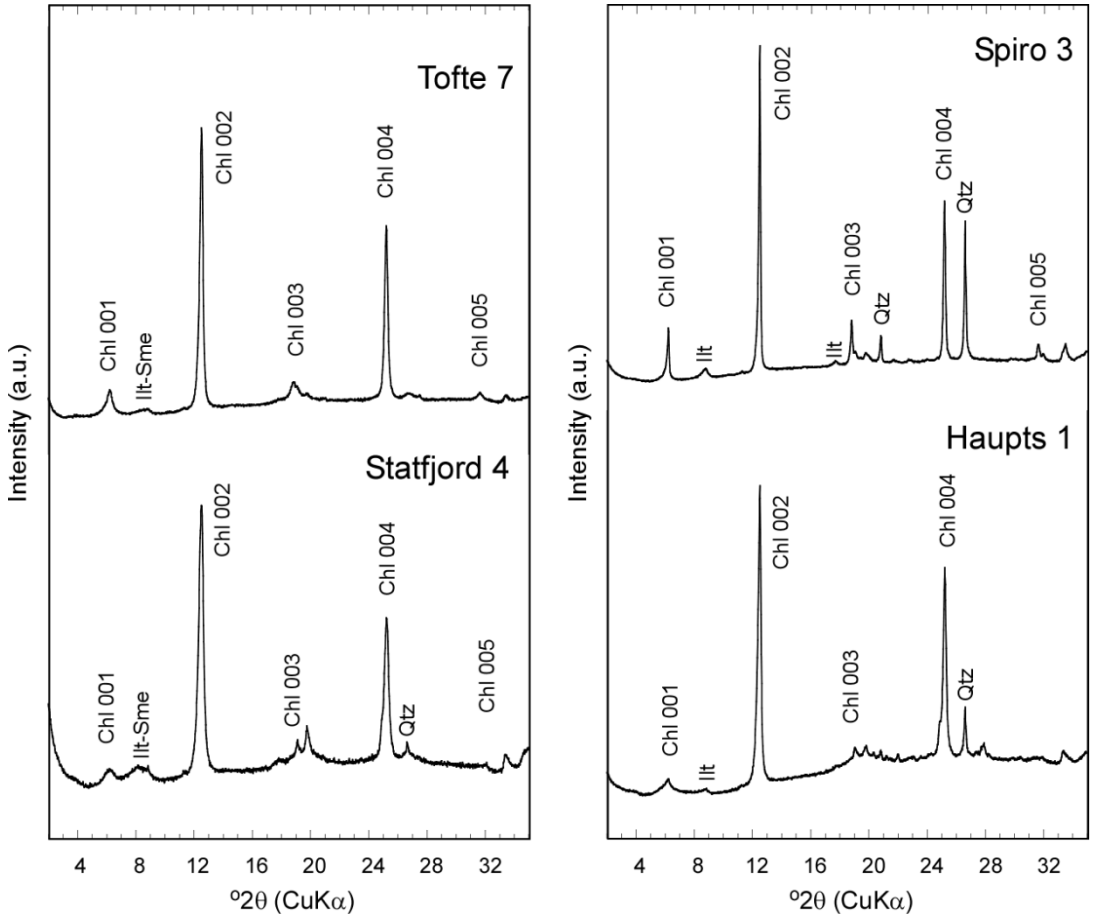

Figure V-4. XRD patterns of samples in a range of 2-35 º. Chl: chlorite, Qtz: quartz, Ilt-Sme: Illite-smectite mixed-layer mineral, Ilt: illite

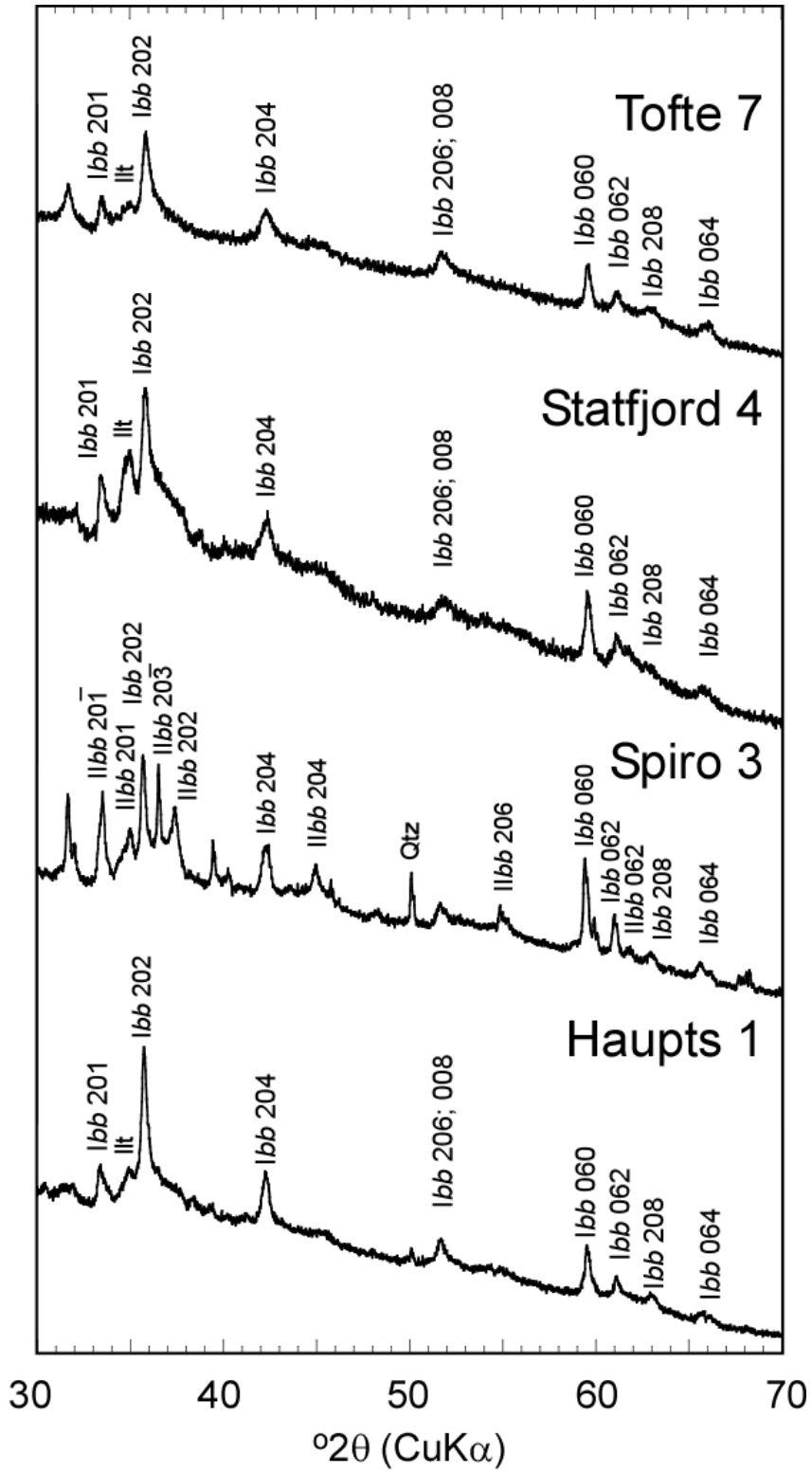

Figure V-5. XRD patterns of samples in a range of 30-70 º showing the polytypic groups.

V. 3. 3. HRTEM

Selected low magnification HRTEM images are given in Figure V-6. Most samples were characterized by continuous, parallel stacks of layers without any dislocations. All samples displayed interlayering of 14Å layers with 7Å layers (Figure V-6) without systematic repetition of 7Å and 14Å layers.

The %7Å were determined from the HRTEM images, similar to the previous procedures for hydrothermal chlorites (Chapter III), 3 % for Spiro 3, 7 % for Tofte 7, 44 % for Haupts 1 and 54 % for Statfjord 4, respectively (Table V-3). The differences in the %7Å values between XRD and HRTEM may be attributed to certain statistic problem in observed grains. Nevertheless, the %7Å is strongly linked to the estimated temperatures of chlorite formation rather than the Fe/(Fe+Mg), the fact which is almost consistent with the results of XRD.

SAED patterns of the samples along one of the Y_i directions showed the decrease in the intensities of odd 00*l* spots for chlorite with increasing the %7Å (Figure V-7). Considering the reciprocal lattices in the SAED patterns, both Tofte7 and Spiro3 have a type I structure of Shirozu and Bailey (1965) (Figure V-7). The other SAED patterns showed the streaking along the c* direction, and hence the assignments of polytypic group from these SAED patterns were impossible.

In the high magnification HRTEM images, all the samples indicated that the stacking structure of 14Å layers is expressed as a mixture of I*bb* and I*ba*, and that of 7Å layers is expressed as group C using the polytypic notation methods of chlorite (Shirozu and Bailey, 1965) and 1:1 phyllosilicate (Bailey, 1969), respectively. On the other hand, using the new notation method proposed in this study (Chapter III), the stacking

structures are denoted by mixtures of I*b* and I*a* modules (Figures V-8 and 9). The number of I*b* modules predominated over that of I*a* structure modules in all the samples. All the intercalated 7Å layers presented in the HRTEM images of Spiro3 and Statfjord4 are described by +c modules (see Chapter III). In the HRTEM images of Haupts1 and Tofte7, both +c and –c 7-Å layers are intercalated. The occurrence of opposite polar 7Å layers appeared to be rare.

Hillier (1994) suggested, as mentioned above, that the 7Å-14Å interstratified minerals with the aforementioned structural characteristic were intermediate products of transformation from berthierine (or odinite) to chlorite. Regarding the transformation mechanism, Xu and Veblen (1996) and Banfield *et al*. (1996) observed the lateral contacts of opposite polar tetrahedral sheets which are similar to the structure shown in Figure III-10. They discussed the transformation mechanism from serpentine mineral to chlorite in detail on the basis of the lateral relationship. However, no lateral contact of the opposite polar 7Å layers was observed in the HRTEM images of studied pore-lining samples. Therefore we cannot discuss the detail mechanism of transformation from berthierine (or odinite) to chlorite at present.

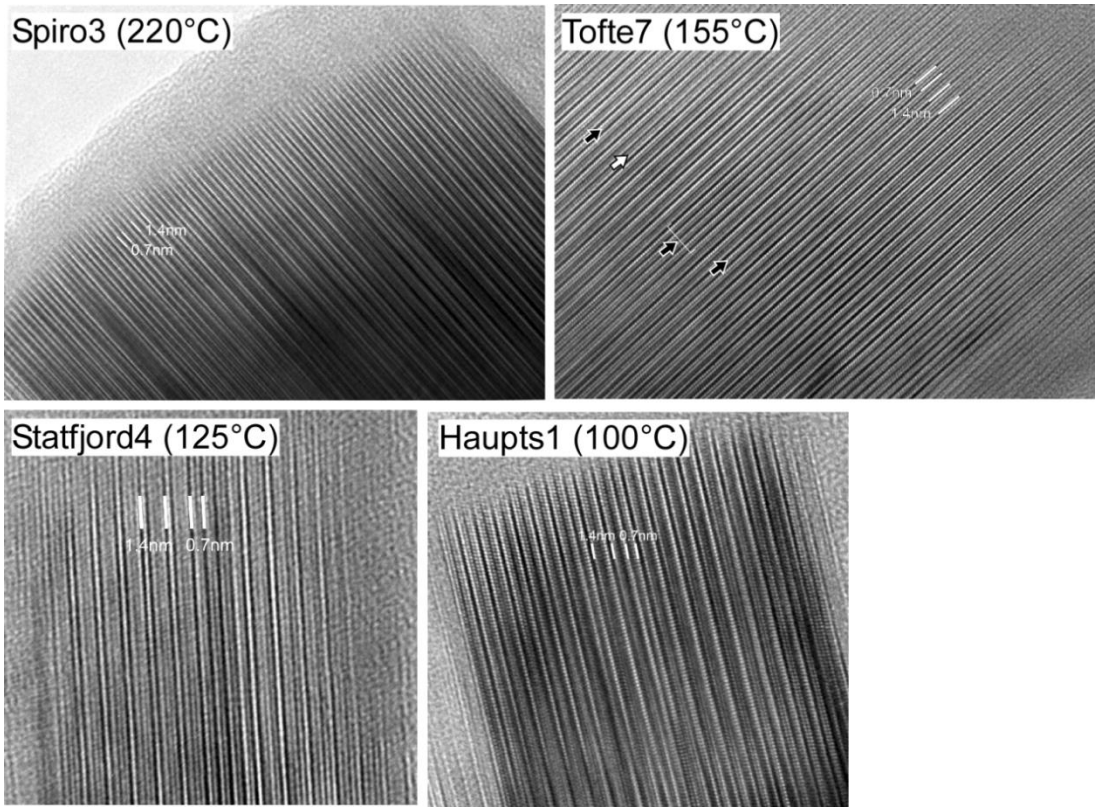

Figure V-6. Low magnification HRTEM images of samples. All images were recorded along one of the Y*i* directions. The arrows in the HRTEM image of Tofte7 indicate the 7Å layers. White arrow indicates the 7Å layer with the polarity opposite to the 7Å layers indicate by the black arrows.

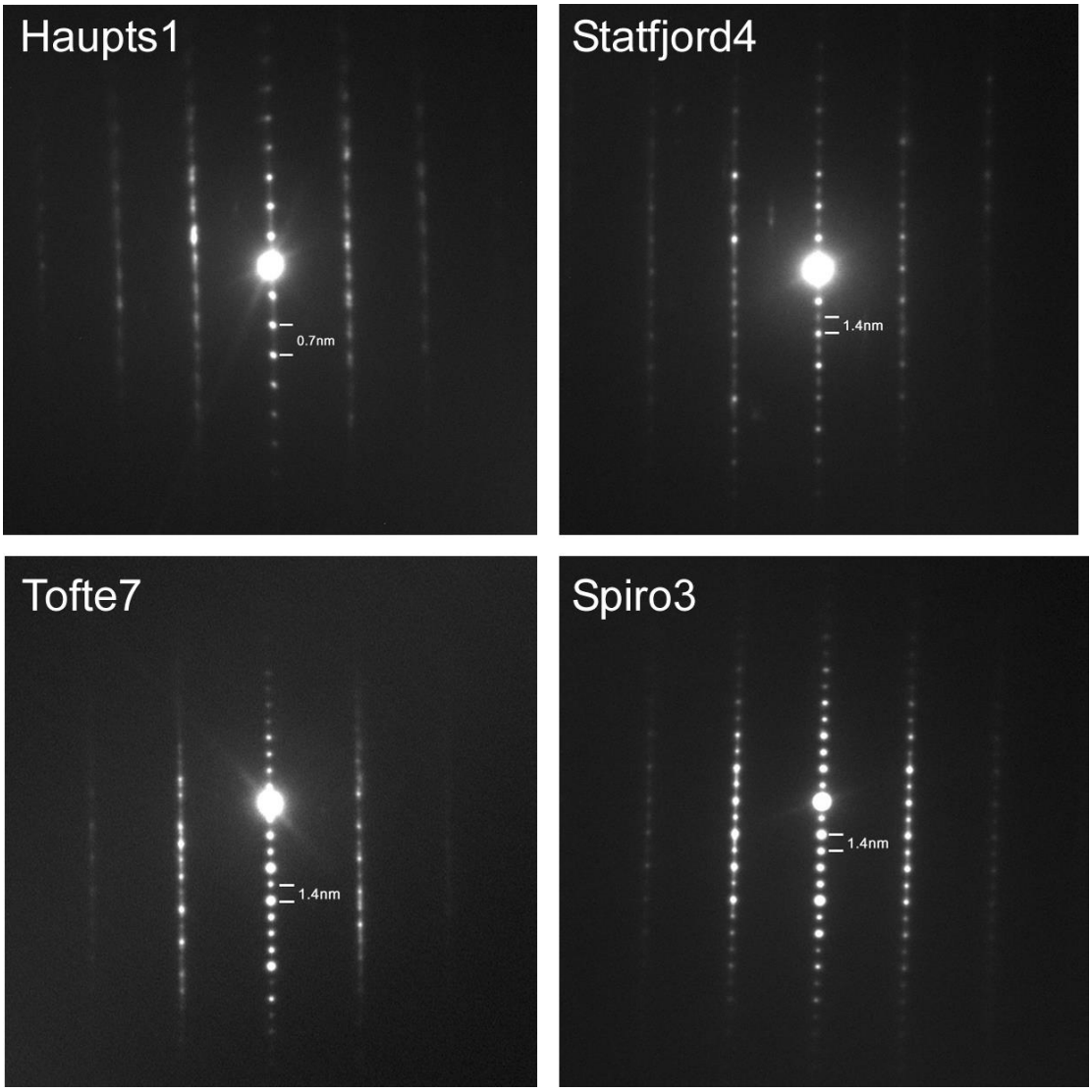

Figure V-7. Examples of SAED patterns of samples recorded along one of the Y*i* directions.

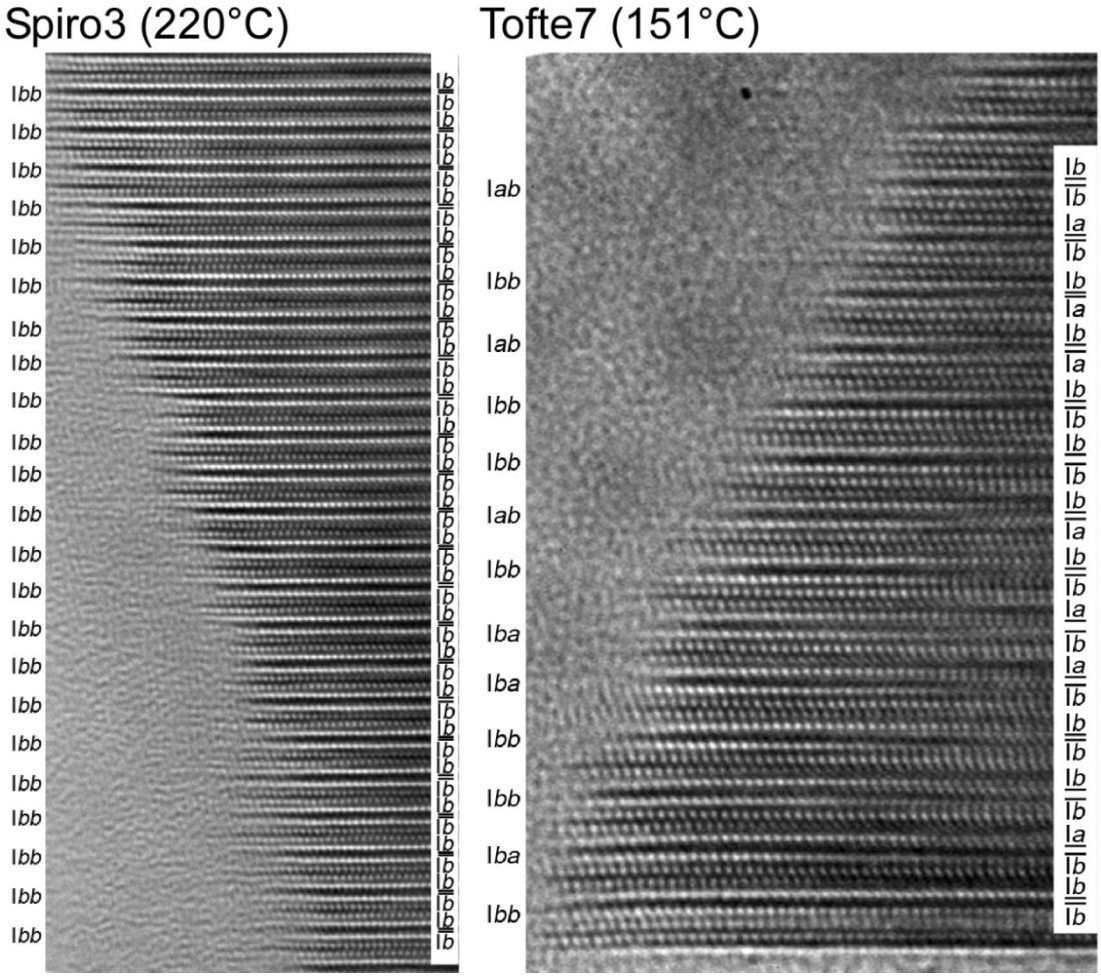

Figure V-6. HRTEM images recorded along one of the Y*i* directions of Spiro3 and Tofte7. The polytypic notations of Bailey (1988) and Bailey (1969) are described at the left-hand side of the images. The symbols for the notation method proposed in Chapter III are denoted at the right-hand side of the images.

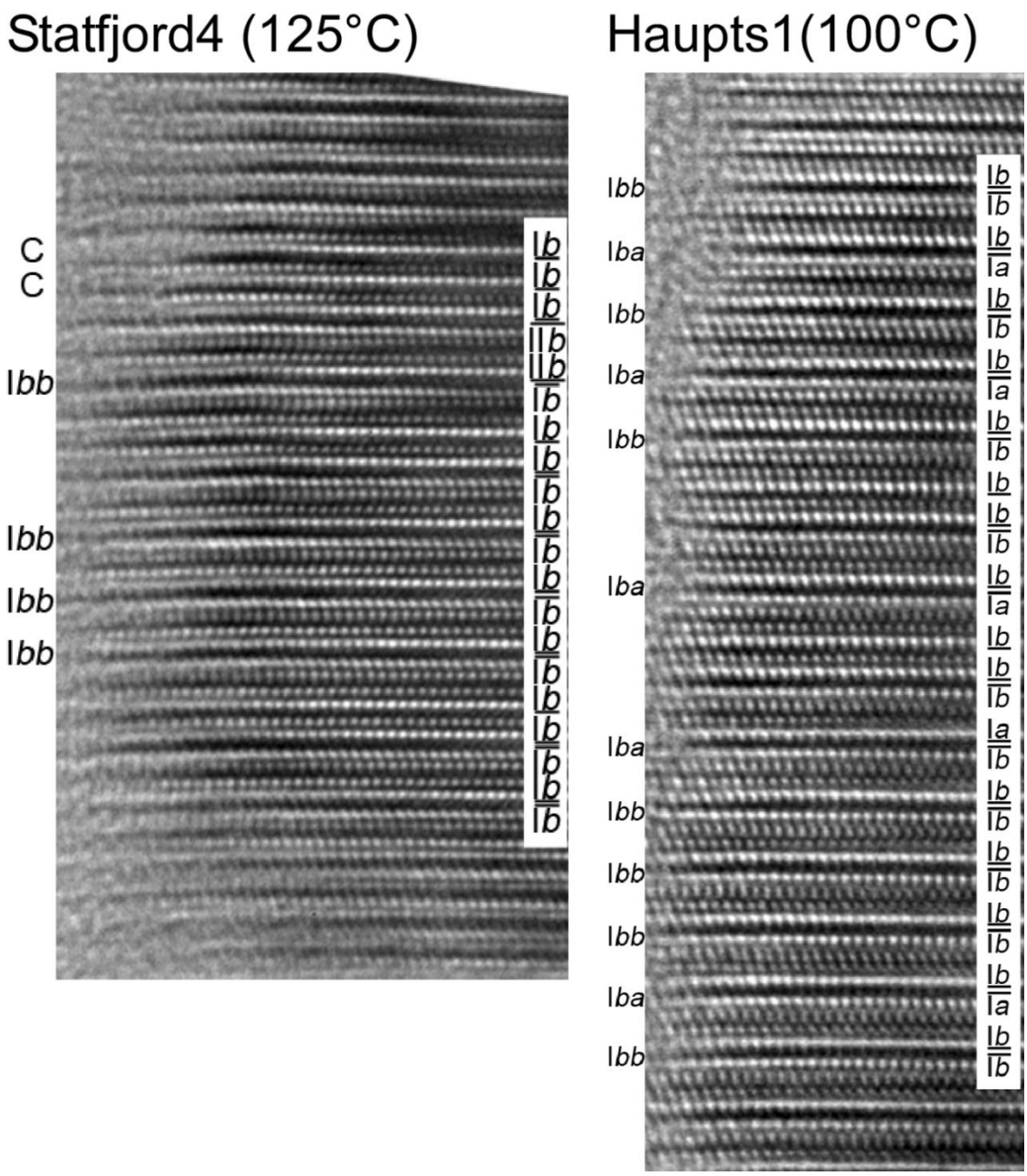

Figure V-7. HRTEM images recorded along one of the Y*i* directions of Statfjord4 and Haupts1. The polytypic notations of Bailey (1988) and Bailey (1969) are described at the left-hand side of the images. The symbols for the notation method proposed in Chapter III are denoted at the right-hand side of the images.

V. 4. SUMMARY AND CONCLUSIONS

Pore-lining 7Å-14Å interstratified minerals were newly characterized by HRTEM and XRD in the present study. The formation temperatures of these samples ranged between 100 ºC and 220 ºC. The samples had Fe/(Fe+Mg) values between 0.7 and 0.8. The pore-lining chlorite and 7Å-14Å interstratified samples are characterized by low total octahedral cation contents owing to a large number of vacancies so that the chemical compositions extend in the range between those of odinite and berthierine in Wiewióra-Weiss' diagram (Figure V-3). Similar characteristics are recognized for other pore-lining berthierines. Accordingly, the pore-lining Fe-rich chlorites preserve a trace of odinite in the structures from the chemical points of view.

XRD and low magnification HRTEM suggested that the proportion of 7Å layers in the interstratified minerals decreased with increasing the temperature of formation. A mixture of opposite polar 7Å layers was very locally observed in the high magnification HRTEM images of the samples.

Hillier (1994) suggested that the studied samples are intermediate products of transformation from berthierine (or odinite) to chlorite. From the chemical point of view, the possibility that the 7Å precursor of pore-lining chlorite was odinite cannot be excluded. However, no lateral contact of opposite polar tetrahedral sheets was observed. Therefore we cannot discuss the detail mechanism of transformation from berthierine (or odinite) to chlorite at present, and the transformation mechanism is still open for the discussion.

VI. GENERAL DISCUSSION AND CONCLUSION

VI. 1. SUMMARY OF RESULTS

The following results were obtained through this study: Fe-rich chlorites of hydrothermal origin were not a pure phase of 14Å chlorite but always intercalated with other layers such as 7Å or 10Å phases. Petrographic and microscopic observations indicated that they were products of direct precipitation from solution under temperatures >200 ℃ that were estimated by chemical geothermometer and microthermometry. Their structures were unlikely to be modified by subsequent events from the mode of occurrence.

In more detail, the samples with Fe/(Fe+Mg)>0.6 contained more or less interlayering of 7Å layers on HRTEM images regardless of the formation temperatures, and especially those with Fe/(Fe+Mg)>0.8 were 7Å layer predominant. It is thereby concluded that the change in the proportion of 7Å layers in the interstratified minerals of hydrothermal origin was a function of the Fe/(Fe+Mg), but not the formation temperature. More striking feature was that hydrothermal 7Å-14Å interstratified minerals with Fe/(Fe+Mg)>0.8 was characterized by disordered arrangement of 7Å and 14Å layers, differences in the polarity of the tetrahedral sheets and a mixture of different polytypic structures. In addition, the lateral contact of tetrahedral sheets with opposite polarity was frequently observed in HRTEM images.

HAADF-STEM observations of the samples with Fe/(Fe+Mg)>0.9 suggested that the O-sheet and the B-sheet of 14Å component layers had different octahedral cation distributions in which octahedral Al and Fe^{3+} are concentrated in the M4 sites of the B-sheet. The 7Å component layers with two types of octahedral cation distributions,

named disordered- and ordered-types, were recognized in the HAADF-STEM images. The disordered type 7Å layer has octahedral cation distribution like that of the octahedral sheet in the 2:1 layer. On the other hand, the ordered-type 7Å layer has octahedral cation distribution that resembles that of the B-sheet. Vertical and lateral arrangements of 14Å layers and disordered and ordered types of 7Å layers are random in the HAADF-STEM images.

Pore-lining Fe-rich chlorites of diagenetic origins studied here for the sake of comparison were characterized by the formation temperatures ranged 100-200 °C and the Fe/(Fe+Mg) ranged 0.7-0.8, in addition to similar Al (VI) contents to those of hydrothermal origin. They were initially precipitated as berthierine or odinite from solution, and the 7Å precursor minerals transformed to chlorite with increasing burial depth. The samples contained predominantly 14Å layer in the 7Å-14Å interstratified structure. The proportion of 7Å layers decreased with increasing temperature, which is different from the case of hydrothermal chlorites. The entire structure was characterized by the variations in the polytypic structure in addition to the limited presence of reversal polarities of tetrahedral sheets. No lateral contact of opposite polar tetrahedral sheets was observed in the pore-lining samples.

VI. 2. GENERAL DISCUSSION

The followings are a general discussion on the formation and transformation mechanisms of Fe-rich chlorites and 7Å-14Å interstratified minerals based on the above results. It has been generally accepted that berthierine and chlorite are of polymorphs each other, berthierine is stable at lower temperatures and transforms into chlorite at temperatures higher than 200 °C (*e.g.* Velde, 1985; Jiang *et al*., 1992; Aagaard *et al*.,

2000; Meunier, 2005). Nevertheless, the present study demonstrated that berthierine was formed at temperatures >200 °C under hydrothermal conditions and many of Fe-rich chlorites consisted of interstratified minerals with 7Å and 14Å layers. These observations give attention to the polymorphic interpretation between berthierine and Fe-chlorite. Blanc *et al*. (2014) indicated that the transformation temperature from berthierine to chlorite depends on the Fe-contents of precursor minerals.

Regarding the transformation mechanisms, if the two minerals are of polymorphs each other, a solid-state transformation mechanism may be reasonably expected, as described by the reversal of tetrahedral sheets in the 1:1 layer (Xu and Veblen, 1996; Banfield *et al*., 1996; Meunier, 2010). At a first glance, indeed, the lateral contacts of opposite polar tetrahedral sheets which observed in the hydrothermal 7Å-14Å interstratified minerals appeared to be similar to those observed by Xu and Veblen (1996) and Banfield *et al*. (1996). However, close observations by HAADF-STEM showed that the type of octahedral cation distribution frequently varied at the lateral contact. As a consequence, the solid-state transformation mechanism failed to explain the lateral relationships between the two component layers.

It is expected for pore-lining chlorite minerals of diagenetic origin that the lateral relationships between 7Å and 14Å component layers appears frequently in the process of the transformation from berthierine to chlorite. In fact, the lateral relationships between two component layers were infrequent in the present HRTEM study. In summary, the formation of the present 7Å-14Å interstratified minerals in both hydrothermal and diagenetic samples is not simply explained by the crystal growth model based on the solid-state transformation mechanism proposed previously, *i.e.* the reversal of tetrahedral sheets in the 1:1 layers.

A new working hypothesis for the formation mechanism of Fe-rich minerals is proposed as follows. Firstly it is assumed that there are three growth modules, named disordered-type, ordered-type and B-sheet (Figure VI-1), based on the present HRTEM and HAADF-STEM results. The disordered-type and ordered-type modules are expressed as the combination of a negatively charged tetrahedral sheet and a positively charged octahedral sheet so that the charges are compensated for each other. The layer charges of octahedral sheets in disordered- and ordered-type modules are $+\alpha$ and $+\beta$ respectively, where $\beta>\alpha$. B-sheet has a layer charge of $+\beta$.

In the growth of pure 14Å chlorite due to direct precipitation, three types of stacking combination of layers are expected: the B-sheet is sandwiched by (a) two disordered-type modules, (b) disordered- and ordered-type modules and (c) two ordered-type modules when the B-sheet always exists in the interlayer position. The HAADF-STEM observations indicated that the observed 14Å component layers were exclusively type (a). It is thus deduced that the sequence of type (a) stacking is most stable for pure 14Å chlorite formed at higher temperatures (probably >200 °C). Taking into consideration the amount of layer charge in each module, the stability of stacking may be reduced in the order of (b) to (c). The relationship between the present stability order and the polytypic stability accepted previously (Bailey, 1988a) is open for future study.

In 7Å berthierines precipitated, similarly, several varieties of stacking sequences can be expected. The chemical composition of berthierine is assumed to be a solid solution between virtual odinite $(R^{2+}_{1.3}R^{3+}_{1.2}\square_{0.5})(Si_{1.8}Al_{0.2})O_5(OH)_4$ and amesite $(R^{2+}_2R^{3+})(SiAl)O_5(OH)_4$. Berthierine is described as a uniform stacking of either ordered-type modules or disordered-type modules (Figure VI-1). The uniform stacking

of ordered-type (with higher layer charges) modules may be less stable than that of disordered-type modules, although this relation is not confirmed yet. The present HRTEM demonstrated the existence of stacking of opposite polar 7Å layers in which two tetrahedral sheets pointed toward the opposite directions. If this is the case, the B-sheet module has to be intercalated between the two tetrahedral sheets to form 14Å chlorite. Actually, however, because the net layer charge of 7Å layers is primarily close to neutral, intercalating a positively charged B-sheet brings about the unbalance in the net layer charge of crystal and resultantly the stacking sequence is less stable than the uniform stacking. As mentioned in Chapter IV, the lateral contact between the ordered-type octahedral sheet and the B-sheet was not observed in our samples, and hence this type of lateral contact is considered to be least stable. On the contrary, the lateral contact of disordered-type octahedral sheets may be stable.

On the assumptions mentioned above, precipitating 7Å-14Å interstratified minerals in solution are a result of accretion of the above growth modules which are freely attached to each other. This mechanism is neither the solid-state transformation of precursor minerals nor simple crystal growth model, rather, is geometrically similar to the oriented attachment growth model of the modules in solution (*e.g.* Penn and Banfield, 1998; Banfield and Zhang, 2001). Parallel and lateral accretions of several growth modules result in the formation of a variety of interstratified minerals in which the stacking structure of component layers is allowed to be completely irregular in a certain case. This model can be applied to hydrothermal samples at least.

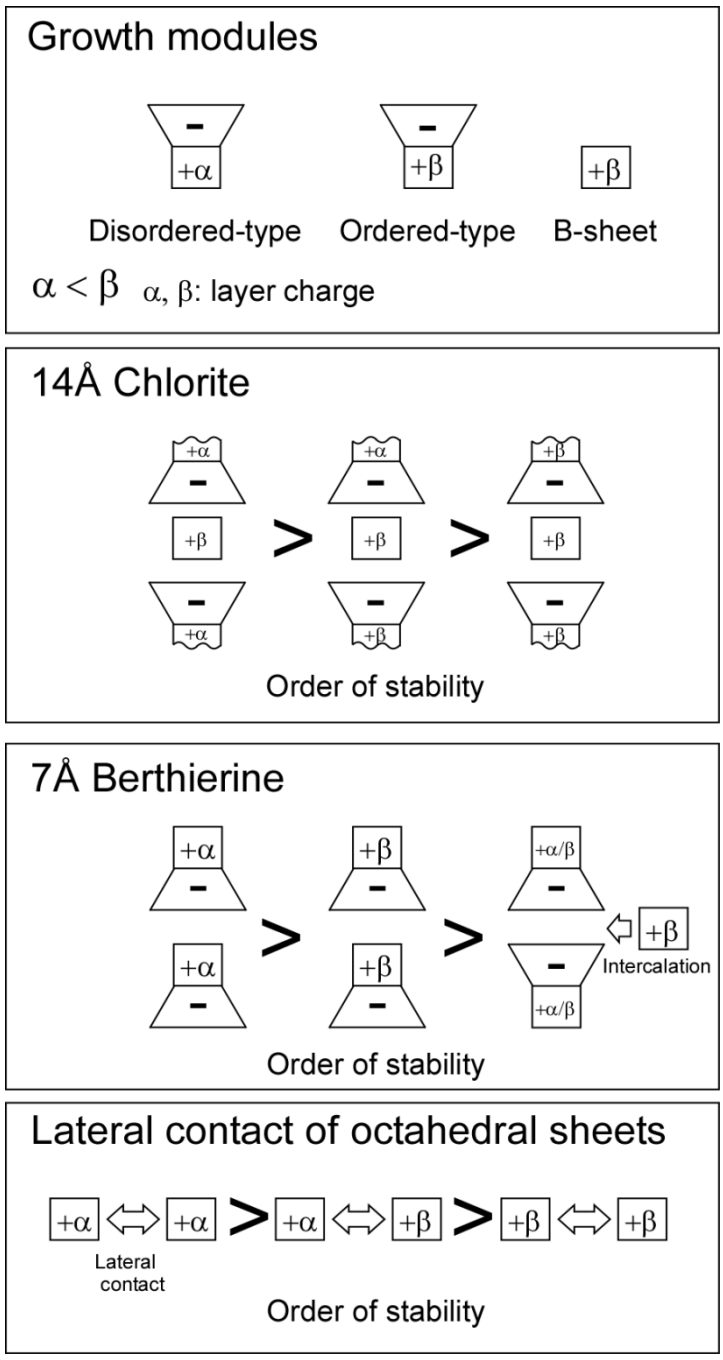

Figure VI-1. Schematic diagrams describing the growth modules and order of stability for 14Å chlorite, 7Å berthierine and lateral contacts of octahedral sheets.

Concerning the berthierine-chlorite transformation in diagenetic environments, the present study does not exclude the solid-state transformation model completely. It is because, the crystallization of berthierine and Fe-rich chlorite occurs for longer time periods than those for hydrothermal equivalents. From the chemical point of view, the possibility that 7Å precursor of pore-lining chlorite is odinite cannot be excluded. No lateral contact of opposite polar tetrahedral sheets was, in fact, observed. Therefore, we cannot discuss the detail mechanism of transformation from berthierine (or odinite) to chlorite at present, and the transformation mechanism is still open for the discussion. Further studies of these minerals combined with HRTEM and HAADF-STEM provide an insight into understanding the genesis, transformation mechanism, and crystallochemistry of chlorite and berthierine.

In conclusion, during the formation of a large crystal of Mg-rich chlorite, the structural irregularities must eventually become metastable relative to fully ordered form as the appropriate dimensions increase indefinitely. This is obvious on the basis of many previous studies of Mg-chlorite. On the contrary, fine-grained Fe-rich chlorites with complex structural and chemical irregularities can occur because they would be stabilized by the stacking disorder. The present study is a good example showing that HRTEM and HAADF-STEM are capable of visualizing the complex structural and chemical irregularities in the phyllosilicate minerals. Further HRTEM and HAADF-STEM observations of natural and synthetic chlorites may describe the polymorphic relationships between serpentine group mineral and chlorite from the crystallochemical point of view. In addition, they are expected to visualize the formation and transformation mechanisms of phyllosilicate minerals as well as chlorites and 7Å-14Å interstratified minerals at atomic scale.

ACKNOWLEDGMENT

I am grateful to Prof. Toshihiro Kogure for suggesting this thesis, as well as his continual support. I also appreciate his criticism, suggestions and guidance. Special mention goes to Prof. Tetsuro Yoneda of Hokkaido University, Prof. Stephen Hillier of the James Hutton Institute, Prof. Atsuyuki Inoue of Chiba University and Prof. Shigenori Ogihara for their kindly providing the chlorite samples used in the present study; in particular to A. Inoue for his providing unpublished microthermometric data of fluid inclusions. I thank Dr. Takeshi Kasama of Center for electron nanoscopy of Technical University of Denmark for the guidance and support for EELS study. During the course of the thesis, I received many helpful discussions and suggestions from Prof. Takashi Murakami, Prof. Yoshio Takahashi and Prof. Yohey Suzuki. The suggestions and discussions with Prof. Hiroyuki Kagi were also valuable and appreciated to improve the thesis.

I also thank Dr. Akihito Kumamoto and Prof. Eita Tochigi for the supports and valuable discussions for HAADF-STEM observations. Mr. Koji Ichimura helped me to use SEM. Ms. Eiko Fuji supported me for the TEM specimen preparations.

Acknowledgment is made to a Research Fellowship of the Japan Society for the Promotion of Science (JSPS) and "Nanotechnology Platform" (project No.12024046) of the Ministry of Education, Culture, Sports, Science and Technology (MEXT), Japan for support of this research.

REFERENCES

Aagaard, P., Jahren, J., Harstad, A., Nilsen, O., and Ramm, M. (2000) Formation of grain-coating chlorite in sandstones. Laboratory synthesized vs. natural occurrences. *Clay Minerals*, **35**, 261-269.

Ahn, J. H. and Peacor, D. R. (1985) Transmission electron microscopic study of diagenetic chlorite in Gulf Coast argillaceous sediments. *Clays and Clay Minerals*, **33**, 228-236.

Aplin, A. C., Matenaar, I. F., McCarty, D. K., and van der Pluijm, B. A. (2006) Influence of mechanical compaction and clay mineral diagenesis on the microfabric and pore-scale properties of deep-water Gulf of Mexico mudstones. *Clays and Clay Minerals*, **54**, 500-514.

Bailey, S. W. (1969) Polytypism of Trioctahedral 1:1 Layer Silicates. *Clays and Clay Minerals*, **17**, 355-371.

Bailey, S. W. (1980) Summary of recommendations of AIPEA nomenclature committee. *Clay Minerals*, **15**, 85-93.

Bailey, S. W. (1988a) Chlorites: structures and crystal chemistry. In: *Hydrous Phyllosilicates (Exclusive of Mica)* (S.W. Bailey editor), *Reviews in Mineralogy*, **19**, 347-403.

Bailey, S. W. (1988b) Polytypism of 1:1 layer silicates. In: *Hydrous Phyllosilicates (Exclusive of Mica)* (S.W. Bailey editor), *Reviews in Mineralogy*, **19**, 9-27.

Bailey, S. W. (1988c) Structures and compositions of other trioctahedral 1: 1 phyllosilicates In: *Hydrous Phyllosilicatse (Exclusive of Mica)* (S.W. Bailey editor),

Reviews in Mineralogy, **19**, 169-188.

Bailey, S. W. (1988d) Odinite, a new dioctahedral-trioctahedral Fe^{3+}-rich 1: 1 clay mineral. *Clay minerals*, **23**, 237-247.

Bailey, S. W. and Brown, G. (1962) Chlorite Polytypism: I. regular and semirandom one-layer structures. *American Mineralogist*, **47**, 819-850.

Bailey, S. W., Banfield, J. F., Barker, W. W., and Katchan, G. (1995) Dozyite, a 1:1 regular interstratification of serpentine and chlorite. *American Mineralogist*, **80**,65-77.

Banfield, J. F. and Bailey, S. W. (1996) Formation of regularly interstratified serpentine-chlorite minerals by tetrahedral inversion in long-period serpentine polytypes. *American Mineralogist*, **81**, 79-91.

Banfield, J. F. and Zhang, H. (2001) Nanoparticles in the environment. In: *Nanoparticles and the Environment* (J.F. Banfield and A. Navrotsky, editors), *Reviews in Mineralogy and Geochemistry*, **44**, 1-58.

Banfield, J. F., Bailey, S. W., and Barker, W. W. (1994) Polysomatism, polytypism, defect microstructures, and reaction mechanisms in regularly and randomly interstratified serpentine and chlorite. *Contributions to Mineralogy and Petrology*, **117**, 137-150.

Barker, C. E. and Pawlewicz, M. J. (1986) The correlation of vitrinite reflectance with maximum temperature in humic organic matter. In: *Paleogeothermics* (G. Buntebarth and L. Stegena, editors), 79-93.

Baronnet, A. (1992) Polytypism and stacking disorder. In: *Minerals and Reactions at the Atomic Scale: Transmission Electron Microscopy* (P. R. Buseck, editor), *Reviews in Mineralogy*, **27**, 231-288.

Bayliss, P. (1975) Nomenclature of the trioctahedral chlorites. *Canadian mineralogist*, **13**, 178.

Beaufort, D. and Meunier, A. (1994) Saponite, corrensite and chlorite-saponite mixed-layers in the Sancerre-Couy deep drill-hole (France). *Clay Minerals*, **29**, 47-61.

Beaufort, D., Baronnet, A., Lanson, B., and Meunier, A. (1997) Corrensite: a single phase or a mixed-layer phyllosilicate in the saponite-to-chlorite conversion series? A case study of Sancerre-Couy deep drill hole (France). *American Mineralogist*, **82**, 109-124.

Beaufort, D., Rigault, C., Billon, S., Billault, V., Inoue, A., Inoue, S., and Patrier, P. (in press) Chlorite and chloritization processes through mixed-layer mineral series in low-temperature geological systems - a review. *Clay Minerals*.

Bhattacharyya, D. P. (1983) Origin of berthierine in ironstones. *Clays and clay minerals*, **31**, 173-182.

Biernacka, J. (2014) Pore-lining sudoite in Rotliegend sandstones from the eastern part of the Southern Permian Basin. *Clay Minerals*, **49**, 635-655.

Bish, D. L. and R. Giese (1981) Interlayer bonding in IIb chlorite. *American Mineralogist*, **66**, 1216-1220.

Billault, V. (2002) *Texture, structure et propriétés cristallochimiques des chlorites ferreuses dans les réservoirs gréseux*. PhD thesis, Université de Poitiers, pp188.

Billault, V., Beaufort, D., Baronnet, A., and Lacharpagne, J. C. (2003) A nanopetrographic and textural study of grain-coating chlorites in sandstone reservoirs. *Clay Minerals*, **38**, 315-328.

Blanc, P., Gailhanou, H., Rogez, J., Mikaelian, G., Kawaji, H., Warmont, F., Gaboreau,

S., Grangeon, S., Grenèche, J.-M., Vieillard, P., Fialips, C., Giffaut, E., Gaucher, E., and Claret, F. (2014) Thermodynamic properties of chlorite and berthierine derived from calorimetric measurements. *Physics and Chemistry of Minerals*, **41**, 603-615.

Bourdelle, F. and Cathelineau, M. (2015) Low-temperature chlorite geothermometry: a graphical representation based on a T–R^{2+}–Si diagram. *European Journal of Mineralogy*, **27**, 617-626.

Bourdelle, F., Parra, T., Chopin, C., and Beyssac, O. (2013) A new chlorite geothermometer for diagenetic to low-grade metamorphic conditions. *Contributions to Mineralogy and Petrology*, **165**, 723-735.

Brindley, G. W. (1982) Chemical-compositions of berthierines - a review. *Clays and Clay Minerals*, **30**, 153-155.

Brindley, G. W. and Ali, S. C. (1950) X-ray study of thermal transformations in some magnesian chlorite minerals. *Acta Crystallographica*, **3**, 25-30.

Buatier, M. D., Früh-Green, G. L., and Karpoff, A. M. (1995) Mechanisms of Mg-phyllosilicate formation in a hydrothermal system at a sedimented ridge (Middle Valley, Juan de Fuca). *Contributions to Mineralogy and Petrology*, **122**, 134-151.

Buddington, A. F. (1935) High-temperature mineral associations at shallow to moderate depths. *Economic geology and the bulletin of the Society of Economic Geologists*, **30**, 205-222.

Cassagnabère, A. (1998) *Characterization and interpretation of kaolinite-to-dickite transition in Froy and Rind hydrocarbons reservoirs (North Sea, Norway)*. PhD thesis, University of Poitiers, pp237.

Cathelineau, M. and Nieva, D. (1985) A chlorite solid solution geothermometer the Los Azufres (Mexico) geothermal system. *Contributions to Mineralogy and Petrology*,

91, 235-244.

Chernosky, J. V., Berman, R. G., and Bryndzia, L. T. (1988) Stability, phase relations, and thermodynamic properties of chlorite and serpentine group minerals. In: *Hydrous Phyllosilicates (Exclusive of Mica)* (S.W. Bailey, editor), *Reviews in Mineralogy*, **19**, 295-346.

Cho, M. S. and Fawcett, J. J. (1986) A kinetic study of clinochlore and its high temperature equivalent forsterite-cordierite-spinel at 2 kbar water pressure. *American Mineralogist*, **71**, 68-77.

Cowley, J. M. (1969) Image contrast in a transmission scanning electron microscope. *Applied Physics Letters*, **15**, 58-59.

Curtis, C. D., Hughes, C. R., Whiteman, J. A., and Whittle, C. K. (1985) Compositional variation within some sedimentary chlorites and some comments on their origin. *Mineralogical Magazine*, **49**, 375-386.

Dalla Torre, M., Livi, K. J. T., Veblen, D. R., and Frey, M. (1996) White K-mica evolution from phengite to muscovite in shales and shale matrix melange, Diablo Range, California. *Contributions to Mineralogy and Petrology*, **123**, 390-405.

De Caritat, P., Hutcheon, I., and Walshe, J. L. (1993) Chlorite geothermometry: a review. *Clays and Clay Minerals*, **41**, 219-239.

Drits, V. A., Ivanovskaya, T. A., Sakharov, B. A., Zviagina, B. B., Gor'kova, N. V., Pokrovskaya, E. V., and Savichev, A. T. (2011) Mixed-layer corrensite-chlorites and their formation mechanism in the glauconitic sandstone-clayey rocks (Riphean, Anabar Uplift). *Lithology and Mineral Resources*, **46**, 566-593.

Ehrenberg S. N. (1991) Clay mineral studies at the geological laboratory, Statoil. *Proceedings of 7th Euroclay Conference, Dresden*, 319-322.

Ehrenberg, S. N. (1993) Preservation of anomalously high porosity in deeply buried sandstones by grain-coating chlorite: examples from the Norwegian continental shelf. *AAPG Bulletin*, **77**, 1260-1286.

Guggenheim, S., Adams, J. M., Bain, D. C., Bergaya, F., Brigatti, M. F., Drits, V. A., Formoso, M. L. L., Galán, E., Kogure, T. and Stanjek, H. (2006) Summary of recommendations of nomenclature committees relevant to clay mineralogy: report of the Association Internationale pour l'Etude des Argiles (AIPEA) Nomenclature Committee for 2006. *Clay Minerals*, **41**, 863-877.

Hayes, J. B. (1970) Polytypism of chlorite in sedimentary rocks. *Clays and Clay Minerals*, **18**, 285-306.

Hillier, S. (1993) Origin, diagenesis, and mineralogy of chlorite minerals in Devonian lacustrine mudrocks, Orcadian Basin, Scotland. *Clays and Clay Minerals*, **41**, 240-259.

Hillier, S. (1994) Pore-Lining Chlorites in Siliciclastic Reservoir Sandstones: Electron-Microprobe, SEM and XRD Data, and Implications for Their Origin. *Clay Minerals*, **29**, 665-679.

Hillier, S. and Velde, B. (1992) Chlorite interstratified with a 7-Å mineral - an example from offshore Norway and possible implications for the interpretation of the composition of diagenetic chlorites. *Clay Minerals*, **27**, 475-486.

Hillier, S. and Marshall, J. E. A. (1992) Organic maturation, thermal history and hydrocarbon generation in the Orcadian Basin, Scotland. *Journal of the Geological Society*, **149**, 491-502.

Hillier, S., Fallick, A., and Matter, A. (1996) Origin of pore-lining chlorite in the aeolian Rotliegend of northern Germany. *Clay Minerals*, **31**, 153-171.

Horn D. (1965) Diagenese und Porosität des Dogger-beta-Hauptsandsteines in den Ölfeldern PlönOst und Preetz. *Erdöl und Kohle Erdgas Petrochemie*, **18**, 249-255.

Hornibrook, E. R. and Longstaffe, F. J. (1996) Berthierine from the Lower Cretaceous Clearwater Formation, Alberta, Canada. *Clays and Clay Minerals*, **44**, 1-21.

Houseknecht D. W. (1987) Thermal maturity and sandstone reservoir quality, Atoka Formation , Arkoma Basin. *SEPM Mid-continent section, short course*.

Iijima, A. and Matsumoto, R. (1982) Berthierine and chamosite in Coal Measures of Japan. *Clays and Clay Minerals*, **30**, 264-274.

Imai, H., Lee, M. S., Iida, K., Fujiki, Y., and Takenouchi, S. (1975) Geologic structure and mineralization of the xenothermal vein-type deposits in Japan. *Economic Geology*, **70**, 647-676.

Inoue, A. and Utada, M. (1991) Smectite-to-chlorite transformation in thermally metamorphosed volcanoclastic rocks in the Kamikita Area, Northern Honshu, Japan. *American Mineralogist*, **76**, 628-640.

Inoue, A., Kurokawa, K., and Hatta, T. (2010) Application of chlorite geothermometry to hydrothermal alteration in Toyoha geothermal system, southwestern Hokkaido, Japan. *Resource Geology*, **60**, 52-70.

Inoue, A., Kurokawa, K., and Nitta, M. (2012) Environment of mineral-fluid interactions in the Toyoha hydrothermal system, southwestern Hokkaido, Japan. *Clay Science*, **16**, 59-81.

Inoue, A., Utada, M., Nagata, H., and Watanabe, T. (1984) Conversion of trioctahedral smectite to interstratified chlorite/smectite in Pliocene acidic pyroclastic sediments of the Ohyu district, Akita prefecture, Japan. *Clay Science*, **6**,103-116.

Inoue, A., Meunier, A., Patrier-Mas, P., Rigault, C., Beaufort, D., and Vieillard, P.

(2009) Application of chemical geothermometry to low-temperature trioctahedral chlorites. *Clays and Clay Minerals*, **57**, 371-382.

Ishizuka, K. (2002) A practical approach for STEM image simulation based on the FFT multislice method. *Ultramicroscopy*, **90**, 71-83.

Jahren, J. and Aagaard, P. (1989) Compositional variations in diagenetic chlorites and illites, and relationships with formation-water chemistry. *Clay Minerals*, **24**, 157-170.

James, R. S., Turnock, A. C., and Fawcett, J. J. (1976) The stability and phase relations of iron chlorite below 8.5 kb pH_2O. *Contributions to Mineralogy and Petrology*, **56**, 1-25.

Jiang, W.-T. and Peacor, D. R. (1994) Formation of corrensite, chlorite and chlorite-mica stacks by replacement of detrital biotite in low-grade pelitic rocks. *Journal of Metamorphic Geology*, **12**, 867-884.

Jiang, W. T., Peacor, D. R., and Slack, J. F. (1992) Microstructures, mixed layering, and polymorphism of chlorite and retrograde berthierine in the Kidd Creek massive sulfide deposit, Ontario. *Clays and Clay Minerals*, **40**, 501-514.

Kilaas, R. (1998) Optimal and near-optimal filters in high-resolution electron microscopy. *Journal of Microscopy*, **190**, 45-51.

Kogure, T. and Bando, Y. (1998) Formation of ZnO nanocrystallites on ZnS surfaces by electron beam irradiation. *Journal of Electron Microscopy*, **47**, 135-141.

Kogure, T. and Banfield, J. F. (1998) Direct identification of the six polytypes of chlorite characterized by semi-random stacking. *American Mineralogist*, **83**, 925-930.

Kogure, T. and Banfield, J. F. (2000) New insights into the mechanism for chloritization

of biotite using polytype analysis. *American Mineralogist*, **85**, 1202-1208.

Kogure, T. and Drits, V. A. (2010) Structural changes in celadonite and cis-vacant illite by electron radiation in TEM. *Clays and Clay Minerals*, **58**, 522-531.

Kogure, T. and Okunishi, E. (2010) Cs-corrected HAADF-STEM imaging of silicate minerals. *Journal of Electron Microscopy*, **59**, 263-71.

Kogure, T., Hybler, J., and Durovic, S. (2001) A HRTEM study of cronstedtite: determination of polytypes and layer polarity in trioctahedral 1: 1 phyllosilicates. *Clays and Clay Minerals*, **49**, 310-317.

Kogure, T., Drits, V. A., and Inoue, S. (2013) Structure of mixed-layer corrensite-chlorite revealed by high-resolution transmission electron microcopy (HRTEM). *American Mineralogist*, **98**, 1253-1260.

Lanari, P., Wagner, T., Vidal,O. (2014). A thermodynamic model for di-trioctahedral chlorite from experimental and natural data in the system MgO–FeO–Al_2O_3–SiO_2–H_2O: applications to P–T sections and geothermometry. *Contributions to Mineralogy and Petrology*, **167**, 1-19.

Lumsden, D. N., Pittman, R. E. and Heald, M. T. (1992) Clay coats: occurrence and relevance to preservation of porosity in sand stones. In: *Origin, Diagenesis and Petrophysics of Clay Minerals in Sandstones* (D. W. Housknecht and E. D. Pittman editors), **47**, 241-255.

Marks, L. D. (1996) Wiener-filter enhancement of noisy HREM images. *Ultramicroscopy*, **62**, 43-52.

McMurchy, R. C. (1934) The crystal structure of the chlorite minerals. *Zeitschrift für Kristallographie-Crystalline Materials*, **88**, 420-432.

Meunier, A. (2005) *Clays*. Springer, Berlin, pp 472.

Meunier, A. (2010) Formation mechanisms of mixed-layer clay minerals In: *Interstratified Clay Minerals: Origin, Characterization and Geochemical Significance* (S. Fiore, J. Cuadros and F. J. Huertas editors), *AIPEA Educational Series*, **1**, 53-72.

Moore, D. M. and Reynolds, R. C. (1989) *X-ray Diffraction and the Identification and Analysis of Clay Minerals*. Oxford University press New York, 332 pp.

Mosser-Ruck, R., Cathelineau, M., Guillaume, D., Charpentier, D., Rousset, D., Barres, O., and Michau, N. (2010) Effects of temperature, pH, and iron/clay and liquid/clay ratios on experimental conversion of dioctahedral smectite to berthierine, chlorite, vermiculite, or saponite. *Clays and Clay Minerals*, **58**, 280-291.

Murakami, T., Sato, T., and Inoue, A. (1999) HRTEM evidence for the process and mechanism of saponite-to-chlorite conversion through corrensite. *American Mineralogist*, **84**, 1080-1087.

Nakamura, T. (1970) Mineral zoning and characteristic minerals in the polymetallic veins of the Ashio copper mine. *Volcanism and Ore genesis*, 231-246.

Nelson, B. W. and Roy, R. (1958) Synthesis of the chlorites and their structural and chemical constitution. *American Mineralogist*, **43**, 707-725.

Okumura, T., Tamura, K., Fujii, E., Yamada, H., and Kogure, T. (2014) Direct observation of cesium at the interlayer region in phlogopite mica. *Microscopy*, **63**, 65-72.

Parra, T., Vidal, O., and Theye, T. (2005) Experimental data on the Tschermak substitution in Fe-chlorite. *American Mineralogist*, **90**, 359-370.

Pauling, L. (1930) The structure of the chlorites. Proceedings of the National Academy of Sciences of the United States of America, **16**, 578.

Penn, R.L. and Banfield, J.F. (1998) Imperfect oriented attachment: dislocation generation in defect-free nanocrystals. *Science*, **281**, 969-971.

Pennycook, S., J. and Nellist, P., D. (2011) *Scanning Transmission Electron Microscopy Imaging and Analysis*. Springer-Verlag, New York, 762 pp.

Pennycook, S. J. and Jesson, D. E. (1992) Atomic resolution Z-contrast imaging of interfaces. *Acta Metallurgica et Materialia*, **40**, S149-S159.

Reynolds, R. (1985) NEWMOD—a computer program for the calculation of one-dimensional diffraction patterns of mixed-layered clays. 8 Brook Road Hanover, New Hampshire.

Reynolds, R. (1988) Mixed layer chlorite minerals. In: *Hydrous Phyllosilicates (Exclusive of Mica)* (S.W. Bailey, editor), *Reviews in Mineralogy*, **19**, 601-629.

Reynolds, R. C., Distefano, M. P., and Lahann, R. W. (1992) Randomly interstratified serpentine/chlorite: its detection and quantification by powder X-ray diffraction methods. *Clays and Clay Minerals*, **40**, 262-267.

Rivard, C., Pelletier, M., Michau, N., Razafitianamaharavo, A., Bihannic, I., Abdelmoula, M., Ghanbaja, J., and Villieras, F. (2012) Berthierine-like mineral formation and stability during the interaction of kaolinite with metallic iron at 90 ºC under anoxic and oxic conditions. *American Mineralogist*, **98**, 163-180.

Rule, A. C. and Bailey, S. (1987) Refinement of the crystal structure of a monoclinic ferroan clinochlore. *Clays and Clay Minerals*, **35**, 129-138.

Ryan, P. C. and Reynolds, R. C. (1996) The origin and diagenesis of grain-coating serpentine-chlorite in Tuscaloosa Formation sandstone, US Gulf Coast. *American Mineralogist*, **81**, 213-225.

Schmidt, D. and Livi, K. J. (1999) HRTEM and SAED investigations of polytypism,

stacking disorder, crystal growth, and vacancies in chlorites from Subgreenschist facies outcrops. *American Mineralogist*, **84**, 160-170.

Shau, Y. H. and Peacor, D. R. (1992) Phyllosilicates in hydrothermally altered basalts from DSDP Hole 504B, Leg 83—a TEM and AEM study. *Contributions to Mineralogy and Petrology*, **112**, 119-133.

Shikazono, N. (2003) *Geochemical and Tectonic Evolution of Arc-Backarc Hydrothermal Systems: Implication for the Origin of Kuroko and Epithermal Vein-Type Mineralizations and the Global Geochemical Cycle*. Elsevier, Amsterdam, 463 pp.

Shirozu, H. (1978) Chlorite minerals. *Developments in sedimentology*, **26**, 243-264.

Shirozu, H. (1988) *Introduction to Clay Mineralogy -Fundamentals for Clay Science-*. Asakura Publishing, Tokyo, 176 pp (*in Japanese*).

Shirozu, H. and Bailey, S. W. (1965) Chlorite polytypism: III. crystal structure of an orthohexagonal iron chlorite. *American Mineralogist*, **50**, 868-885.

Slack, J. F. and Coad, P. R. (1989) Multiple hydrothermal and metamorphic events in the Kidd Creek volcanogenic massive sulphide deposit, Timmins, Ontario: evidence from tourmalines and chlorites. *Canadian Journal of Earth Sciences*, **26**, 694-715.

Slack, J. F., Jiang, W. T., Peacor, D. R., and Okita, P. M. (1992) Hydrothermal and metamorphic berthierine from the Kidd Creek volcanogenic massive sulfide deposit, Timmins, Ontario. *Canadian Mineralogist*, **30**, 1127-1142.

Smith, J. V. and Yoder, S. B. (1956) Experimental and theoretical studies of the mica polymorphs. *Mineralogical Magazine*, **31**, 209-235.

Smyth, J. R., Dyar, M. D., May, H. M., Bricker, O. P., Acker, J. G. (1997) Crystal structure refinement and Mössbauer spectroscopy of an ordered, triclinic clinochlore.

Clays and Clay Minerals, **45**, 544-550.

Steinfink, H. (1958a) The crystal structure of chlorite. I.a monoclinic polymorph. *Acta Crystallographica*, **11**, 191-195.

Steinfink, H. (1958b) The crystal structure of chlorite. II. a triclinic polymorph. *Acta Crystallographica*, **11**, 195-198.

Sudo, T. (1974) *Clay Mineralogy*. Iwanami-shoten, Tokyo, 498 pp (*in Japanese*).

Taylor, K. (1990) Berthierine from the non-marine Wealden (Early Cretaceous) sediments of south-east England. *Clay Minerals*, **25**, 391-399.

Turnock, A. (1960) The stability of iron chlorites. *Carnegie Institute of Washington Year book*, **59**, 98-103.

Velde, B. (1985) *Clay Minerals: A physico-chemical explanation of their occurrence*. Elsevier, Amsterdam, 427 pp.

Vidal, O. (2005) Thermodynamic properties of the Tschermak solid solution in Fe-chlorite: application to natural examples and possible role of oxidation. *American Mineralogist*, **90**, 347-358.

Vidal, O., Parra, T., and Trotet, F. (2001) A thermodynamic model for Fe-Mg aluminous chlorite using data from phase equilibrium experiments and natural pelitic assemblages in the 100° to 600°C, 1 to 25 kb range. *American Journal of Science*, **301**, 557-592.

Walker, J. R. (1993) Chlorite polytype geothermometry. *Clays and Clay Minerals*, **41**, 260-267.

Walker, J. R. and Thompson, G. R. (1990) Structural variations in chlorite and illite in a diagenetic sequence from the Imperial-Valley, California. *Clays and Clay Minerals*, **38**, 315-321.

Walshe, J. L. (1986) A six-component chlorite solid solution model and the conditions of chlorite formation in hydrothermal and geothermal systems. *Economic Geology*, **81**, 681-703.

Weaver, C. E., Highsmith, P. B., and Wampler, J. M. (1984) Chlorite. In: *Shale-slate Metamorphism in the Southern Apparalachians* (C.E. Weaver, editor). Elsevier, Amsterdam, 99-139.

Welch, M. D., Barras, J., and Klinowski, J. (1995) A multinuclear NMR study of clinochlore. *American Mineralogist*, **80**, 441-447.

Wiewióra, A. and Weiss, Z. (1990) Crystallochemical classifications of phyllosilicates based on the unified system of projection of chemical composition: II. the chlorite group. *Clay Minerals,* **25**, 83-92.

Worden, R. H. and Morad, S. (2003) Clay minerals in sandstones: controls on formation, distribution and evolution. In: *Clay Mineral Cements in Sandstones* (R.H. Worden and S. Morad, editors). Blackwell Publishing Ltd., 3-41.

Xu, H. F. and Veblen, D. R. (1996) Interstratification and other reaction microstructures in the chlorite-berthierine series. *Contributions to Mineralogy and Petrology*, **124**, 291-301.

Zheng, H. and Bailey, S. W. (1989) Structures of intergrown triclinic and monoclinic IIb chlorites from Kenya. *Clays and Clay Minerals*, **37**, 308-316.

Zimmerle, W. (1963) Zu Petrographie und Diagenese des Dogger-beta-Hauptsandsteins im Erdölfeld Plön-Ost. Erdöl und Kohle Erdgas Petrochemies. **16**, 249-255

Appendix I: METHOD TO OBTAIN CRYSTALLOGRAPHIC INFORMATION FROM SELECTED AREA IN THE PETROGRAPHIC THIN SECTION

A. 1. INTRODUCTION

A weak point of HREM study is often expressed as “cannot see the wood for the trees”. The spatial resolution of powder XRD is too low to clarify the differences in the structural features of the minerals showing different textures and/or chemical compositions in the petrographic thin sections. Combination of FIB and TEM, on the other hand, can overcome such weak point of powder XRD, whereas it is sometimes difficult to conclude whether observed structural features are statistically valid. Usually, the validity is confirmed by taking many images in a specimen and by complimentary XRD analyses. The analytical techniques which have the spatial resolution in-between may be useful to overcome the difficulties of both XRD and FIB-TEM.

Electron backscatter diffraction (EBSD) is one of such techniques to obtain crystallographic information from specimens in a scanning electron microscope (SEM). The EBSD pattern is a Kikuchi pattern formed by back scattered electrons. The pattern is projected on a wide phosphor screen close to the specimen surface, and generally digitized and stored to a personal computer. By analyzing the EBSD patterns, mineral phase and crystal orientation can be instantly determined (Prior *et al.*, 1999). EBSD is successfully applied to identify polymorphs and to obtain “crystal orientation maps” for texture analyses of polycrystalline materials like steel or rocks, determined from orientations of individual crystals in SEM (*e.g.* Dingley and Randle, 1992; Humphreys,

2004). EBSD also enables to distinguish the polytypes of phyllosilicates (serpentine, mica, chlorite, and kaolin group minerals) in SEM (Kogure, 2002; Kogure and Tachikawa, 2002; Kogure *et al.*, 2005). The patterns must be clear and sharp to discriminate the polytypes. The phyllosilicate in the petrographic thin sections generally appear with layers terminated by the polished surface. Moreover, chlorite polytypic groups are only distinguishable from Y direction (Kogure and Banfield, 2000). Especially, for the purpose of the present study, it is desirable to obtain EBSD patterns of good quality from the X and Y directions. EBSD patterns acquired from the Z direction, *i.e.* (001) cleaved surfaces, of phyllosilicates are sufficient for the polytype discrimination, whereas those acquired from the other surfaces usually cannot endure the pattern analyses. To overcome such difficulties, the origin of this failure is investigated and an optimum sample preparation method to acquire EBSD patterns that are sharp enough to determine the polytypes of phyllosilicates is proposed. The results of this part have been reported in Inoue and Kogure (2012).

A. 2. METHODS

A. 2. 1. Petrographic thin section

The surface of petrographic thin sections was prepared by the following procedure. After gluing rock samples to glass slides, the samples were ground with coarse abrasive down to about 30 μm thick. Then the surface was ground and polished using #3000, #6000 grit abrasives and diamond paste (3 μm, 1 μm) in order. For EBSD analysis, the surface was further polished with colloidal silica suspension and polishing cloth on a Buehler Masterserv® 250 grinder-polisher for about 20 mins. Finally, a thin amorphous carbon film was coated on the section to prevent charge accumulation in the SEM.

A. 2. 2. EBSD

A Hitachi S-4500 SEM equipped with a ThermoNoran PhaseID EBSD system was used for EBSD analysis. The thin sections were mounted on a special holder to keep the surface normal of the section 70° from the vertical or incident electron beam. The acceleration voltage of electrons was 20 kV. Calculations of Kikuchi patterns and analyses of observed EBSD patterns were performed using a program coded with Visual Basic 6.0, developed by Kogure (2003).

Observations of the constituent minerals on petrographic thin sections were performed using a Hitachi S-4500 SEM with a cold field-emission gun and an yttrium-aluminum-garnet (YAG) back-scattered electron (BSE) detector and Kevex energy-dispersive X-ray spectrometer (EDS) equipped to the SEM. The acceleration voltage was 15kV for the observations and chemical analyses.

A. 2. 4. FIB-TEM

TEM specimens were prepared following the methods described in Chapter III. For the conditions of observations can be referred to Chapter III.

A. 3. RESULTS AND DISCUSSION

A. 3. 1. EBSD patterns from the polished and ion-beam-etched surfaces of phyllosilicates

Sectioned surfaces perpendicular to the basal planes, of large crystals of phlogopite from pegmatite (Yamanoo, Ibaraki, Japan) and chlorite (Yukinoura, Nagasaki, Japan; Shirozu 1980) were prepared by sandwiching them with hard epoxy resin between two

glass slides, slicing them together with a diamond wheel cutter, polishing the sectioned surfaces, and coating with carbon. As a reference, a polished surface of an Iceland spar calcite crystal was prepared simultaneously using the same polishing process. The acquired pattern from each surface is shown in Figure A-1. The patterns from muscovite and chlorite are so obscure that it is almost impossible to analyze the patterns. EBSD patterns are known to be generated in the vicinity of the crystal surface (Harland et al. 1981) and if one wishes to obtain sharp EBSD patterns from petrographic thin sections, their surfaces must be finished with a gentle polishing process, for instance polishing with colloidal silica instead of hard abrasives like diamond or alumina particles (Prior et al. 1999). The surface regions of minerals damaged by prior mechanical grinding are removed by polishing with colloidal silica which has the effects of both mechanical polishing and chemical etching. Thus, if the quality of obtained EBSD pattern is poor, one can immediately suspect the insufficient polishing of the sample surface. However, such possibility was excluded in the present study because the EBSD pattern obtained from calcite was clear and adequate for further EBSD pattern analysis. The present results suggest that a damage induced by the mechanical grinding cannot be removed by colloidal silica.

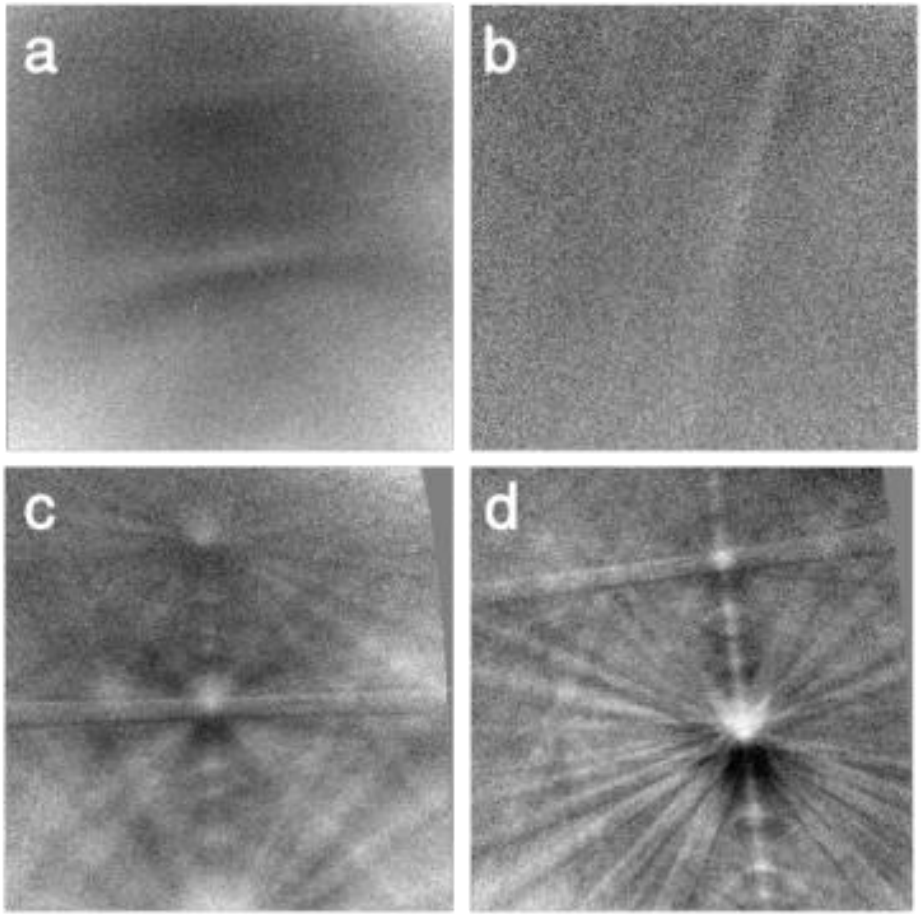

Figure A-1. (a, b) EBSD patterns from (a) muscovite and (b) chlorite mechanically polished using colloidal silica. (c, d) EBSD patterns from (c) muscovite and (d) chlorite after ion-beam etching for 2 hours. Reprinted from Inoue and Kogure (2012) with the permission of the Mineralogical Society of America.

In order to examine the state of sample surface, TEM specimen was prepared by FIB from the near-surface region of the phlogopite sample, perpendicular to the layers. A The TEM image (Figure A-2a) shows distinct bending of the phlogopite layers in the region from the surface to about 1 μm depth. Such crystal bending is expected to be formed by mechanical polishing, considering the flexible layers and dense microcleavages common in mica crystals. Because the position of Kikuchi bands in EBSD patterns is dependent on the crystal orientation, sharp Kikuchi bands cannot be

expected from such a bent crystal. This result indicated that the surface finished with mechanical polishing by colloidal silica is not sufficient for EBSD analyses of phyllosilicates. A possible alternative method is wet etching, using chemicals such as HF, to remove the damaged region at the surface caused by prior mechanical grinding. However, the etching rates of minerals by such chemicals are strongly dependent on mineral structures, compositions, orientation, defect density, etc. and a smooth surface, which is desirable for EBSD analyses, is not expected in case of petrographic thin sections.

In the present study, we adopted Ar ion milling to remove the bent crystals at the surface. For ion beam etching, thin sections 1 mm thick were cut into a square of less than 5 mm. They were loaded in a Gatan Model 600 Dual Ion Mill, commonly used to prepare TEM specimens. The conditions used were 3 kV energy of the Ar ion, an incident angle of 15° to the specimen surface, ~ 2 hours duration, and a specimen current of ~ 20 mA. Considering the routine process to prepare TEM specimens, in which the ion milling is continued until a hole is formed in silicate specimens of a certain thickness, the estimated thickness of etching with this ion milling condition, is roughly ~ 4 μm. It is known that ion milling can generate a damaged amorphous layer on the mineral surface by the implantation of the incident ions (e.g., McCaffrey *et al.*, 2001), which may also degrade EBSD patterns. Hence, the ion-beam-etched surface of phlogopite was evaluated in TEM (Figure A-2b and c). In order to identify the specimen surface, Pt-Pd thin film was coated just after the ion milling. Using ion milling, the bent crystals were successfully removed (Figure A-2b). The thickness of the damaged layer, which lies between the Pt-Pd film at the top and the lattice fringes of phlogopite, was less than 20 nm (Figure A-2c). The lattice fringes of ~ 1 nm spacing, which corresponds

to the unit layer of phlogopite, are sharp and not bent in the figure. The EBSD patterns from the phlogopite and chlorite specimens after the ion beam etching are sufficiently sharp and the polytype and crystal orientation can be unambiguously determined by analyzing these patterns (Figure A-1c and d). This result indicates that the damaged layer in Figure A-2c is negligible for the acquisition of the EBSD patterns from phyllosilicates after mechanical polishing.

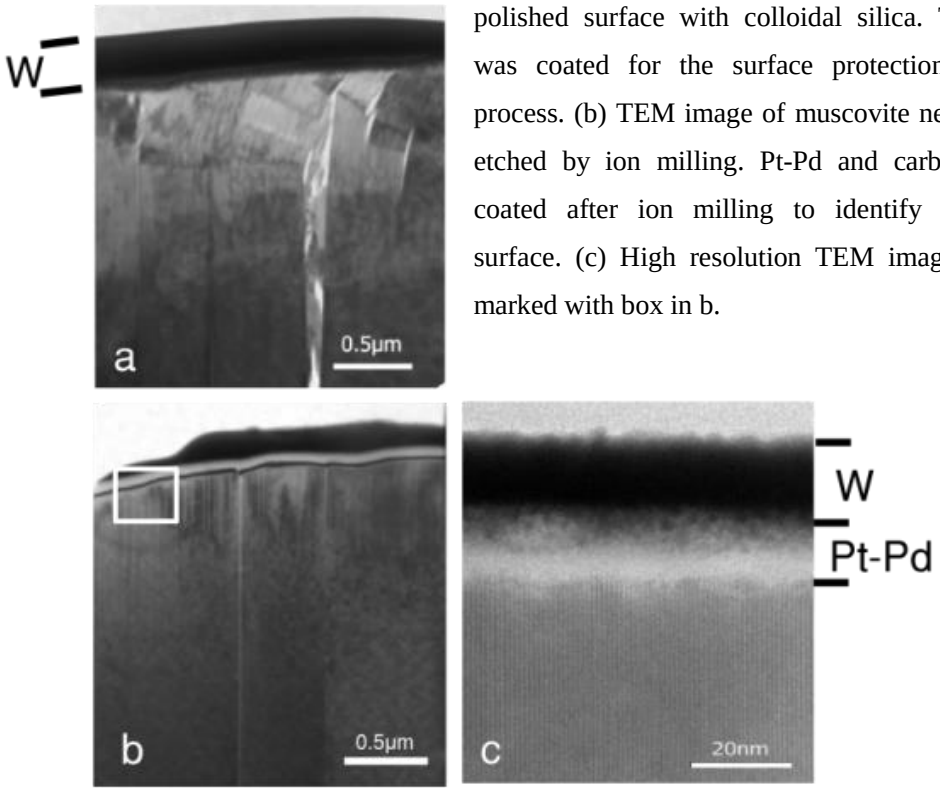

Figure A-2. (a) TEM image of sample near the polished surface with colloidal silica. Tungsten (W) was coated for the surface protection in the FIB process. (b) TEM image of muscovite near the surface etched by ion milling. Pt-Pd and carbon film were coated after ion milling to identify the specimen surface. (c) High resolution TEM image of the area marked with box in b.

A.3.2. Practical EBSD analysis of phyllosilicates in petrographic thin section

A petrographic thin section was made from staurolite schist collected in Unazuki area, Hida metamorphic terrain, Japan. The section was first polished with diamond paste and finished with colloidal silica, the normal sample preparation method for EBSD. Based on the petrographic observations, quartz, garnet (almandine), and chlorite were major

constituent minerals (Figure A-3a). EBSD patterns from chlorite in this section are shown in Figure A-3b. As the results described in the above section, the pattern from chlorite was obscure, whereas those from garnet and quartz were sufficiently sharp. Figure A-3c shows EBSD pattern of chlorite after ion beam etching. The EBSD pattern from chlorite has become clear enough and that from garnet was unchanged. Calculated Kikuchi patterns for chlorite II*bb* and I*bb* along the same crystal orientation as the experimental one are shown (Figures A-3d and e). Comparing the experimental and calculated Kikuchi patterns, the polytypic group of this chlorite is determined as II*bb*. It is because that some of the peaks which are visible in the experimental pattern (Figure A-3c) were not appeared in that of I*bb* (Figure A-3e).

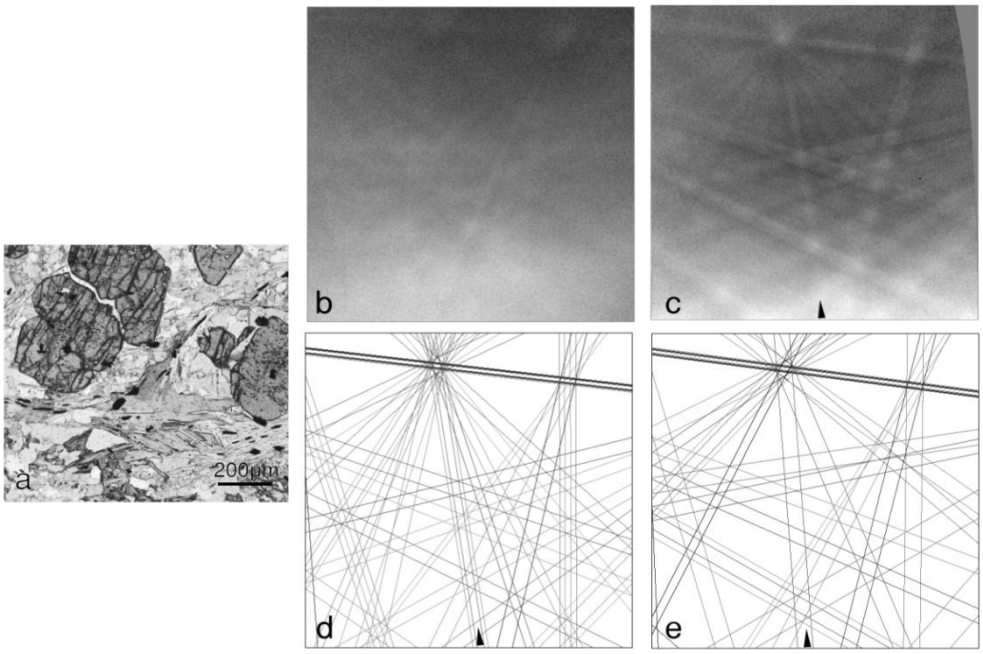

Figure A-3. (a) Optical micrograph of the petrographic thin section from staurolite schist. (b) EBSD pattern from chlorite polished with colloidal silica. (c) EBSD pattern obtained from the same chlorite grain after etching by ion milling. Calculated Kikuchi patterns for chlorite-II*bb* (d) and chlorite-I*bb* (e) in the same crystal orientation. The arrowheads in c and d indicate the corresponding Kikuchi bands which appear only in chlorite-II*bb*. Reprinted from Inoue and Kogure (2012) with the permission of the Mineralogical Society of America.

A.4. CONCLUSION

EBSD analysis of phyllosicates in petrographic thin sections is enabled by using ion beam etching. A minute problem is that the maximum size of the specimens processed by conventional ion milling apparatuses is limited. The area to be etched uniformly is also not large, and the surface is slightly roughened by ion beam etching, which may be an obstacle for quantitative X-ray chemical analysis using a fine electron probe. However, these problems could be overcome by optimizing the etching condition, e.g., the incident angle of the ion beam.

EBSD is expected to be used as the complementary tools of HRTEM. For instance, the author utilized EBSD to determine the crystal orientation of the phyllosilicate prior

to FIB samples preparation. It improves efficiency of FIB-TEM because the samples must be observed along the proper direction.

REFERENCES

Dingley, D. J. and Randle, V. (1992) Microtexture determination by electron back-scatter diffraction. *Journal of Materials Science*, **27**, 4545-4566.

Harland, C., Akhter, P., and Venables, J. (1981) Accurate microcrystallography at high spatial-resolution using electron backscattering patterns in a field-emission gun scanning electron-microscope. *Journal of Physics E-Scientific Instruments*, **14**, 175-182.

Humphreys, F. J. (2004) Characterisation of fine-scale microstructures by electron backscatter diffraction (EBSD). *Scripta Materialia*, **51**, 771-776.

Inoue, S. and Kogure, T. (2012) Electron backscatter diffraction (EBSD) analyses of phyllosilicates in petrographic thin sections. *American Mineralogist*, **97**, 755-758.

Kogure, T. and Banfield, J. F. (2000) New insights into the mechanism for chloritization of biotite using polytype analysis. *American Mineralogist*, **85**, 1202-1208.

Kogure, T. (2002) Identification of polytypic groups in hydrous phyllosilicates using electron backscattering patterns. *American Mineralogist*, **87**, 1678-1685.

Kogure, T. and Tachikawa, O. (2002) Application of electron back-scattering diffraction (EBSD) in mineralogy. *Japanese Magazine of Mineralogical and Petrological Sciences*, **31**, 275-282 (*in Japanese*).

Kogure, T. (2003) A program to assist kikuchi pattern analyses. *Journal of the Crystallographic Society of Japan*, **45**, 391-395.

Kogure, T., Inoue, A., and Beaufort, D. (2005) Polytype and morphology analyses of

kaolin minerals by electron back-scattered diffraction. *Clays and Clay Minerals*, **53**, 201-210.

McCaffrey, J., Phaneuf, M., and Madsen, L. (2001) Surface damage formation during ion-beam thinning of samples for transmission electron microscopy. *Ultramicroscopy*, **87**, 97-104.

Prior, D. J., Boyle, A. P., Brenker, F., Cheadle, M. C., Day, A., Lopez, G., Peruzzo, L., Potts, G. J., Reddy, S., Spiess, R., Timms, N. E., Trimby, P., Wheeler, J., and Zetterstrom, L. (1999) The application of electron backscatter diffraction and orientation contrast imaging in the SEM to textural problems in rocks. *American Mineralogist*, **84**, 1741-1759.

Shirozu, H. (1980) Variations of DTA and TG curves for Mg-chlorites. *Clay Science*, **5**, 237-244.

Appendix II. CHEMICAL COMPOSITIONS OF PORE-LINING CHLORITES, BERTHIERINE AND ODINITE REPORTED IN THE PREVIOUS STUDIES

Table A-II-1. Structural formulae calculated on the basis of O=14. Iron cations are regarded as a divalent.

	Curtis et al (1985)					
	Tuscaloosa sandstones					
Si	3.06	3.10	2.68	2.87	3.12	3.08
Al(IV)	0.94	0.90	1.32	1.14	0.88	0.93
ΣTetrahedral cations	4.00	4.00	4.00	4.00	4.00	4.00
Al(VI)	1.52	1.27	1.53	1.77	1.68	1.16
Ti	0.01	0.00	0.02	0.01	0.02	0.06
Fe	2.88	2.39	2.56	2.93	2.75	3.49
Mg	1.15	1.98	1.59	0.84	1.00	0.73
Mn	0.02	0.06	0.01	0.01	0.01	0.00
Ca	0.03	0.04	0.04	0.01	0.03	0.15
Na	0.00	0.00	0.09	0.00	0.00	0.00
K	0.03	0.00	0.01	0.01	0.02	0.21
ΣOctahedral cations	5.62	5.73	5.83	5.57	5.50	5.80
No. of vacancies	0.38	0.27	0.17	0.43	0.50	0.20
Fe/(Fe+Mg)	0.71	0.55	0.62	0.78	0.73	0.83

Table A-II-1. (Continued)

	Curtis et al (1985)					
	North Sea sandstones					
Si	2.91	2.72	2.73	2.98	2.78	2.67
Al(IV)	1.10	1.29	1.28	1.03	1.23	1.33
ΣTetrahedral cations	4.00	4.00	4.00	4.00	4.00	4.00
Al(VI)	1.67	1.37	1.44	1.69	1.40	1.55
Ti	0.00	0.00	0.01	0.01	0.00	0.00
Fe	2.16	2.30	2.57	1.83	2.20	1.99
Mg	1.78	2.12	1.75	2.01	2.19	2.24
Mn	0.00	0.00	0.01	0.00	0.00	0.00
Ca	0.02	0.03	0.01	0.00	0.01	0.01
Na	0.00	0.03	0.01	0.06	0.04	0.03
K	0.05	0.07	0.07	0.09	0.01	0.02
ΣOctahedral cations	5.66	5.91	5.85	5.67	5.84	5.83
No. of vacancies	0.34	0.09	0.15	0.33	0.16	0.17
Fe/(Fe+Mg)	0.55	0.52	0.60	0.48	0.50	0.47

Table A-II-1. (Continued)

	Curtis et al (1985)				
	Alaskan sandstones			Belly River sandstone	
Si	3.39	3.97	3.45	3.06	3.25
Al(IV)	0.62	0.03	0.55	0.94	0.76
ΣTetrahedral cations	4.00	4.00	4.00	4.00	4.00
Al(VI)	1.58	2.08	1.49	1.47	1.15
Ti	0.02	0.03	0.01	0.01	0.00
Fe	2.16	1.62	1.83	3.09	3.60
Mg	1.46	0.96	1.95	0.99	0.77
Mn	0.01	0.01	0.05	0.01	0.00
Ca	0.16	0.15	0.10	0.02	0.12
Na	0.02	0.11	0.04	0.04	0.00
K	0.04	0.08	0.05	0.02	0.05
ΣOctahedral cations	5.45	5.02	5.51	5.63	5.68
No. of vacancies	0.55	0.98	0.49	0.37	0.32
Fe/(Fe+Mg)	0.60	0.63	0.48	0.76	0.82

Table A-II-1. (Continued)

	Curtis et al (1985)				
	Belly River sandstone			Hamersley Group	
Si	2.90	2.87	3.05	2.71	2.76
Al(IV)	1.11	1.13	0.96	1.30	1.25
ΣTetrahedral cations	4.00	4.00	4.00	4.00	4.00
Al(VI)	1.77	1.67	0.67	1.21	1.28
Ti	0.02	0.01	0.00	0.00	0.01
Fe	2.55	2.85	4.50	2.85	2.94
Mg	1.20	1.06	0.59	1.85	1.61
Mn	0.01	0.01	0.00	0.00	0.00
Ca	0.01	0.02	0.09	0.00	0.00
Na	0.00	0.00	0.00	0.00	0.07
K	0.01	0.01	0.07	0.04	0.02
ΣOctahedral cations	5.55	5.61	5.90	5.94	5.91
No. of vacancies	0.45	0.39	0.10	0.06	0.09
Fe/(Fe+Mg)	0.68	0.73	0.88	0.61	0.65

Table A-II-1. (Continued)

	Curtis et al (1985)			Ahn and Peacor (1985)	
	Cambrian Welsh Slate			Chlorite	
Si	2.84	2.73	2.57	2.70	2.80
Al(IV)	1.17	1.28	1.43	1.30	1.20
ΣTetrahedral cations	4.00	4.00	4.00	4.00	4.00
Al(VI)	0.98	1.53	1.52	1.40	1.60
Ti	0.00	0.01	0.00	—	—
Fe	2.74	0.86	2.54	3.33	3.13
Mg	2.27	3.22	1.59	1.10	1.00
Mn	0.00	0.12	0.05	—	—
Ca	0.01	0.01	0.01	—	—
Na	0.00	0.23	0.10	—	—
K	0.03	0.04	0.02	—	—
ΣOctahedral cations	6.01	6.00	5.81	5.83	5.73
No. of vacancies	-0.01	0.00	0.19	0.17	0.27
Fe/(Fe+Mg)	0.55	0.21	0.61	0.75	0.76

Table A-II-1. (Continued)

	Ahn and Peacor (1985)				
	Chlorite (continue)				
Si	2.80	2.70	2.90	2.80	2.70
Al(IV)	1.20	1.30	1.10	1.20	1.30
ΣTetrahedral cations	4.00	4.00	4.00	4.00	4.00
Al(VI)	1.50	1.50	1.70	1.50	1.50
Ti	—	—	—	—	—
Fe	3.13	3.13	2.93	3.13	3.13
Mg	1.10	1.20	1.10	1.10	1.10
Mn	—	—	—	—	—
Ca	—	—	—	—	—
Na	—	—	—	—	—
K	—	—	—	—	—
ΣOctahedral cations	5.73	5.83	5.73	5.73	5.73
No. of vacancies	0.27	0.17	0.27	0.27	0.27
Fe/(Fe+Mg)	0.74	0.72	0.73	0.74	0.74

Table A-II-1. (Continued)

	Ahn and Peacor (1985)			Ryan and Reynolds (1996)	
	7Å-14Å			7Å-14Å	
Si	2.70	2.70	2.70	2.90	2.88
Al(IV)	1.30	1.30	1.30	1.10	1.12
ΣTetrahedral cations	4.00	4.00	4.00	4.00	4.00
Al(VI)	1.30	1.60	1.40	1.76	1.59
Ti	—	—	—	—	—
Fe	3.74	3.33	3.64	3.18	3.16
Mg	0.80	0.80	0.90	0.72	1.00
Mn	—	—	—	0.01	0.01
Ca	—	—	—	—	—
Na	—	—	—	—	—
K	—	—	—	—	—
ΣOctahedral cations	5.84	5.73	5.94	5.67	5.76
No. of vacancies	0.16	0.27	0.06	0.33	0.24
Fe/(Fe+Mg)	0.82	0.81	0.80	0.82	0.76

Table A-II-1. (Continued)

	Ryan and Reynolds (1996)		Billault (2002), Billault et al. (2003)		
	7Å-14Å		7Å-14Å		
Si	2.80	2.80	2.64	2.82	2.82
Al(IV)	1.20	1.20	1.36	1.18	1.18
ΣTetrahedral cations	4.00	4.00	4.00	4.00	4.00
Al(VI)	1.59	1.70	1.16	1.55	1.55
Ti	—	—	—	—	—
Fe	3.43	2.97	3.87	3.08	3.08
Mg	0.77	1.07	0.76	1.11	1.11
Mn	0.01	0.01	0.00	0.00	0.00
Ca	—	—	—	—	—
Na	—	—	—	—	—
K	—	—	—	—	—
ΣOctahedral cations	5.80	5.75	5.79	5.74	5.74
No. of vacancies	0.20	0.25	0.21	0.26	0.26
Fe/(Fe+Mg)	0.82	0.73	0.84	0.74	0.74

Table A-II-1. (Continued)

	Billault (2002), Billault et al. (2003)		Hornibrook and Longstaffe (1996)		
	7Å-14Å		Berthierine		
Si	2.65	2.65	3.67	3.29	3.55
Al(IV)	1.35	1.35	0.33	0.71	0.45
ΣTetrahedral cations	4.00	4.00	4.00	4.00	4.00
Al(VI)	1.48	1.21	1.75	1.46	1.57
Ti	—	—	0.15	0.02	0.07
Fe	3.53	3.77	2.42	2.96	2.59
Mg	0.75	0.86	0.85	0.90	0.85
Mn	0.00	0.00	0.01	0.01	0.01
Ca	—	—	0.00	0.05	0.09
Na	—	—	0.03	0.03	0.05
K	—	—	0.10	0.05	0.14
ΣOctahedral cations	5.76	5.84	5.30	5.47	5.37
No. of vacancies	0.24	0.16	0.70	0.53	0.63
Fe/(Fe+Mg)	0.82	0.81	0.74	0.77	0.75

Table A-II-1. (Continued)

	Hornibrook and Longstaffe (1996)		Bailey (1988)		
	Berthierine		Odinite		
Si	3.19	3.56	3.66	3.59	3.58
Al(IV)	0.81	0.44	0.34	0.41	0.42
ΣTetrahedral cations	4.00	4.00	4.00	4.00	4.00
Al(VI)	1.46	1.71	0.44	0.30	0.34
Ti	0.07	0.10	0.01	0.01	0.01
Fe	2.87	2.29	0.63	0.90	0.63
Mg	0.91	1.00	2.20	1.85	1.96
Mn	0.01	0.00	0.00	0.00	0.00
Ca	0.09	0.10	0.00	0.00	0.00
Na	0.04	0.10	0.00	0.00	0.00
K	0.10	0.05	0.00	0.00	0.00
ΣOctahedral cations	5.54	5.37	3.28	3.07	2.95
No. of vacancies	0.46	0.63	2.72	2.93	3.05
Fe/(Fe+Mg)	0.76	0.70	0.22	0.33	0.24

Table A-II-1. (Continued)

	Bailey (1988)				
	Odinite				
Si	3.59	3.82	3.90	3.91	3.94
Al(IV)	0.41	0.18	0.10	0.09	0.06
ΣTetrahedral cations	4.00	4.00	4.00	4.00	4.00
Al(VI)	0.72	1.16	1.32	1.35	1.25
Ti	0.00	0.03	0.00	0.04	0.04
Fe	0.57	2.11	1.95	2.13	2.21
Mg	2.03	1.70	1.59	1.29	1.37
Mn	0.00	0.00	0.00	0.00	0.00
Ca	0.00	0.00	0.00	0.00	0.00
Na	0.00	0.00	0.00	0.00	0.00
K	0.00	0.00	0.00	0.00	0.00
ΣOctahedral cations	3.32	5.00	4.86	4.82	4.86
No. of vacancies	2.68	1.00	1.14	1.18	1.14
Fe/(Fe+Mg)	0.22	0.55	0.55	0.62	0.62

Table A-II-1. (Continued)

	Brindely (1982)					
	Berthierine					
Si	2.29	2.19	2.55	2.45	2.55	2.41
Al(IV)	1.71	1.81	1.45	1.55	1.45	1.59
ΣTetrahedral cations	4.00	4.00	4.00	4.00	4.00	4.00
Al(VI)	1.92	1.84	2.05	1.87	1.64	1.57
Ti	0.00	0.00	0.00	0.00	0.00	0.00
Fe	3.46	3.73	3.36	3.60	3.00	3.29
Mg	0.33	0.27	0.16	0.35	1.14	0.49
Mn	0.00	0.00	0.00	0.00	0.00	0.00
Ca	0.00	0.00	0.00	0.00	0.00	0.00
Na	0.00	0.00	0.00	0.00	0.00	0.00
K	0.00	0.00	0.00	0.00	0.00	0.00
ΣOctahedral cations	5.72	5.84	5.57	5.83	5.79	5.36
No. of vacancies	0.28	0.16	0.43	0.17	0.21	0.64
Fe/(Fe+Mg)	0.91	0.93	0.95	0.91	0.72	0.87

Table A-II-1. (Continued)

	Brindely (1982)						
	Berthierine						
Si	2.57	2.85	2.65	2.67	2.71	2.91	3.07
Al(IV)	1.43	1.15	1.35	1.33	1.29	1.09	0.93
ΣTetrahedral cations	4.00	4.00	4.00	4.00	4.00	4.00	4.00
Al(VI)	1.80	1.69	1.68	1.47	1.46	1.26	1.18
Ti	0.00	0.00	0.00	0.00	0.00	0.00	0.00
Fe	3.61	2.96	3.67	3.79	3.84	3.33	3.58
Mg	0.34	0.26	0.45	0.53	0.43	1.32	1.00
Mn	0.00	0.00	0.00	0.00	0.00	0.00	0.10
Ca	0.00	0.00	0.00	0.00	0.00	0.00	0.00
Na	0.00	0.00	0.00	0.00	0.00	0.00	0.00
K	0.00	0.00	0.00	0.00	0.00	0.00	0.00
ΣOctahedral cations	5.75	4.91	5.81	5.79	5.73	5.91	5.87
No. of vacancies	0.25	1.09	0.19	0.21	0.27	0.09	0.13
Fe/(Fe+Mg)	0.91	0.92	0.89	0.88	0.90	0.72	0.78